SYNTHESIS, CHARACTERIZATION, AND TESTING OF COPPER SELENIDE-GRAPHENE NANOCOMPOSITES FOR THERMOELECTRIC APPLICATIONS

A Thesis

by

MUHAMMED ZIAUDDIN AHMAD EBRAHIM

Submitted to the Graduate and Professional School of
Texas A&M University
in partial fulfillment of the requirements for the degree of

MASTER OF SCIENCE

Chair of Committee,	Ahmed Abdala
Committee Members,	Konstantinos Kakosimos
Committee Members,	Mohammed Al-Hashimi
Head of Department,	Arul Jayaraman

December 2021

Major Subject: Chemical Engineering

ABSTRACT

Thermoelectric (TE) materials provide an environment-friendly approach to convert waste heat into electricity. The liquid-like superionic behavior of copper selenides and their ultra-low thermal conductivity have attracted interest as potential thermoelectric material. However, to reach practical applications, the thermoelectric performance of copper selenides requires enhancement. In this thesis, the literature on TE materials is reviewed, the routes for synthesizing different copper selenide materials are discussed, and the strategies for enhancing the thermoelectric performance through alloying, doping, nanostructuring, and nanocomposite formation are discussed. Moreover, the application of graphene as an excellent filler to improve the performance of TE materials is analyzed.

We developed a solution-based method for synthesizing pure copper selenide and its graphene oxide (GO) nanocomposites. Two types of GO prepared following the Tours (GO_T) and the Hummers (GO_H) methods, leading to a different distribution of oxygen functionality, were used. Detailed analysis of the chemical composition, structural morphology, mechanical and thermal properties, and the thermal conductivity of pure and nanocomposite thermoelectric materials was carried out.

The structure of the synthesized materials is characterized using XRD and XPS that confirmed the cubic crystal structure of $Cu_{1.8}Se$ with the absence of impurities. The SEM analysis confirmed the sheet-like morphology with homogenous size distribution synthesized material. The nanocrystal size of $Cu_{1.8}Se$ was ~42 nm based on the *Warren-Averbach* model.

The addition of graphene did not have a significant effect on the grain size of the nanopowders. However, the Hummer's GO composites showed a smaller grain size than Tour's GO composites. The thermal transitions and thermal stability were analyzed using DSC and TGA. The incorporation of graphene increased both the mechanical and thermoelectric properties. The $Cu_{1.8}Se$ and its nanocomposites showed poor thermal stability due to the sublimation of selenium at higher temperatures. This was reflected in poor TE performance and the inability to hot-press the nanocomposites due to melting.

Nonetheless, thermal annealing at 600°C for 10 hours has improved the thermal stability of the pure and nanocomposite samples. The annealed sample also showed enhanced electrical conductivity, Seebeck coefficient, and power factor. The power factor of the pure sample increased from 0.04 mW/mK^2 to 0.56 mW/mK^2 at 300 °C after the thermal treatment.

Our results show that incorporating graphene into copper selenide is an encouraging method to improve the thermoelectric performance of the materials, with the improvement of mechanical properties that may help in device fabrication for commercial applications. Furthermore, the thermal treatment of the nanopowders under inert conditions has drastically enhanced the material's thermal and TE properties.

DEDICATION

I dedicate this work to my family and friends for their constant support, patience, and strength, without which this challenging project would not have been possible.

ACKNOWLEDGEMENTS

I would like to thank and show my gratitude to my supervisor and committee chair, Dr. Ahmed Abdala, for his support and motivation. His continuous guidance helped me through all my research work and brought this research into success. I would also like to thank the committee members, Dr. Konstantinos Kakosimos and Dr. Mohammed Al- Hashimi, for their comments, inspiration, and encouragement.

I am incredibly thankful to Dr. Yiming Wubulikasimu at the Central Materials Facility at TAMUQ to assist me in running multiple characterization tests and extensive training on operating the equipment with in-depth discussions of analyzing the results. I would also like to thank Dr. Khaled Youssef and Ms. Farah ElMakaty at Qatar University for assisting me in various testing throughout my thesis.

Furthermore, I would like to thank my colleague Fizza Usmani for her guidance and support, who helped me tailor my synthesis swiftly with my experimental work.

I am also thankful to the members of the Materials Research Group, especially Omnya Abdalla and Abdulrehman, for their help during my synthesis, organizing the lab, and procurement of required items.

I would also like to thank my fellow students, the department faculty, and staff at Texas A&M University, Qatar, for giving me beautiful memories of this part of my academic life.

Finally, I am most grateful to my family for their unconditional love and patience. They always encouraged me to aspire to the highest and bring out the best in me.

CONTRIBUTORS AND FUNDING SOURCES

Contributors

This work was supervised by the thesis committee consisting of Professors Ahmed Abdala [advisor] and Konstantinos Kakosimos [member] of the Department of Chemical Engineering and Professor Mohammed Al- Hashimi [member] of the Department of Chemistry.

Dr. Yiming Wubulikasimu at the Materials Research Facilities at TAMUQ has carried the XRD, SEM, EDS, and XPS measurements. Dr. Adel Said at the Chemistry Instrumentation Laboratory at TAMUQ has carried the DSC and TGA analysis. Thermoelectric property measurements were performed at the Qatar University in Dr. Khaled Youssef's lab. All other work conducted for the thesis was completed by the student independently.

Funding Sources

Graduate study was supported by a graduate assistantship from Texas A&M University at Qatar and Qatar National Research Fund under NPRP10-0206-170366. Its contents are solely the authors' responsibility and do not necessarily represent the official views of the QNRF.

NOMENCLATURE

Cp	Specific heat capacity
DOS	Density of states
EDS	Energy Dispersive X-ray Spectroscopy
GO	Graphene oxide
PF	Power Factor
k	Thermal Conductivity
k_L	Lattice thermal conductivity
SEM	Scanning Electron Microscopy
σ	Electrical Conductivity
TE	Thermoelectric
TGA	Thermogravimetric Analysis
DSC	Differential Scanning Calorimetry
XPS	X-ray Photoelectron Spectroscopy
XRD	X-ray Diffraction
ZT	Figure-of-merit

TABLE OF CONTENTS

Page

LIST OF FIGURES

LIST OF TABLES

Page

1. INTRODUCTION

The present goal of our society is to look for technologies and innovations that can effectively reduce our dependence on fossil fuels, thereby minimizing greenhouse gas release. With rising population and rapid urbanization, there is an urgent need for environment-friendly techniques and renewable energy sources like solar and wind to replace conventional energy sources [1]. Any energy source usage, be it fossils, solar or electrical energy, generates a lot of waste heat. As much as 60% of the fossil fuel's energy is lost as waste heat and around 70% in automobiles [2]. Thermoelectric (TE) devices can convert thermal energy into electricity from the sun, cars, industrial waste heat, and ubiquitous waste heat. TE devices' advantages are their solid-state nature, ease of scalability, and no having mechanical moving parts, making their maintenance more manageable and cost-effective [3, 4]. Solid-state energy conversion is advantageous due to its simplicity compared to devices run by compression and expansion of a two-phase (liquid/gas) working fluid [5].

Conversely, the reverse phenomenon where electrical energy is converted to thermal energy, i.e., thermoelectric cooling, is used to make refrigerators and other cooling devices [6]. TE device potential can be maximized by working in tandem with other energy conversion technologies. Therefore, TE devices have garnered worldwide attention, and significant research is being carried out to fabricate high-performance TE materials [7].

1.1. History of Thermoelectrics

The thermoelectric effect was first discovered in 1802 by Alessandro Volta, where he observed that the temperature gradient between the junction of two different conducting materials produces an electromotive force[3]. Twenty years later (1821), Thomas Seebeck, a physicist from Berlin, observed the deflection of a compass magnet placed near the circuit of the junction of two dissimilar metals [8]. This effect is now known as the 'Seebeck effect.' Although Seebeck mistakenly refuted the phenomenon's electrical essence and claimed it 'thermomagnetism,' the name 'thermoelectric' was later coined by Orsted [3, 8]. In 1834, a part-time French physicist discovered that an isothermal junction consisting of dissimilar metals is either heated or cooled depending on the direction of current passing through it, which is the opposite to the 'Seebeck effect' and today, this phenomenon is named the 'Peltier effect' [3, 9]. In 1854, a British mathematical physicist, William Thomson, provided a thermodynamic analysis of the Seebeck and Peltier effects. Thomson found a third thermoelectric effect in which heat is either released or absorbed when the current flow in a homogenous material is subjected to a temperature gradient. This effect is now called the 'Thomson effect' [3]. Based on the Seebeck, Peltier, and Thomson effects, thermoelectrics found various applications in the 20^{th} century where energy availability was more important than efficiency. In 1885, the British physicist John William Strutt Rayleigh was the first to use the Seebeck effect for power generation [3, 10]. Various devices were fabricated to

generate electric current later in the 19th century, and these devices were named thermoelectric generators [3].

In 1909, a German physicist, Edmund Altenkirch, proposed a formula to calculate the maximum efficiency for thermoelectric generators. In 1922, Edmund also obtained the coefficient of performance of a Peltier cooler [3]. The dimensionless figure-of-merit *zT*, which analyzes and compares the thermoelectric efficiency for thermocouples, was first established in 1949 by a Russian physicist named Abram Fëdorovič Ioffe [3, 11].

The efficiency of thermoelectric devices was not up to the mark, and research around the 1960s started to focus more on conventional devices. However, the solid-state and immovable mechanical parts kept the research programs on TE devices alive. The first Radioisotope Thermoelectric Generators (RTGs) were first developed in the late 1950s. In 1961, the United States launched SNAP 3, the first spacecraft equipped with Radioactive Thermoelectric Generator (RTG).

The advent of nanotechnology paved way for the advancement of thermoelectrics. In 1993, L. D. Hicks and Mildred Dresselhaus of the Massachusetts Institute of Technology (MIT) published a theory paper titled “Effect of Quantum Well Structures on the Thermoelectric Figure of Merit’’ outlining the importance of nanotechnology to improve the performance of thermoelectric devices [3, 12, 13]. This novel approach to increase the zT began to garner more interest, and significant research was carried to develop high-performance thermoelectric devices. Conventional petrol/diesel engines could be soon replaced in the

upcoming years as the current attention is focused on renewable and sustainable technology for the forthcoming generations. Hence, investment in thermoelectric technology will be a strategic target for many companies across the world.

1.2. Fundamentals of Thermoelectrics

Thermoelectric conversion is defined as the conversion of thermal energy to electrical energy [4]. TE devices work on the principle of the thermoelectric effect. The effect is a combination of three effects: Seebeck, Peltier, and Thomson effects, all of which have been briefly explained in *Section 1.2 History of Thermoelectrics* [14]. This effect is applicable for both power generation and active refrigeration.

In thermoelectric power generation, the charge carriers will move from the hot junction to the cold junction due to high thermal energy at the hot junction when a thermoelectric couple consisting of n-type and p-type elements is subjected to a temperature gradient (ΔT) [4]. This induces an electric potential (ΔV) across the junction leading to the production of electric current in the circuit [4, 15]. This effect is defined as the Seebeck effect, discovered by Thomas Johann Seebeck in the year 1821 [3, 15, 16]. The Seebeck coefficient, S, is given by [4]:

$$S = \Delta V/\Delta T \qquad (1.1)$$

The sign of S changes accordingly with the current direction and is usually measured in V/K or μV/K [17]. Seebeck coefficient is the basis of thermoelectric power generation.

Conversely, suppose an external electromotive force is applied across the junction of two dissimilar metals, the reverse phenomenon of the Seebeck effect takes place, which is known as the 'Peltier effect', named after the French physicist Jean Charles Peltier who discovered this phenomenon in 1834 [3, 4, 16, 17]. The flow of current either produces a heating or cooling effect at the junction [15]. The Peltier coefficient π is the ratio between the heat q removed from the system and the current I passing through the system [14, 17]. The Peltier coefficient (π) has units of V and is given by:

$$\pi = \frac{q}{I} \tag{1.2}$$

The principles of the Seebeck and Peltier effects are illustrated in Figure 1.

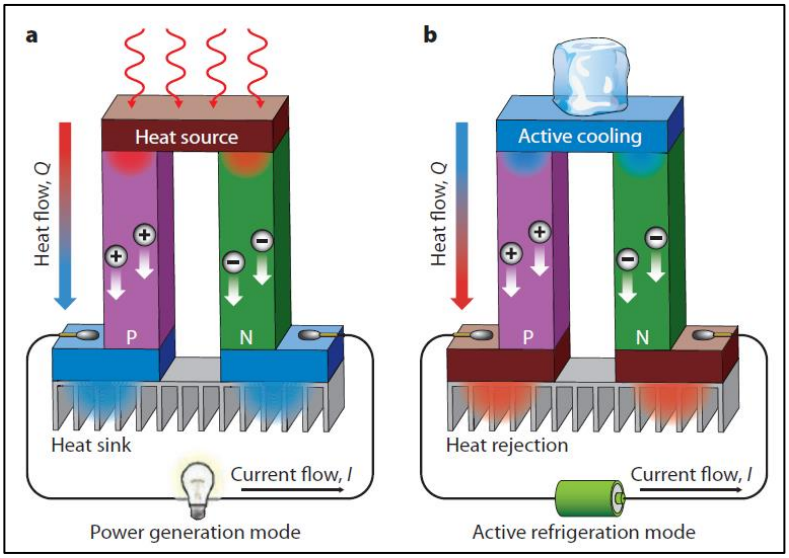

Figure 1: (a) TE generator and (b) TE refrigeration. (a) A temperature gradient provokes the charge carriers to diffuse from the hot end to the cold end, thereby generating current in the circuit.

(b) Electric current passes through the active refrigerator inducing a temperature difference across the junction, and the cold end absorbs heat Adapted from Li et al. Li, et al. [4].

The third thermoelectric effect, the Thomson effect, occurs when heat is either absorbed or released by the charge carriers along a single homogenous conductor with a temperature difference of ΔT [18]. The Thomson coefficient (β) is defined as [17]:

$$\beta = q\, I \Delta T \tag{1.3}$$

The units for the Thomson coefficient are also V/K [17].

1.3. Figure of merit

A thermoelectric devices' performance is represented by a dimensionless figure-of-merit (*zT*) introduced by Abram Fëdorovič Ioffe in 1949 [3, 4, 11, 15-17]. *zT* is defined as [3, 4, 17] :

$$zT = \frac{S^2 \sigma}{k}\, T \tag{1.4}$$

S, σ, κ, and *T* is the Seebeck coefficient, the electrical conductivity, the thermal conductivity, and the absolute temperature at which the properties are measured. A material with higher zT corresponds to better thermoelectric performance. To maximize zT, both the Seebeck coefficient (S) and electrical conductivity (σ) must be high, while the thermal conductivity (*k*) must be low [4]. A material with zT of one is considered a good TE material. However, a zT of ~ 3 is essential for TE energy converters to reach any efficiency comparable to mechanical power generators [4, 19]. As shown in Figure 2, a higher temperature gradient

would lead to increased efficiency. Hence, TE materials that maintain a large temperature gradient across its ends is preferred.

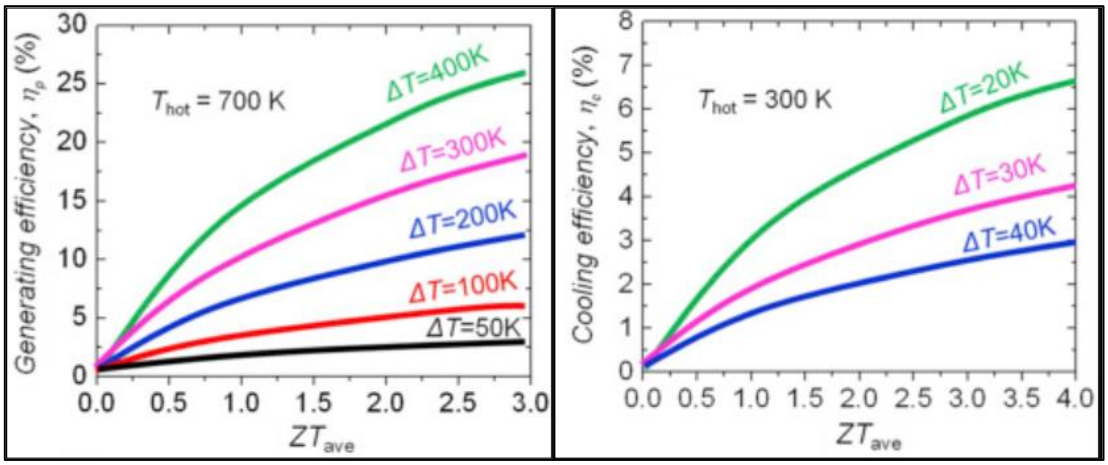

Figure 2: Power generation efficiency based on the Seebeck effect and cooling efficiency based on the Peltier effect as a function of average ZTave. The figure shows that a larger temperature difference and higher zT will have better efficiency. Adapted from Zhang and Zhao [16].

The maximum efficiency of a TE generator as a function of Carnot efficiency is given by [15, 20, 21]:

$$\eta_p = \frac{T_{hot}-T_{cold}}{T_{hot}} \frac{\sqrt{1+ZT_m}-1}{\sqrt{1+ZT_m}+\frac{T_{cold}}{T_{hot}}} \tag{1.5}$$

zT_m is the figure of merit averaged over the hot and cold junction temperature, i.e., the *n*-type and *p*-type legs [15]. Moreover, the thermoelectric cooling efficiency at the electrified junction is given by[16]:

$$\eta_c = \frac{T_{hot}}{T_{hot}-T_{cold}} \left[\frac{\sqrt{1+ZT_{avg}}-\frac{T_{hot}}{T_{cold}}}{\sqrt{1+ZT_{avg}}+1} \right] \tag{1.6}$$

A higher zT_{ave} and a larger temperature gradient will provide a higher thermoelectric efficiency required to match the conventional mechanical engines.

1.4. Thermoelectric Materials

The advent of semiconductors paved the way again for more research to be focused on TE materials. Maria Telkes, in the year 1947, developed a Thermoelectric Generator (TEG) based on PbS and ZnSb that achieved a conversion efficiency higher than 5% for a temperature difference of 400 K [22]. The Soviet Union in the 1950s produced ring-shaped TEGs that is made up of ZnSb that ran on heat from kerosene lamps [23]. Various materials have been used in the fabrication of TE devices, but due to their low efficiency, TE devices were not successful compared to other techniques like mechanical power generators. However, TE devices were used for spacecraft as they required less maintenance and no mechanical moving parts. The most commonly studied TE materials are lead, tellurium, and germanium but because these metals are either uncommon or hazardous, other groups of materials are being studied.

Due to their high Seebeck coefficient, semiconductors are undoubtedly the most studied material for TE devices. Inorganic compounds like Bi_2Te_3 and its alloys have high zT due to their low thermal conductivity [24]. The advantages of inorganic over organic materials are their superior thermoelectric properties. Materials with a small bandgap are desirable for use in TE devices [25]. Semiconductor TE materials can also be classified into three types, according to their use-temperature ranges. Bi_2Te_3- based low-temperature materials that are

used below 400 K, PbTe based middle-temperature materials that operate between 600 and 900 K, and SiGe-based high-temperature materials that are used above 900 K [26].

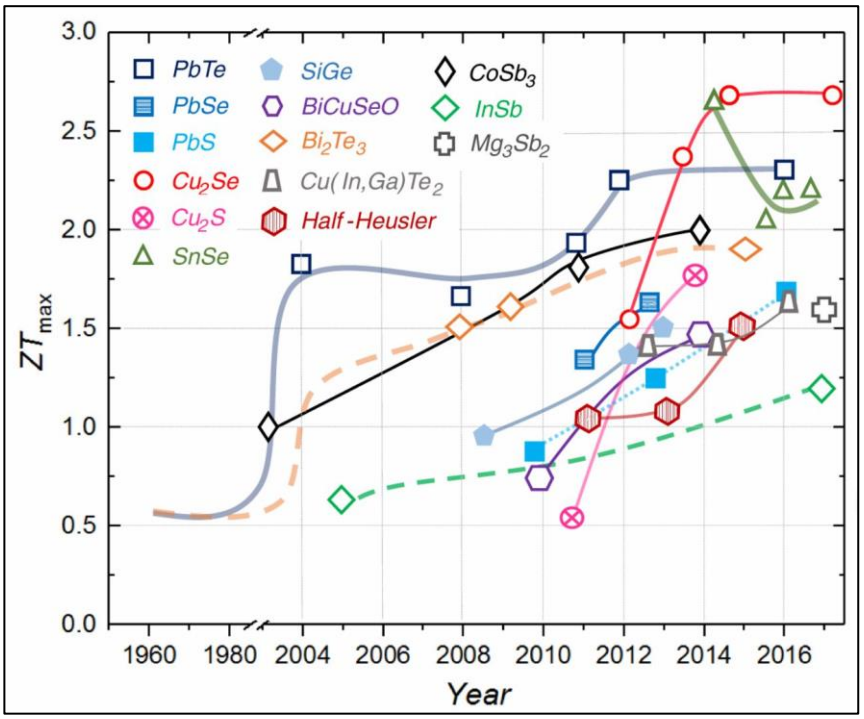

Figure 3: Evolution of ZT of various thermoelectric materials. Adapted from He &Tritt (2017) [27]

Figure 3 depicts the advancement of zT over the past decades with low toxic materials. The recent attention of the research community has been directed to chalcogenides. Chalcogenides are a group of inorganic thermoelectric materials made of tellurides (Te), selenides (Se) and sulfides (S). Chalcogenides are the best thermoelectric contender among all inorganic materials and have been widely employed due to their consistent and superior thermoelectric performance over other materials [28]. Because of the low ZT of ceramic and polymer-based

TE devices, semiconductors are still the most promising candidates for TE devices [16]. Therefore, this research focuses on copper selenide, a p-type semiconductor.

1.5. Enhancement of the performance of thermoelectric materials

1.5.1. Challenges

Enhancing the performance of thermometric materials, i.e., increasing zT, is the focus of the thermoelectric research community. As discussed in the previous section, zT of ~ 3 is necessary to commercialize thermoelectric devices [4, 19]. A good TE material is expected to have the properties of 'phonon-glass/electron crystal' (PGEC) material [17, 29]. This material should have low glass-like thermal conductivity and excellent crystal-like electrical properties [17, 29]. The main challenge in achieving high zT is the interdependent thermoelectric properties, namely electrical conductivity, Seebeck coefficient, and thermal conductivity. TE materials should have low thermal conductivity (k) for a large temperature gradient, high electrical conductivity to reduce the Joule heat loss and a high Seebeck coefficient for better voltage output [30].

The typical approach of improving TE materials' performance is to increase the power factor ($S\sigma^2$) by changing the carrier concentration 'n' or reducing lattice thermal conductivity [24, 30]. The thermal conductivity, k, is the sum of the electronic (k_e), the lattice (k_l), and the bipolar (k_b) thermal conductivity elements [24, 30].

The electrons and holes contribute to the electrical conductivity and electronic thermal conductivity, while the phonons contribute to the lattice thermal conductivity [24]. Generally, good thermoelectric materials are heavily doped semiconductors with a carrier concentration of 10^{19}-10^{21} cm^{-3} [31]. On the other hand, the lattice thermal conductivity can be reduced by incorporating scatter centers [24, 30].

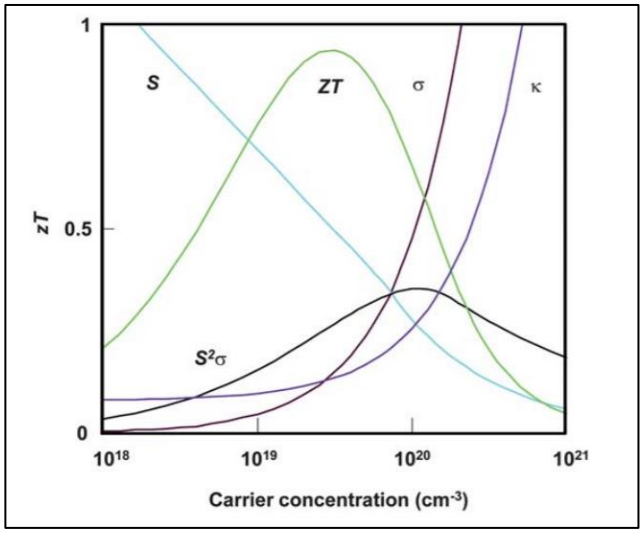

*Figure 4: a) The dependence of the Seebeck coefficient (S), electrical conductivity (**σ**), and thermal conductivity (k) with carrier concentration. Semiconductors have the perfect carrier concentration for the maximum power factor (PF). Adapted from Snyder and Toberer [32]*

The Seebeck coefficient (S) accounts for the energy difference between the average energy of the mobile carrier and the Fermi energy [24, 30, 33]. If the carrier's concentration is high, both the average energy and the Fermi energy increase, but the Fermi energy increases more swiftly than the average energy, which reduces the Seebeck coefficient and thereby the power factor ($S\sigma^2$). Thus, due to the interconnection of TE properties, an increase in the carrier concentration increases the electrical conductivity but reduces the Seebeck coefficient.

Charge carriers conduct electricity as well as heat. The Wiedemann-Franz law gives the relationship between the electronic thermal conductivity (K_e)and the electrical conductivity (σ), as shown in Equation (1.7) [4, 24, 30].

$$K_e = L\,\sigma\,T \tag{1.7}$$

Where k_e is the electronic thermal conductivity, T is the temperature, σ is the electronic, electrical conductivity, and L is the Lorenz number that varies based on carrier concentration $\left(L = 1.6x10^{-8}\frac{V^2}{K^2} - 2.2x10^{-8}\frac{V^2}{K^2}\right)$ [30].

The relationship between electrical conductivity and carrier concentration is given by:

$$\sigma = \mu ne \tag{1.8}$$

μ is the carrier mobility, n is the carrier concentration, and e is the charge of an electron.

From equation 1.7, it is clear that the electrical conductivity (σ) is proportional to the electronic contribution to the thermal conductivity (k_e). Any method employed to increase electrical conductivity will increase k_e, thereby increasing thermal conductivity. Therefore, other techniques must be employed for increasing zT. Also, an attempt to decrease the lattice thermal conductivity by increasing phonon scattering will decrease the carrier mobility as most defects tend to scatter both phonons and electrons [30]. The thermoelectric parameters are intertwined where one affects the other, and a proper decoupling of these parameters is

needed to enhance the *zT*. It is also important to note that there is no limitation on increasing the value of zT by the second law of thermodynamics [24].

1.6. Enhancing the Performance of Thermoelectric Materials

1.6.1. Enhancement by nanostructuring

The main motive when developing high-performance TE material is to unwind the interconnection of thermoelectric physical properties. The formation of nanostructures is a sound way to improve TE performance. Nanostructuring plays a pivotal role in enhancing the figure-of-merit by reducing the lattice thermal conductivity. By nanostructuring, the dimensions of the material are reduced. This approach has been considered to improve the zT for low-cost thermoelectric bulk materials like semi-metallic bismuth, metallic zinc, and semiconducting silicon [7]. The density of states (DOS) near the Fermi level is significantly enhanced due to quantum confinement when the particle size is reduced, and the particles' interatomic distance equals the phonon mean free path [4, 12]. The DOS increases with a decrease in the dimensionality [7], which in turn improves the Seebeck coefficient by increasing the effective carrier mass and paves the way to improve the earlier challenge faced to enhance zT by decoupling power factor ($S\sigma^2$) and electrical conductivity (σ) [4, 34]. This approach has its constraints as small confinement length requirements are difficult to fabricate in many materials [7]. In 1993, Hicks and Dresselhaus [12] reported that the zT value of two-dimensional (2D) Bi_2Te_3 could be increased via quantum confinement over three-dimensional (3D) structures [12]. The bulk 3D material's chemical potential could be influenced only by

chemical doping compared to their 2D counterpart, wherein their chemical potential could be optimized by varying the thickness of each Bi_2Te_3 layer [12]. A study conducted by Hicks et al. [35] on PbTe/$Pb_{1-x}Eu_xTe$ system showed that decreasing the well-width increases the power factor several times over the bulk material [35]. It was recently demonstrated that the electric field effect (EFE) could manipulate DOS at the Fermi level by incorporating carrier quantum confinement [36]. Theoretical calculations predict that Bi_2Te_3 nanowires could achieve a zT = 3.4 at room temperature when the carrier concentration is modified using this EFE method [7].

The relation between phonon mean free path (l) and lattice thermal conductivity (K_l) is given by [12, 30, 34, 37, 38]:

$$K_l = \frac{1}{3} C_v v l \tag{1.8}$$

C_v is the heat capacity at constant volume, v is the velocity of sound, and l is the phonon mean free path.

The second approach to reducing the lattice thermal conductivity is by incorporating nanostructures to scatter phonons' transport due to nanostructures' interfaces, reducing thermal conductivity [7, 24]. Any dimension less than phonons' average mean free path will decrease the thermal conductivity [4, 7]. The mean free path of electrons is shorter than those of phonons in heavily doped semiconductors, as illustrated in Figure 5.

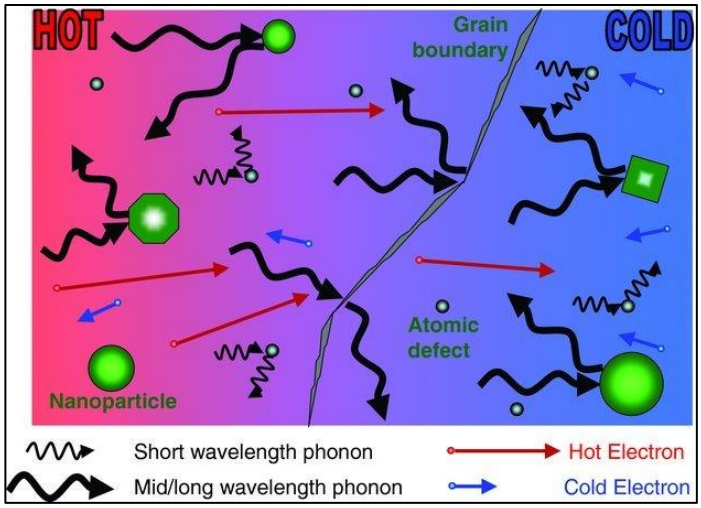

Figure 5: Schematic illustration of different mechanisms of scattering of phonons within a thermoelectric material. Nanoparticles scatter the longer wavelength phonons, while the atomic defects scatter the short-wavelength phonons. The figure also depicts the electronic transport of hot and cold electrons in the material. Adapted from Vineis et al. [38].

Hence, introducing a large density of interfaces by nanostructuring will predominantly scatter the phonons with a large mean free path over electrons [34, 38]. This method does not hinder the electrical conduction within the material. For example, the thermal conductivity of Bi_2Te_3 films fabricated by pulsed laser deposition shows a significant 25% reduction in thermal conductivity (0.3–0.4 W m^{-1} K^{-1}) compared to the bulk Bi_2Te_3 [4]. The introduction of grain boundaries also aids in the reduction in thermal conductivity [4]. Seebeck coefficient of $Bi_{0.46}Te_{0.54}$ nanowires deposited in the nanopores of anodized alumina membranes increased by 15-60% compared to their bulk at 300 K [24]. Kesker *et al.* [24] reported a decrease in Bismuth nanotubes' thermal conductivity five times over Bismuth powder due to the decrease in lattice thermal conductivity through interface scattering, as shown in Figure 6.

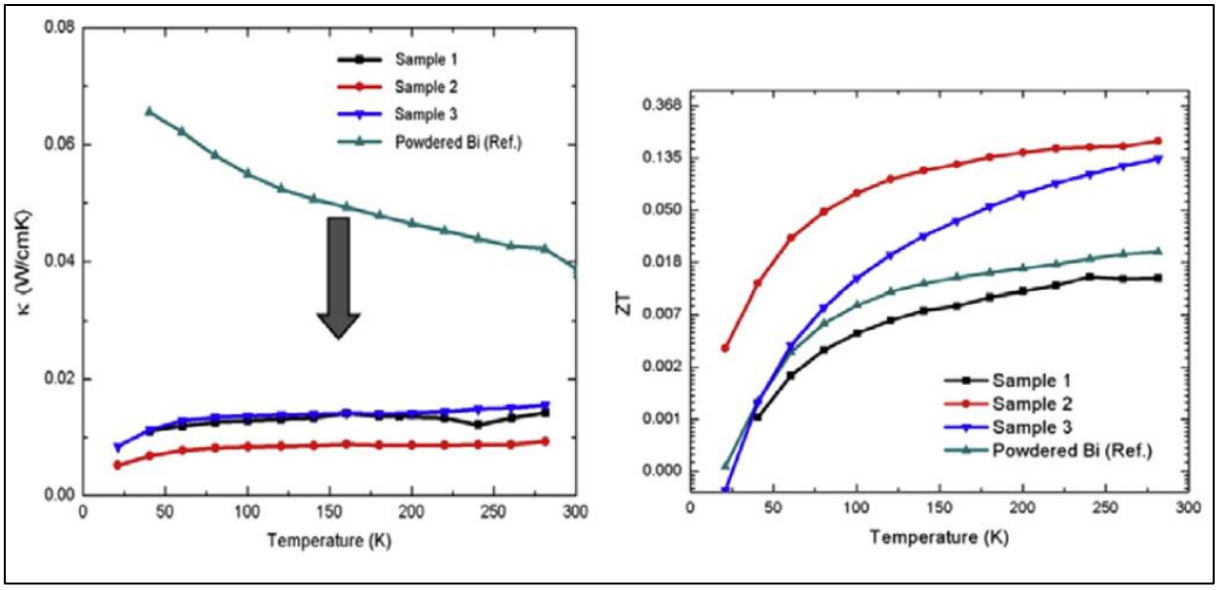

Figure 6: Thermal conductivity and zT as a function of temperature for the nanostructured samples. As seen in the figure, the thermal conductivity is significantly reduced after nanostructuring than the powder form. The zT is also enhanced and reached 0.2 at 280 K due to the reduction in thermal conductivity. Adapted from Alam and Ramakrishna [24]

1.6.2. Enhancement by Doping/Alloying

Doping and alloying are typical approaches to improving the efficiency of thermoelectric materials by either increasing the power factor or decreasing the material's thermal conductivity.

1.6.2.1. Alloying

Alloys of bismuth telluride reached a zT of 1 at room temperature in the 1950s [38]. The main motive of alloys is to generate point defects that scatter phonons. The host and guest should be of the same group in the periodic table to minimize the scattering of carriers [7].

$Si_{1-x}Ge_x$ is a commonly used alloy-based thermoelectric material where the undoped alloy's thermal conductivity is lower than undoped Si [7]. The alloying process allows the calibration of the carrier concentration of the lattice thermal conduction without decreasing the electrical conductivity. The lattice thermal conductivity of Bi_2Te_3 is reduced with Sb_2Te_3 and Bi_2Se_3 hence increasing the zT [24]. Similarly, binary tellurides (Bi_2Te_3, Sb_2Te_3, PbTe, and GeTe) are alloyed and studied extensively for their thermoelectric properties [39]. The same has been considered for $AgSbTe_2$ to increase the zT value above 1. The p-type alloy $(GeTe)_{0.85}(AgSbTe_2)_{0.15}$ was found to have a zT value of 1.2 at 400 K [40]. Tang et al.[41] reported a significant increase in zT when SnTe was alloyed with MgTe. The solubility of MgTe was increased to 20% in this approach, which facilitated valence band convergence [41].

1.6.2.2. Doping

One of the template methods to maximize the figure of merit value is by modifying carrier concentration to the optimized value. The zT of a material can be further optimized by increasing the DOS if the dopant has energy levels near the Fermi level and increasing thermopower [7]. Doping improves the Seebeck coefficient of the material, thereby enhancing the thermoelectric performance. Zhao *et al.* [42] reported an increase in the thermoelectric figure of merit at 300 K for SnSe from 0.1 for the undoped sample to 0.7 for the sample hole-doped with sodium (Na) at 300 K, reaching a maximum zT of 2.0 at 773 K. This high performance is attributed to the increase in the electrical conductivity of SnSe from ~12 S cm^{-1} to 1500 S cm^{-1} by hole doping [42]. The increased electrical conductivity and

enhanced Seebeck coefficient are essential in increasing the PF [42]. Heremans et al. [43] reported a zT value of 1.5 at 773 K for Thallium doped PbTe, which is more than twice the zT of conventional bulk PbTe (0.7). The local DOS increases, increasing the effective carrier mass without any change in the carrier concentration when a donor or acceptor level lies near the Fermi level. The Seebeck coefficient was enhanced by the distortion of the electronic density of states near the Fermi level. The effective mass increased by three while the mobility decreased by a factor of 3-5. Such band engineering techniques, along with nanostructuring, reduce the sample's thermal conductivity [43].

1.6.3. Enhancement by Nanocompositing

Most of the current research on low-dimensional thermoelectrics has been investigated at the nanoscale level by understanding the TE phenomena without applying them for energy conversion at a macroscopic level. To overcome this limitation, Nanocompositing has become an encouraging method to increase the dimensionless figure of merit. Nanocomposites are used to scale up and produce large quantities for commercial use. Nanocomposites are bulk materials made up of nanostructured constituents. Nanocomposites of thermoelectric materials have different nanostructures, including refined grains, dispersed particles, and atomic defects. The main objective of nanocomposite fabrication is to introduce as many interfaces as possible to reduce the thermal conductivity, increase the Seebeck coefficient, and maintain or improve the electrical conductivity. Both these factors contribute to the increase in zT [44]. The most successful approach for enhancing the zT of

nanocomposites is reducing the thermal conductivity [45]. Jeng et al. [46] carried a Monte-Carlo simulation of nanocomposite thermoelectric materials to study their thermal transport. Their results indicated a decrease in thermal conductivity compared to that of the minimum alloy [46].

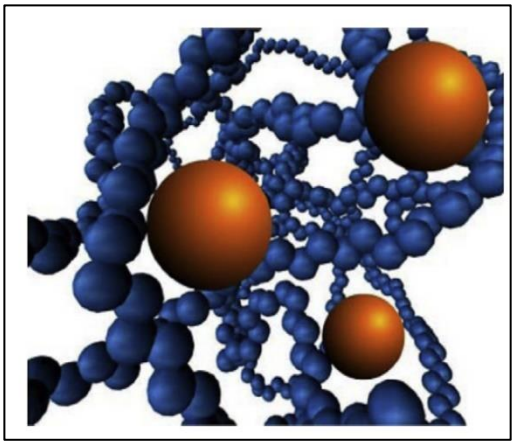

Figure 7: Nanocomposite thermoelectric material, assembly of nano-inclusions materials embedded in a host material or matrix. Adapted from Alam and Ramakrishna [24]

Dresselhaus et al. [44] reported a decrease in the thermal conductivity below an alloy with the exact overall stoichiometry by the random distribution of nanostructures in SiGe nanocomposites, as shown in Figure 7 Figure 7: Nanocomposite thermoelectric material, assembly of nano-inclusions materials embedded in a host material or matrix. Adapted from Alam and Ramakrishna [24]. The thermal conductivity of 10 nm and 50 nm Si-Ge nanocomposites wires was numerically predicted and experimentally confirmed lower than the Si-Ge superlattices [44].

Poudel et al. [47] reported increasing zT for bulk p-type $Bi_xSb_{2-x}Te_3$ alloys by incorporating nanostructured morphologies [47]. Nanopowders of p-type BiSbTe were prepared by ball milling of bulk p-type BiSbTe ingots followed by hot pressing to produce the nanocomposites [47]. The phonon scattering by grain boundaries and defects decreased the thermal conductivity from 1.4 W/mK for the bulk ingot to 1.1 W/mK for the nanocomposite associated with an increased electrical conductivity [47]. The grain boundaries are depleted of charge carriers. These grain boundaries serve as Schottky barriers, wherein the grain boundary is a source of holes introduced into the grains, thereby increasing the material's electrical conductivity [33]. Therefore, these grain boundaries, in addition to phonon scattering, could also impact electrical conductivity based on this hypothesis.

Ni *et al.* [48] prepared Bi_2Te_3 based nanocomposites by hot pressing metal alloys and powders synthesized by the hydrothermal method. P-type $Bi_{0.5}Sb_{1.5}Te_3$ and N-type $Bi_2Te_{2.85}Se_{0.15}$ were balled milled to powders and mixed with 10 wt.% hydrothermally synthesized Bi_2Te_3 powders. The mixture was then hot pressed to produce 1-mm thick nanocomposite discs. A more substantial decrease in thermal conductivity over electrical conductivity was observed due to nanopowders' addition that lead to an increase in zT [48].

Figure 8 shows the Transmission Electron Microscopy (TEM) image of $Si_{80}Ge_{20}$ nanocomposite prepared by mechanical alloying of the pure elements with P micro powders. The grain size is small (10-20 nm) than a typical $Si_{80}Ge_{20}$ grain, around one micron or larger. These structures are smaller than the phonon's mean free path but larger than that of electrons.

Hence, phonons are scattered by these interfaces over the charge carriers, thereby reducing the material's thermal conductivity. The peak zT of the SiGe bulk alloy was 1.3 at 900 °C [49].

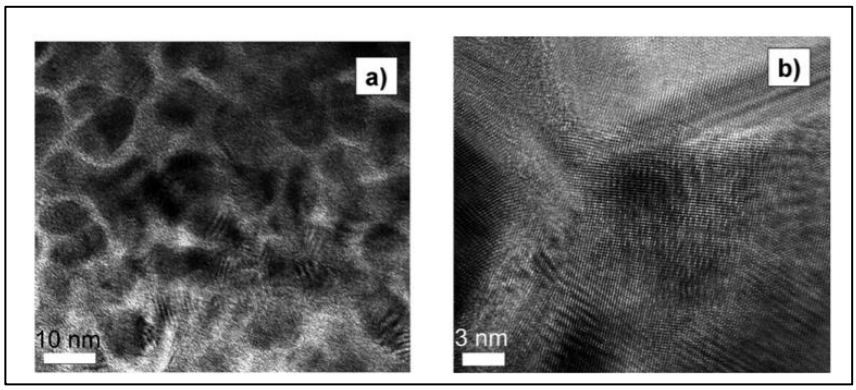

Figure 8: (a) TEM and (b) HRTEM images of $Si_{80}Ge_{20}$ nanocomposite. Adapted from Minnich et al. [50]

There are several challenges associated with the fabrication of nanocomposites. Previously, atomic layer deposition techniques were the only viable techniques to fabricate nanostructured materials. Recently, bulk processes were conducted to create a thermodynamically stable nanostructured material. One of the critical challenges is to sustain the thermoelectric performance of the devices based on nanocomposites during practical applications without disintegration over repeated use [50].

Thermal stability is also an important characteristic that must be addressed when developing nanocomposites, as these devices usually operate at high temperatures. Despite all these challenges, various methods have been developed to fabricate nanocomposites. Ball milling, followed by hot pressing, is used to make nano-grained materials [50]. Other techniques

include thermal processing to produce nanoscale precipitates [50], hydrothermal and solvothermal synthesis, and wet-chemical synthesis [51].

2. LITERATURE REVIEW

2.1. History of Cu- based Thermoelectric

The first use of copper-based material as a TE material was documented in 1827 by the French scientist Antoine César Becquerel when he studied the electricity produced in circuits made of ring-shaped platinum and copper heated by candles [52, 53]. Burning sulfur powders over the Cu wire improves electricity generation. Over thirty years later, Monsanto Company applied for a patent for Ag-doped Cu_2Se TE material in 1959.

The interest in copper-based thermoelectric materials has increased drastically. The number of annual articles published on Cu-based TE materials, obtained from the 'Web of Science' and 'Scifinder' database using the keywords "copper" and "thermoelectric" is provided in Figure 9 [1]. Conventional TE materials like Bi_2Te_3 and PbTe are comprised of rare elements and are toxic to the environment.

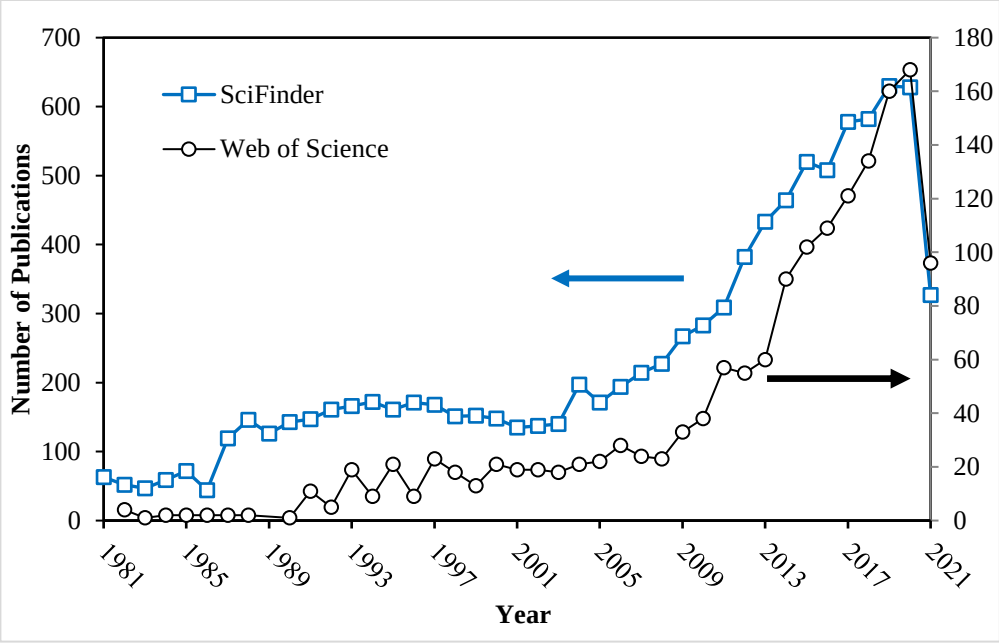

Figure 9: Annual publications on Cu-based TE materials returned using "copper" and "thermoelectric" as keywords. Source: Web of Science and SciFinder Date of Search: 12th July 2021.

Copper chalcogenides have garnered immense interest in the field of TE due to their "phonon-liquid electron-crystal'' (PLEC) property and the low raw materials cost. A zT of 0.95 at 850 K was reported by Shi et al. [54] in quaternary chalcogenide $Cu_3ZnSnSe_4$. Many Cu- based compounds like Cu_2SnSe_3 and $CuInTe_2$ have been found to have zT > 1 [55, 56]. PLEC led to the fabrication of more copper-based TEs, resulting in very low thermal conductivity as observed in the Cu_2Se synthesized by Liu et al. [57] that had a max zT of 1.5 at 1000 K. The figure of merit of the current Cu- based TEs have exceeded 2.0 with ultrahigh TE performance of 2.3 at 400 K in iodine doped Cu_2Se [58].

2.2. Copper Selenide Thermoelectric Materials

Copper selenides have been a promising TE material for more than 200 years. The lack of cutting-edge research and acceptable documentation practices hindered the growth of applications of copper chalcogenides. Figure 10 depicts the number of scientific literature published per year, primarily dealing with copper selenide. The graph indicates that the starting point for the onset of copper selenides happened around the year 1980, and the involvement of research is growing in the thermoelectric field.

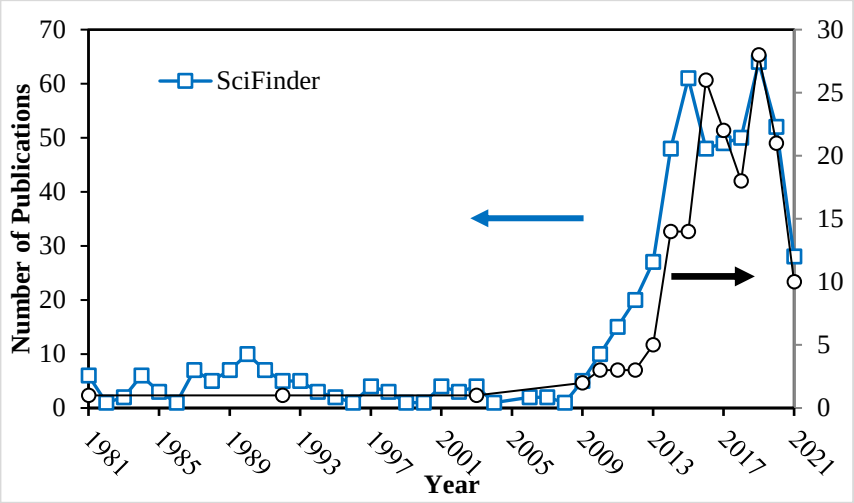

Figure 10: Number of annual publications (1981–2020) using "copper selenide" and "thermoelectric" as the keywords. Source: Web of Science and Scifinder (Date of Search: July 12th, 2021)

2.2.1. Structure and Properties of Copper Selenide

Nanostructure materials are those materials that have at least one dimension between 1 and 100 nm. Nanomaterials are defined to have strong chemical bonds and delocalization of

valence electrons [59]. Cu-based TE materials have recently gained much interest due to the abundance of copper [60]. Due to their characteristic electrical and optical properties, metal chalcogenides have been extensively studied with potential applications in various fields like batteries, gas sensors, and photovoltaic cells [61]. Metal chalcogenides are also used in superionic conductors, photodetectors, photothermal conversion, electro-conductive electrodes, and microwave shielding [62-65].

Cu-based chalcogenides have high efficiency, adjustable transport properties, and low toxicity [66]. Copper Selenide is a p-type semiconductor (conduction is due to the movement of positive holes) that exists in many phases and crystal structures in both stoichiometric (CuSe, Cu_2Se, and Cu_3Se_2) and non-stoichiometric ($Cu_{2-x}Se$) structures [61]. CuSe crystal structure is a hexagonal closed packed (HCP) at room temperature that undergoes a transition to the orthorhombic phase at 48° C and goes back to HCP at 120°C [67].

Table 1: Crystal Structure of CuSe and Cu_2Se

System	**Phase**	**Crystal Structure**	**Space group**	**Lattice parameter (nm)**			**T (K)**	**Ref.**
				a	*b*	*c*		
CuSe	α	Hexagonal	$P6_3/mmc$	1.42		1.73	298	[68]
	β	Orthorhombic	Cmcm	0.395	0.686	1.724	353	
	γ	Hexagonal	$P6_3/mmc$	0.398		1.726	485	
Cu_2Se	α	Monoclinic, β = 94.31°	C2/c	0.714	0.124		<400	[69]
	β	Cubic	Fm3m	0.569	0.569	0.569	>400	

The $Cu_{2-x}Se$ phase is similar to the B4 (ZnO) and Cl (CaF_2) structures with a *fcc* lattice with six to eight copper atoms occupying the octahedral, tetrahedral, and trigonal sites randomly and four selenium atoms at the face center [70]. As shown in Figure 11, the Cu deficient region ($Cu_{2-x}Se$) shows two phases, a low- temperature α-phase and a high-temperature β-phase [71].

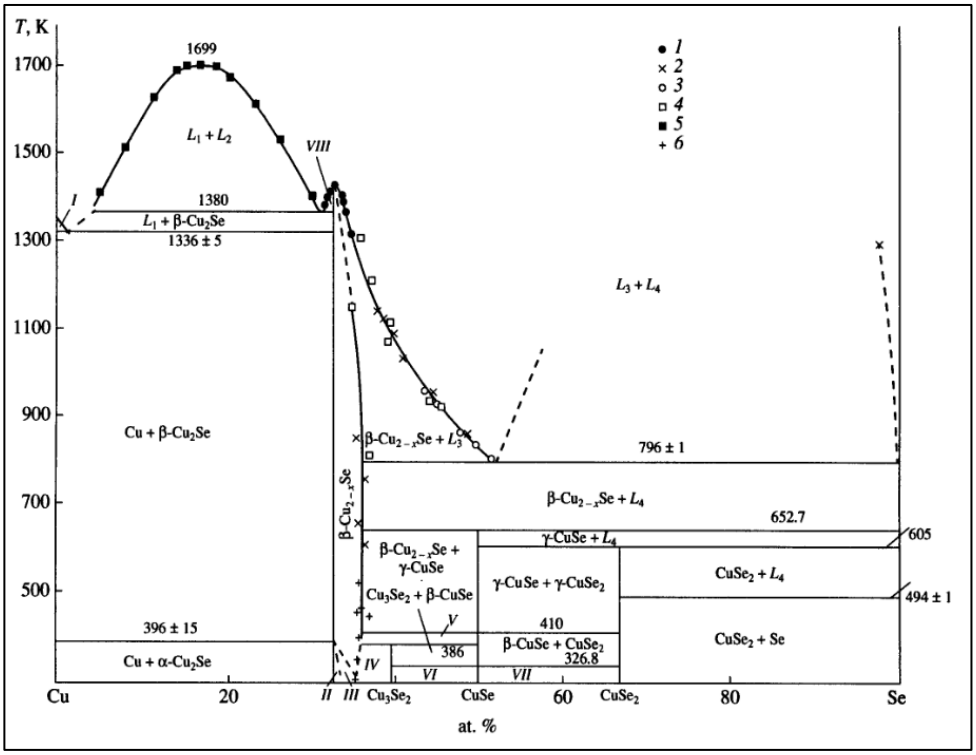

Figure 11: Binary phase diagram of Cu-Se. Adapted from Glazov, et al. [71]

Se atoms are present in an uncomplicated *fcc* structure at high-temperature β-phase with the space group $Fm\bar{3}m$ (Figure 12), but the superionic copper ions spanning the structure are

kinetically disordered. The α -phase is stable up to ~400 K and has a lower symmetry crystal structure [57].

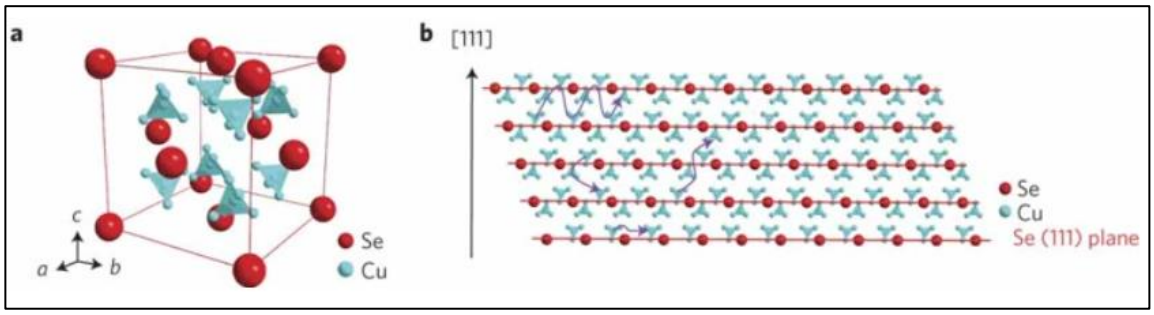

Figure 12: a) Unit cell is shown with Cu atoms occupying the 8 (c) and 32 (f) sites and b) the crystal structure along [110] direction. The arrows represent the movement of Cu ions between the interstitial sites. Adapted from Liu, et al. [57].

Based on the electron counting rules, the stoichiometric Cu_2Se is assumed to be an intrinsic semiconductor with optical studies indicating a bandgap of 1.23 eV [72]. $Cu_{2-x}Se$ is detailed to have a direct bandgap of 2.2 eV and an indirect bandgap of 1.4 eV for x=0.2 [73]. In contrast, Tadashi et al. and Vohl et al. reported a direct bandgap of 2 eV. The sharp cut causes the band gap's variation of the wavelength with spectral transmittance instead of the slow increase [74]. The variation is also caused by the deviation from stoichiometry, dislocations, the variation in grain size, and the quantum effect [75].

The non-stoichiometric phase is an excellent p-type electrical conductor with a high Seebeck coefficient [76]. The conductivity of the material increases with increasing Cu- deficiency. The transport properties of polycrystalline $Cu_{2-x}Se$ are excellent both in the low and high-temperature phases. The material has low electrical resistivity and a high Seebeck coefficient, Figure 12-b. The Seebeck coefficient, S, is 60 -100 μVK^{-1} in the α-phase (300-350 K), and

80 - 300 μVK^{-1} in the β-phase (420- 1,000 K) [57]. These values are comparable to the best TE materials available.

The carrier density of $Cu_{2-x}Se$ is in the order of 10^{20} cm^{-3}, as reported by Liu et al. [57]. At room temperature, the measured power factor ($PF = S^2/\rho$) is ~ 6-8 μW cm^{-1}K^{-1} for the α-phase and 7-12 μW cm^{-1}K^{-1} for the β-phase. $Cu_{2-x}Se$ has low thermal conductivity, as shown in Figure 13**.** *Liu et al*. reported a zT of ~ 1.5 at 1,000 K for Cu_2Se, which is very on par with the best TE materials available [57]. The material developed by Liu et al. was prepared using spark plasma sintering and was un-doped, which suggests that refining the TE properties by doping or any other means would increase zT further.

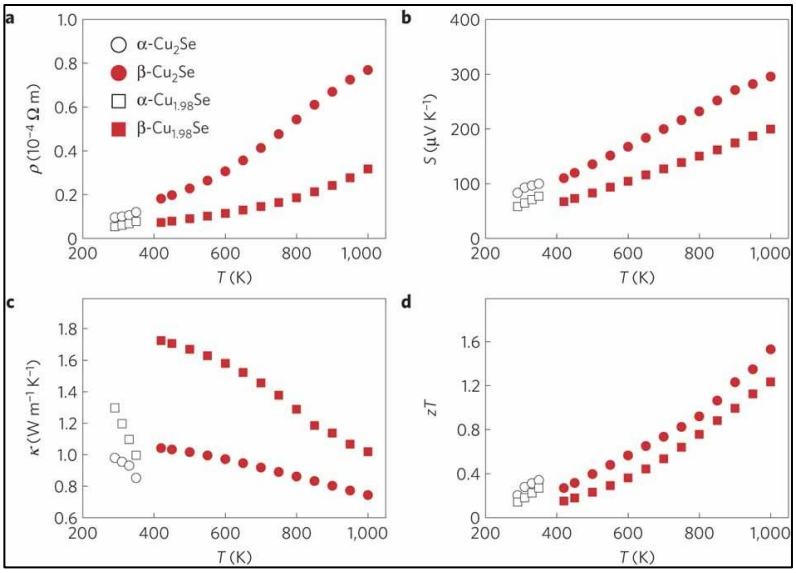

Figure 13: Thermoelectric properties of α and β phases in $Cu_{2-x}Se$. Adapted from Liu, et al. [57]

As discussed in the earlier sections, k is the sum of three components, i.e., electronic contribution (k_e), lattice contribution (k_l), and bipolar contribution (k_b). The most direct

method to improve zT is by reducing the lattice contribution to the thermal conductivity through nanocomposites [77], [78]. The critical point in developing nanocomposites is to create grains that help in phonon scattering without affecting electron transport.

2.2.2. Copper Selenide synthesis techniques and their properties

Nanocomposites synthesized by high-energy ball milling with assisted hot pressing have improved zT. Yu reported a maximum zT of 1.6 for β-phase Cu_2Se synthesized using ball milling and hot pressing at 700 ℃. They also reported a low lattice thermal conductivity of 0.4-0.5 W/mK. The β- phase turns into α- phase on cooling, and this phase transition is reversible. The cubic β-phase has a smaller unit cell with a= b= c= 5.8639 Å at 200 ℃. The authors also studied the composition effect on the TE properties by varying the amount of Se in the starting compositions. The Seebeck coefficient and electrical resistivity decreased with increasing the selenium content due to the increased concentration of holes caused by many Cu vacancies [79]. Copper selenide synthesized by Bulat et al. [80] is reported to have a maximum zT value of 1.8. A mechanochemical process was used to synthesize the nanopowders by ball milling of Cu powder and Se grains. These obtained high zT was attributed to the low thermal conductivity of the synthesized materials. Theoretically predicted zT was also consistent with the experimentally measured zT up to a temperature of 773 K [80]. Cu_2Se undergoes a structural phase transition at 130 ℃ from the α-Cu_2Se (monoclinic) phase to a cubic β-Cu_2Se phase [81]. Tafti et al. [82] synthesized nanostructure copper selenide (Cu_2Se) using microwave-assisted thermolysis with an average particle size

of 150 nm ±20 nm, and the powders were then compacted using spark plasma sintering (SPS). The synthesized samples were reported to have a high-power factor and low thermal conductivity. A zT value of 2.0 was found at 900 K, one of the highest reported values. The figure of merit of the nanostructured Cu_2Se is increased by around 60% compared to the bulk samples [82].

Table 2: Synthesis methods for copper selenide

Growth Technique	Main Precursors	Process Conditions	Application	Product	Ref
Ball Milling	Cu and Se elemental powder	Milling time of 8-50 h at 400-500 rpm under Ar. Process control agents, e.g., stearic acid and n-heptane	TE	β-phase Cu_2Se with ordered Se and disordered Cu layers	[79]
				Nanostructured $Cu_{1.98}Se$ with 12 nm crystallite post-SPS	[83]
				Monoclinic and cubic Cu_2Se, small grain boundaries, and pores	[84]
				Monoclinic Cu_2Se. Grain size of 20 nm	[85]
				Nanostructured Cu_2Se. Crystallite size ~11 nm.	[86]
Melting	Cu and Se elemental powder	T = 1423K for 10-12 hr.	TE	Polymorphic $Cu_2Se_{1-x}S_x$ *at room temperature*	[87]
				$Cu_{2-y}Se_{1-x}Br_x$ doped with Br to reduce hole concentration	[88]
				$Cu_2Se_{1-x}S_x$. Mixture of trigonal and cubic phases. Thickness < 100 nm	[89]
				$Cu_{2-x}Se$ ingots	[57]
				Trigonal $Cu_2Se_{1-x}Te_x$. 100 nm thickness	[90]

Chemical Synthesis	CuCl and Se powder	RT to 250 C. Duration: 5 mins (MW thermolysis) to 2 hr.	TE	**Co-precipitation:** Cu_2Se nanoflowers. Average size of 150-500 nm. **Reduction:** Irregular hexagonal Cu_2Se nanoplates (100 nm)	[91]
	Copper Acetate and Se powder			β-Cu_2Se nanoparticles with an average size of 150 nm	[82]
	$CuSO_4$ and SeO_2			β-Cu_2Se nanoparticles with spherical morphology with a diameter ~75 nm	[92]
Solvothermal/ Hydrothermal	Copper salts and Se	Autoclave. T = 100 – 230 C for 1 - 24 h	None REPORTED	CuSe, β-Cu_2Se, Cu_2Se, and $Cu_{2-x}Se$ for different Cu precursors	[93]
	$CuSO_4$ and SeO_2			Cu_2Se hexagonal flakes ~ 100-200 nm	[94]
	Copper foil and Se			Cu_2Se nanowires. Length up to 50 μm.	[95]
	$CuSO_4$ and SeO_2		TE	Cu_2Se nanopowders with spherical morphology, size about 100 nm- 1.2 μm	[96]
	CuO and SeO_2			β-phase Cu_2Se hexagonal nanoplatelets. Grain size ~ 30 nm.	[97]
			Battery	$Cu_{2-x}Se$. Nanocrystals size 10-130 nm	[98]
	Copper acetate and Sodium Selenite			$Cu_{2-x}Se$@C nanosheets. Thickness 20-50 nm	[99]
				Cubic $Cu_{2-x}Se$ nanosheets. diameter ~300 nm	[100]
	Cu foam and Selenourea			Cu_2Se nanoflakes. ~100 nm thick on Cu foam substrate	[101]
	Cu foil and Se with CTAB	RT for 2 h		Cu_2Se- CTAB nanosheets	[102]

Solid-state reaction	Cu and Se powder		TE	$Cu_{2+x}Se$- RGO composites with enhanced chemical stability	[103]

2.2.3. Effect of doping on the properties of copper selenide.

The zT of Cu_2Se at room temperature was found to be improved via doping. Liu et al. [58] reported a zT of ~ 2.3 at 400 K at the phase transition in Iodine-doped Cu_2Se. The critical phase transition temperature can be modified to around room temperature by iodine doping. The scattering significantly increases the thermopower and decreases thermal conductivity, leading to a high zT value [58]. Studies have been carried out even at very low temperatures. A figure of merit of 0.14 was reported by Yao et al. [81] at 200 K in doped p-type α-phase Cu_2Se. This layered structure was developed using ball-milling and studied with different dopants like Tellurium, Nickel, and Zinc. However, the parent compound Cu_2Se was reported to show a higher zT value over the doped compounds. Kang et al. [104] reported an increased zT value of 1.4 by doping copper selenide with lithium. Superionic compounds are known to have thermo and electromigration due to the diffusive cation, and this bipolar conduction was forcibly put to a decrease by lithium doping [104]. Another study by Hu et al. [105] also reports the same conclusion. Lithium-doped Cu_2Se samples were prepared by hot-pressing the powders that were obtained from hydrothermal synthesis. The addition of Li

increases the Seebeck coefficient and reduces the k_l due to increased phonon- scattering. A zT value of 2.14 was reported for the $Cu_{1.98}Li_{0.02}Se$ sample at 973 K [105].

Peng, et al. [106] reported a decrease in the electric resistivity. The carrier concentration was changed when Cu_2Se was doped in the following stoichiometric composition $Cu_{1.99}A_{0.01}Se$ (A= Fe, Ni, Mn, In, Zn or Sm). This, in turn, enhanced the value of the power factor. All the doped samples except the In-doped sample showed better thermoelectric properties. The highest zT was obtained for the Ni-doped sample, and the value was around 1.51 at 823K [106]. A few more information on other doped sample studies is summarized in Table 2.

Table 3: Thermoelectric Properties of Doped Copper Selenide

Filler	**Preparation Technique**	**T (K)**	**zT**	**Developed size**	**Comments**	**Ref.**
Iodine	Vacuum melting and spark plasma sintering	400	2.3	Ingots	Ultra-high Thermoelectric performance	[58]
Lithium	Lithium doped using mechanical alloying	1000	1.4	Ingots	Copper selenide was doped with lithium to suppress the Cu ion diffusivity	[104]
Fe	Conventional melting, ball milling and quenching route, followed by a spark plasma sintering technique.	823 (Ni)	1.07	Ingots	T= 823K, Doping did not change structure of Cu2Se, p-type conduction	[106]
Ni			1.51			
Mn			1.28			
Sm			1.07			
Zn			1.25			
Ag	Melting elemental Cu, Ag, Se and then ball-milled to form powders.	870	1.0	Ingots	Ag doping reduces Hall carrier concentration, zT of Cu2Se can be increased by reducing Hall carrier concentration. We do not require Ag; any other means would suffice.	[107]
Te	Solvothermal	400-850	~1.2	1.5 μm	Te doping made the phase transition to α- phase. Low k via nanostructuring and Te doping	[108]

K	Hydrothermal+ Hot-press sintering	773	1.19	-	Doping of K brings micro-pore structure to decrease thermal conductivity	[109]
Li	Hydrothermal	973	2.1	100-500 nm	Reduction in k_l due to phonon scattering	[105]
Na	Hydrothermal	973	1.32	-	Carrier concentration increases, decreased k_l.	[110]

2.3. Nanostructured Thermoelectric Material-Graphene Composites

2.3.1. Graphene

Graphene is the building block of graphite. It is a single layer of carbon atoms in a tightly packed honeycomb two-dimensional lattice, as shown in Figure 14. Graphene was discovered by K. S. Novoselov and A. K. Geim in 2004 when they tried to separate flakes from bulk graphite using scotch tape [111]. Moreover, since its discovery, numerous applications have been used due to its remarkable physical properties that would pave the way for extensive research in the nanoscale industry [111-115].

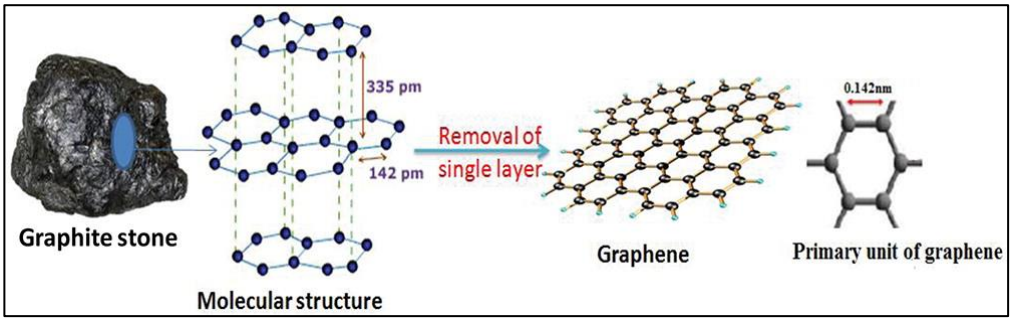

Figure 14: Schematic depictions about the origin (presenting the transformation) of graphene from graphite and peculiar structure of graphite and graphene. Adapted from Tiwari, et al. [116].

It is made up of sp^2 hybridized atoms arranged in a lattice structure [117, 118]. The unit cell for graphene is a two-dimensional rhombus, and two atoms are present per unit cell, as shown in Figure 15 [119]. Graphene has exceptional thermal and electrical properties. Graphene has a thermal conductivity of 3000-5000 $Wm^{-1}K^{-1}$ at room temperature [120]. P.R Wallace was the first to perform band structure calculations on graphene [121]. Pristine graphene is found to be a zero-bandgap semiconductor as the conduction and valence bands touch at the Dirac point [122, 123]. The graphene unit cell is a two-dimensional rhombus, and two atoms are present per unit cell, as shown in Figure 16 [119]. The carrier mobility of graphene at room temperature was found to be around 10,000 $cm^2V^{-1}s^{-1}$ with a specific area of 2630 m^2g^{-1}. Young's modulus is as high as 1 TPa [118] and ultimate strength of 130 GPa, making single-layer graphene the strongest ever material to be measured [124]. Graphene exists in various dimensions, namely zero-dimensional (0D) fullerenes, 1D nanotubes, or stacked as 3D graphite, as shown in Figure 16**.**

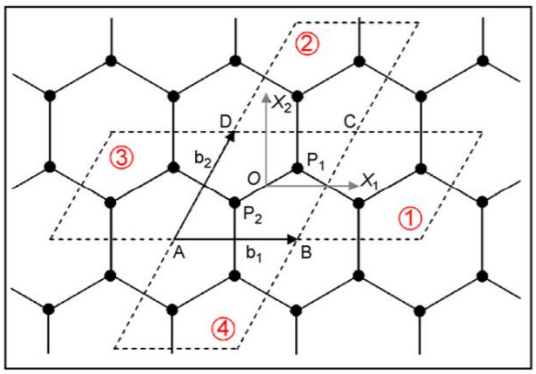

Figure 15: Two-dimensional rhombic unit cell ABCD of graphene surrounded by four neighboring unit cells. Adapted from Zhou and Huang [119].

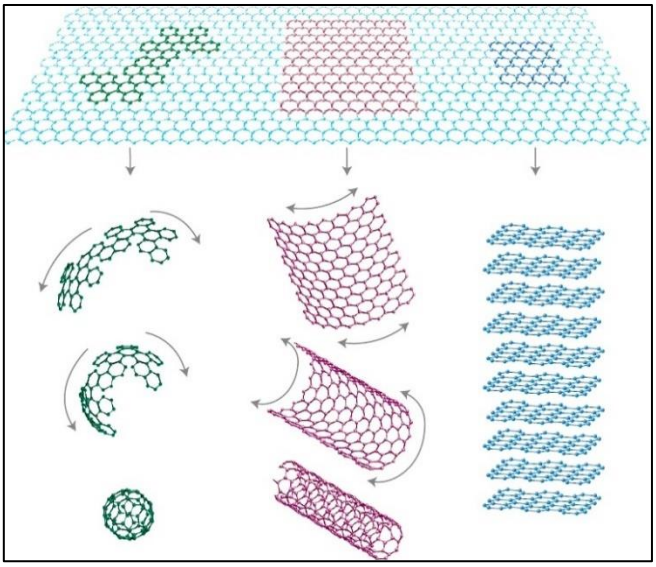

Figure 16: 2-D graphene is regarded as the building block for other carbon materials. It can be wrapped into 0D fullerenes, rolled into 1D nanotubes, or stacked into 3D graphite. Adapted from Kakaei et al. [125].

Over the years, graphene has garnered interest due to its exceptional and mind-boggling properties, which can be exploited in various ways. It has been used widely in sensors, biomedicals, fuel cells, and nanocomposite materials [112, 114-116, 126]. Graphene also improves the efficiency and performance of Pt nanoparticles [118].

Bulk graphene has one of the highest thermal conductivities [127-129], and due to that, its overall zT is relatively low [130]. Even though this poses a threat to the TE performances, there are numerous ways to decrease the thermal conductivity of graphene by introducing defects [130], edge-passivation by hydrogen [131], by patterning [132, 133], and by nanostructuring [134]. Graphene also strengthens the bulk materials' mechanical properties, as this criterion is essential for device fabrication [135].

2.3.2. Thermoelectric Material-Graphene Nanocomposites

Graphene has been added to improve the thermoelectric performance with other nanocomposites to increase the figure of merit. The electrical conductivity of materials is enhanced by incorporating graphene at very low vol% due to its high electrical conductivity and high aspect ratio [136]. Xie, et al. [137] reported increased electrical conductivity by adding graphene into MoS_2 nanomaterials. The addition of graphene provides more electron transport channels in the nanocomposite. Wang et al.[138] prepared Polyaniline (PANI)/graphene nanocomposites in which the structural defects and the amount of oxygen content in the graphene affect the thermoelectric performance of the composites. In composite films prepared with graphene, TE properties were high and increased with graphene content, as shown in Figure 17 [138].

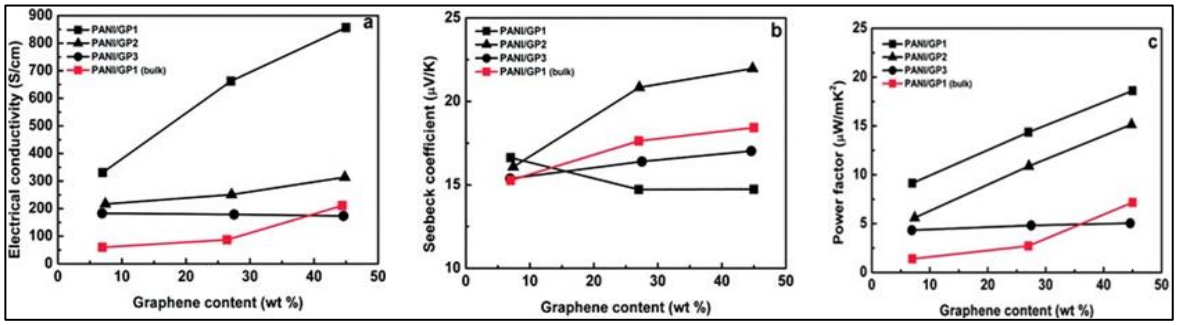

Figure 17: Electrical conductivity (a), Seebeck coefficient (b), and power factor (c) of bulk PANI/graphene composite films. Adapted from Wang et al. [138]

Ahmad et al. [139] reported that the addition of graphene into nanostructured $BiTe_3$ produced by ball milling enhanced the material's thermoelectric properties. The incorporation of graphene decreased thermal conductivity because of enhanced phonon scattering [139].

Li et al. [140] reported an increase in zT of Cu_2Se incorporated with graphene nanoplates. A zT= 2.44 was reported at 873 K, which is very high and a record number in the field of study. The nanocomposite material was prepared using ball milling and melt quench to incorporate graphene nanoplatelets into the copper selenide matrix. The graphene-incorporated β-Cu_2Se has a lattice parameter of 5.857 ± 0.005 A. The electron microscopy showed the graphene incorporated copper selenide with a primary Cu_2Se phase and a secondary honeycomb structure. Incorporating graphene lowers the PF, but the drastic reduction in the thermal conductivity overcomes that reduction in PF, leading to enhancement in zT. The study also reported an increase in zT with the graphene content of up to 0.3 wt%. A maximum zT of 2.44 was observed at 0.15 wt%. The main observation was the control of the thermal conductivity by the incorporation of graphene [140].

Li et al. [141] reported a study on graphene's synthesis and TE properties- incorporated Cu_2Se nanocomposites. The graphene- copper selenide nanocomposites were fabricated using ball milling followed by SPS. The material's thermal conductivity is decreased in the GNP incorporated sample compared to the pure sample, thereby enhancing the thermoelectric figure of merit. The zT values increase with the increase in doping concentration with a

maximum zT value of 1.8 at 873 K (0.25 wt% GNP- Cu_2Se sample), whereas the undoped sample had a zT value of 0.9 at the same temperature (873 K) [141].

Table 4: Thermoelectric figure of merit of various Cu_2Se – carbon nanocomposites.

Carbon source	Preparation Method	zT		T(K)	Developed size	Ref
		Control	Composite			
Carbon nanodots	Hydrothermal	~1.3*	1.98	973	50-100 nm hexagonal nanoplates	[142]
Carbon nanotubes	Ball Milling+ SPS	1.5	2.4	1000	-	[143]
Carbon fibers	Melt solidification	1.25	2.4	850	30-60 nm (Cu_2Se)	[144]
Graphene	Ball milling+ SPS	0.9	1.8	873	$\sim 50\ \mu m$	[141]
Graphene	Ball milling and melt quench	1.1	2.44	873	-	[140]

*Reading from graph

Zhao, et al. [144] also reported enhancing zT of copper selenide by incorporating various carbon sources. The authors noted that a small number of carbon fibers increased the zT significantly with a maximum zT of 2.4 at 850 K reached with 0.3 wt.% carbon-doped Cu_2Se. The inclusion of a carbon source reduces copper ion diffusion, which hinders practical applications at high temperatures. Generally, the thermoelectric performance at moderate temperatures (500-750 K) is unsuitable for practical applications as the $zT < 1$. This specific sample also showed a $zT > 1$ for temperatures above 520 K. The fabrication of Cu_2Se with carbon develops nanostructured interfaces that significantly decrease the thermal conductivity by increasing the boundary's resistance. Cu_2Se based nanocomposites are less

toxic, with low-cost fabrication methods paving the way for state-of-the-art TE materials [144].

The current research focuses on utilizing graphene's remarkable electrical and transport properties with copper selenide's available intrinsic properties. As seen in Table 4, many of the syntheses use mechanical methods to fabricate the sample. At the same time, this research focuses on a hydrothermal approach that is cost-efficient, scalable and has better nucleation control. The morphology/ structure of the material can be controlled with reaction temperature, solvents, type of precursors, and capping agents. The enhancement of the figure of merit is of prime importance in thermoelectric materials to incorporate them for energy applications, and nanocomposite fabrication is proved to be an excellent approach for improving zT.

3. RESEARCH OBJECTIVES

This research aims to enhance the properties of thermoelectric materials of copper selenide by fabricating nanocomposites with graphene.

The aim of this research will be met by accomplishing the following objectives:

1. Preparation of copper selenide and copper selenide-graphene composites with different concentrations of graphene.
2. Characterization of the as-prepared thermoelectric materials to establish the correlation between graphene content and its effect on the materials' properties.
3. Assessment of the thermal stability of the pure CuSe and its graphene nanocomposites
4. Improvement of the thermal stability of the as-synthesized nanopowders via thermal treatment.
5. Analysis of the thermoelectric performance of the pure and nanocomposites for the optimum graphene concentration pre and post thermal treatment.

4. METHODOLOGY

4.1. Copper Selenide Fabrication

For the preparation of Copper selenide (Cu_2Se), copper sulfate pentahydrate ($CuSO_4 \cdot 5H_2O$), selenium dioxide (SeO_2) were used as precursors. 9.692 g (38.82 mmol) of $CuSO_4$ and 2.154 g (19.41 mmol) of SeO_2 were added (2:1 mole ratio) to a 200 mL beaker containing 160 mL of deionized water. The solution was stirred for 10 minutes using a magnetic stirrer to ensure that no clumps of the precursors remained. It was then probe sonicated for 10 minutes (30 seconds on, 30 seconds off). The reducing agent used for this process was hydrazine hydrate $N_2H_4.H_2O$. 12 mL of the reducing agent was added to the prepared precursor mixture. This solution was then transferred to a 200 mL Teflon liner, placed in an autoclave, and kept in the oven at 180 ˚C for 24 hours. After heating, the autoclave was then removed from the oven, and it was cooled down to room temperature naturally. The product was collected by centrifugation by washing twice with HCl followed by four times with water and ethanol. The material was then dried at 80 ˚C under vacuum until a constant mass was achieved (4 h).

Cu^{2+} and Se^{4+} being highly active, are reduced by hydrazine, which then combines to form Cu_2Se. The reaction mechanism is as follows:

$$SeO_2 + H_2O \rightarrow H_2SeO_3 \quad (4.1)$$

$$H_2SeO_3 + N_2H_4.H_2O \rightarrow Se + N_2 \uparrow + 4H_2O \quad (4.2)$$

$$2CuSO_4 \cdot 5H_2O + N_2H_4 \cdot H_2O \rightarrow 2Cu + 2H_2SO_4 + N_2\uparrow + 6H_2O \quad (4.3)$$

$$2Cu + Se \rightarrow Cu_2Se \quad (4.3)$$

4.2. Copper selenide-graphene composite

For the preparation of copper selenide-carbon composite, a similar procedure to pure copper selenide preparation was followed. The preparation of the precursor mixture was unchanged, but different quantities of DI water were used instead. For the carbon, a graphene oxide (GO) precursor was used. Different amounts of 2 mg/mL graphene oxide were used. Two graphene oxide solutions were used to make the composites.

The GO prepared using Hummer's method (1958) involved oxidation of graphite by potassium permanganate, sodium nitrate, and concentrated sulfuric acid. GO produced using Hummer's method is one of the most used commercial methods due to its reduced production cost [145]. The most recent popular technique was James Tours, who enhanced the existing Hummer's method. This method used phosphoric acid instead of sodium nitrate and was introduced in 2010. This modification lessens the toxicity of the solution since hazardous gases such as nitrogen dioxide and dinitrogen tetroxide are emitted in Hummer's approach, which is not present in Tour's synthesis [146]. Graphene oxide prepared using Tour's method was synthesized in our lab, and graphene oxide prepared using Hummer's method was obtained commercially.

The graphene oxide solution preparation is the same for both types. A solution was made in 100 mL DI water for all the different masses. It was bath sonicated for 15 minutes, followed by probe sonication for 5 minutes (30 seconds on, 30 seconds off). The precursor solution, the graphene oxide solution and 12 mL hydrazine were added to a 200 mL Teflon liner. The

liner was then placed in an autoclave and kept in the oven at 180 ˚C for 24 hours. The autoclave was then removed from the oven, and the product was collected by filtration in a dead-end cell using N_2. The material was then dried at 80 ˚C in a vacuum.

Table 5:Mass of the precursors used for the synthesis of $Cu_{2-x}Se$ and $Cu_{2-x}Se$ -graphene nanocomposites

Precursor	Mass				
	% GO				
	0	0.05%	0.1%	0.25%	0.5%
$CuSO_4.5H_2O$	9.69				
SeO_2	2.15				
GO (mg)	0	5.7	11.4	28.7	57.1

The nanostructured powders were consolidated using hot pressing under an argon atmosphere. The powder was loaded and pressed under a uniaxial pressure of 1 GPa at 300°C for 5 mins. The consolidated discs were of 12.7 mm diameter with a thickness of 3 mm.

4.3. Characterization

Various characterization tests were carried out on the synthesized samples to understand their physical and chemical properties. The tests performed for analysis and testing of the prepared materials are summarized in Table 6

Table 6: Characterization tests performed on the synthesized samples.

Material	XRD	XPS	SEM	EDS	DSC	TGA	Seebeck Coefficient	Electrical Conductivity	Hardness
Cu-Se (1:1)	✓	✓	✓	✓	✓	✓			

Cu-Se (2:1)	✓	✓	✓	✓	✓	✓	✓	✓	✓
Tours GO Composites (%GO)									
0.05%	✓	✓	✓	✓	✓	✓	✓	✓	✓
0.1%	✓	✓	✓	✓	✓	✓	✓	✓	✓
0.25%	✓	✓	✓	✓	✓	✓			
0.5%	✓	✓	✓	✓	✓	✓			
Hummer's GO Composites (%GO)									
0.05%	✓	✓	✓	✓	✓	✓	✓	✓	✓
0.1%	✓	✓	✓	✓	✓	✓	✓	✓	✓
0.25%	✓	✓	✓	✓	✓	✓			
0.5%	✓	✓	✓	✓	✓	✓			

4.3.1. Chemical and Structural Properties

4.3.1.1. X-Ray Diffraction (XRD)

X-ray diffraction is a non-destructive technique to study the crystallographic structure of a material. The periodic arrangement of atoms in a crystal diffracts light, thus producing significant peaks due to monochromatic X-ray beams' constructive interference at specific angles. This diffraction pattern holds information about the arrangement of atoms in a material.

The XRD data can also obtain parameters such as average grain size, crystallinity, strain, and crystal defects. The diffraction from a crystal can be outlined based on Bragg's law, which is given by $\lambda = 2\,d\sin\theta$ (4.4)

where d is the interplanar spacing, λ is the wavelength of the X-rays, and θ is the angle between the incident beam and the Bragg plane [147, 148].

The crystal size is determined according to Scherrer's equation given by:

$$D = \frac{0.9\lambda}{\beta_d} . \frac{1}{\cos\theta} \quad (4.5)$$

where λ and θ are the same as Bragg's law, and β is the full width at half maximum (FWHM). However, Scherrer's equation has a limitation. The assumption that only the crystals' size affects the peak broadening is inaccurate, as it does not consider the stress-induced broadening, the effect of ambient temperature, and lattice strain on the width of the peak [149, 150]. There are several other methods used to overcome the pitfalls of Scherrer's equation:

4.3.1.1.1. Williamson- Hall (WH)

Williamson-Hall is a better method than Scherrer's in determining the size as it acknowledges the peak broadening due to lattice strain and not just the crystallite size. As a result, the FWHM according to W-H is given by

$$\beta_{hkl} = \beta_{size} + \beta_{strain} \quad (4.6)$$

where β_{hkl}, $\beta_{size,}$ and β_{strain} are the peak broadening, peak widths due to the grain size, and lattice strain. We obtain the size from the intercept and the strain component from the graph's slope [149].

4.3.1.1.2. Warren-Averbach (W-A)

Warren- Averbach method is another size/strain analysis that uses a Fourier – coefficient analysis model. This model can calculate the size of a curve of any shape provided the tails are appropriately truncated. This method is found to be in good accordance with the crystallite size determined experimentally [151].

4.3.1.1.3. Size Strain Plot (SSP)

The SSP model offers more significance to the low angle XRD peaks as those areas have high accuracy and precision than higher diffractions angles where peaks generally overlap. The SSP plot models the size broadened part as a Lorentzian function and the strain broadened part as a Gaussian function [152].

For this research, the XRD was carried using Rigaku Ultima IV X-ray Diffractometer in a scan range of 5˚ to 80˚, with a speed of 1˚/minute. CuK (alpha) (0.1542 nm) radiation at 40 kV and 30 mA was used in this analysis. Figure 18 shows an X-ray Diffractometer

Figure 18:Rigaku Ultima IV X-ray Diffractometer

4.3.1.2. X-ray Photoelectron Spectroscopy (XPS)

X-ray Photoelectron Spectroscopy (XPS) is a non-destructive surface characterization technique that bombards the material's surface with X-ray photons under a vacuum. The electrons absorb photons corresponding to a particular energy level in the material. The electrons released are unique for each element, which aids in obtaining the material's elemental composition. XPS can also give us information on the chemical state of the element based on the binding energy. For this project, XPS was used to determine copper and selenium's chemical state in their compounds. It was also used to obtain each element's quantification – how much was present in each sample. This test can also show if there are oxides present [148, 153]. Figure 19 depicts an X-ray Photoelectron Spectroscopy from Kratos Analytical.

Figure 19: X-ray Photoelectron Spectroscopy from Kratos Analytical

4.3.1.3. Scanning Electron Microscopy (SEM)

Scanning Electron Microscopy (SEM) is a well-known technique to obtain images of a material's surface. The scanning electron microscope scans the material with a focused

electron beam and gathers the secondary or backscattered electrons from the sample. SEM provides high magnification, high-resolution images of the surface. Different detectors collect the emitted particles to yield the results. X-rays are also generated due to the incident beam, which is characteristic of a particular element and helps collect the elemental information (discussed in the next section). The analysis was performed on the Thermo Fisher Scientific Apreo SEM in high vacuum and 30 kV [153, 154].

4.3.1.4. Energy Dispersive X-ray Spectroscopy (EDS)

Energy Dispersive X-ray Spectroscopy (EDS) is utilized to identify the sample's elemental composition by collecting characteristic x-rays generated from the material's surface during SEM analysis using a specialized detector. The X-rays are collected and categorized automatically since each element has characteristic energy for the X-ray photons emitted [153, 154]. The EDS was performed in conjunction with the SEM, using the EDAX Octane Elect EDS System.

4.3.2. Thermal Properties

4.3.2.1. Thermal stability

Thermogravimetric analysis is used to determine the thermal stability of a material. It also measures the composition of volatile compounds in the material. The material's weight change is monitored as the sample is heated to a higher temperature at a constant rate. The heating is carried out in a controlled atmosphere where the purge gas is nitrogen. The curve obtained is the weight change against the temperature can also determine any decomposition,

oxidation, dehydration, and pyrolysis during heating [155]. TGA was carried on a Perkin Elmer TGA, a temperature range of 50 ˚C to 900 ˚C under nitrogen at the rate of 20˚ C/minute.

4.3.2.2. Thermal Transitions

Differential Scanning Calorimetry (DSC) is a thermal analysis technique. The difference in the amount of heat required to raise a material's temperature and reference material is recorded as a temperature function. It is a useful analysis to gauge if a sample undergoes physical or chemical changes. Both the sample and the reference are maintained at the same temperature throughout the experiment. The melting point, specific heat capacity, heat of fusion, and heat of vaporization of a material can be obtained from this technique [155]. For this research, DSC was carried out from 50 ˚C to 400 ˚C for two cycles at 20 ˚C/ min using Perkin Elmer Pyris.

4.3.3. Thermoelectric property measurement

Compaction of powders was done for all samples using hot- pressing at 300 °C for 10 minutes under high-purity argon. This temperature was chosen based on the stability of the prepared copper selenide.

Electrical conductivity and the Seebeck coefficient are essential in understanding the TE behavior of a material. The consolidated samples' properties are measured using NETZSCH SBA-458 as shown in Figure 20 from room temperature to 573 K under Argon atmosphere.

The sample is held between a pair of micro heaters, current pins, and thermocouples. The microheaters heat alternatively to maintain a temperature gradient. The temperature gradient will generate a potential difference/voltage between the thermocouples. Each measured voltage is plotted against the temperature to obtain the Seebeck coefficient. Similarly, the electrical conductivity is measured by passing different current values through the current pins and then measuring the resulting voltage across the ends.

Figure 20: NETZSCH- SBA-458 Nemesis instrument

4.3.4. Mechanical Properties

4.3.4.1. Hardness Measurement

To analyze the mechanical properties of the synthesized materials, the microhardness of these materials was measured. For these measurements, the nanopowders were pressed into small disks. A pyramidal indenter with a square base makes an indentation on the surface of the disk. The hardness of the material is determined by the prediction size of the indentation and the used load [156]. Figure 21 shows an illustration of the indenter and indentation.

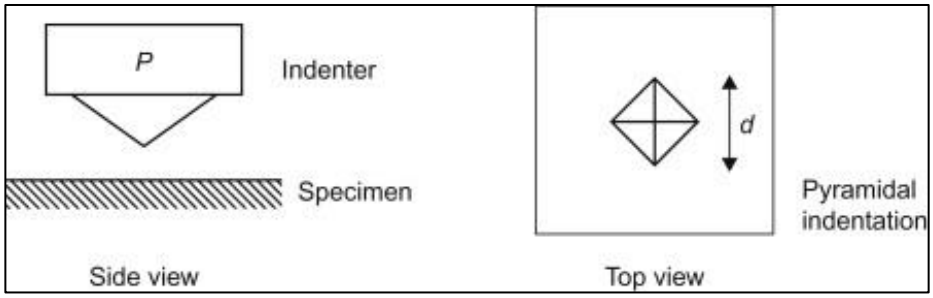

Figure 21: Indenter and indentation made for the microhardness measurements. Adapted from Smallman and Ngan [157]

5. RESULTS AND DISCUSSION

Pure copper selenide and copper selenide-graphene nanocomposites with different graphene concentrations were synthesized using the hydrothermal method detailed in Section 4. The yield of the as-synthesized products was above 90% for all materials. The first synthesis was produced using a 1:1 precursor ratio ($CuSO_4$:SeO_2) as a pilot study and a 2:1 ratio. As predicted, the first synthesis yielded CuSe as the product. The graphene composites were made for the 2:1 ratio only.

The chemical and structural properties of the materials were studied by performing XRD, XPS, SEM, and EDS on the synthesized materials. The XRD peaks were matched to the reference database from ICDD (The International Centre for Diffraction Data), and the crystallite size was calculated as detailed in Section 4.3.1.1. The XPS was done to analyze the samples' chemical state and composition, followed by SEM imaging and EDS mapping to find the chemical composition. The thermal properties of the sample were studied by their respective TGA and DSC scans. The samples were then consolidated into discs for TE property measurements.

5.1. Copper (II) Selenide (CuSe)

5.1.1. Chemical and Structural Properties

A 1:1 stochiometric ratio of the precursors was to synthesize pure CuSe. Figure 22 shows the XRD patterns for the pure CuSe. The observed XRD peaks correspond to CuSe-

Klockmannite (ICDD PDF Card No: 00-006-0427), confirming the pure successful synthesis of CuSe. The identified lattice plane (006) has the highest intensity. The interplanar spacing of 0.29 nm was obtained for the (006) plane using Bragg's law.

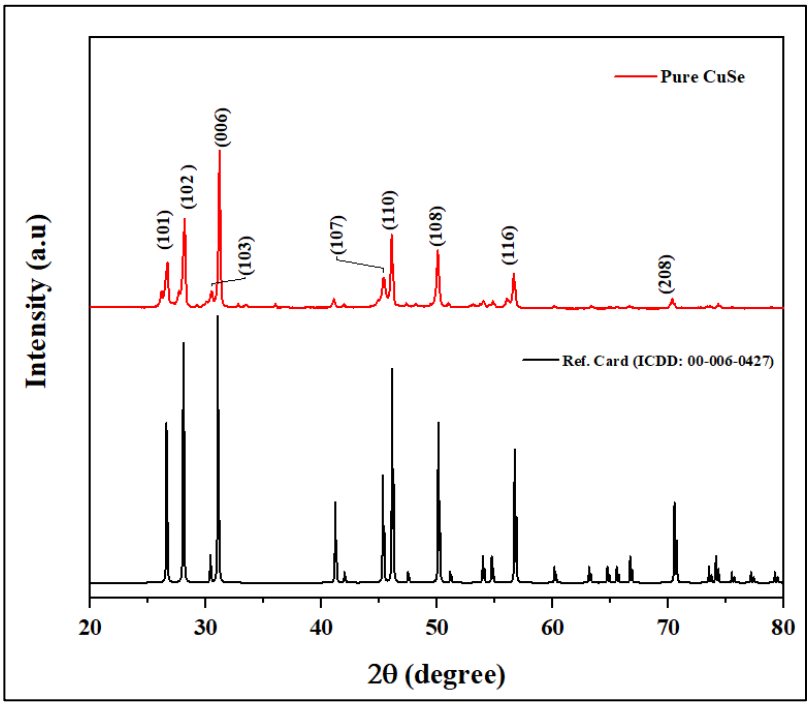

Figure 22: XRD plot of synthesized CuSe with standard PDF card (ICDD: 00-006-0427)

The grain size for the crystals was determined using Scherrer's, W-H, and W-A methods. WA method resulted in the best fit with an R^2 value of 0.94. The equation for the Warren-Averbach process is as follows:

$$\frac{\beta^2}{\tan^2\theta} = \frac{\lambda}{D}\left(\frac{\beta}{tan\theta\ sin\theta}\right) + 25e^2 \qquad (5.1)$$

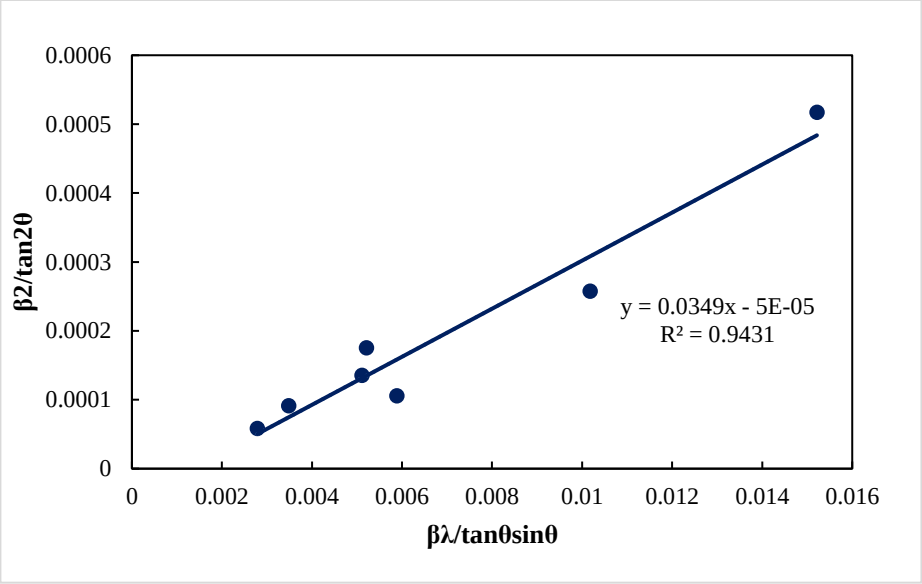

Figure 23: Warren- Averbach linear fit for CuSe nanocrystals.

Figure 23 shows a linear fit for $\frac{\beta^2}{\tan^2\theta}$ vs $\frac{\beta\lambda}{\tan\theta\sin\theta}$, the grain size and strain were obtained from the slope and the intercept, respectively. The grain size was 28.7 nm, and the strain was 0.14 %.

In addition to XRD, XPS analysis was performed to investigate the elements' chemical states and quantify their composition. Figure 24 (a) shows the survey spectra of the synthesized CuSe sample. Figure 24 (b) and (c) show the deconvoluted Cu 2p and Se 3d peaks. The Cu spectrum has only two significant peaks at (932.9 eV and 952.6 eV), corresponding to the Cu (II) ions in CuSe. The satellite labeled peaks confirm Cu^{2+} in the samples as satellite peaks are characteristic of the element's paramagnetic state. The shoulder peaks correspond to the presence of copper oxides in the model. The Se spectra have only two peaks (at 54.7 and 55.3 eV), which can be assigned to Se^{2-} ions in CuSe. The short, broad peak in Se 3d scan could

correspond to the formation of oxides on the surface. The Cu and Se content can be quantified from the peak areas of Cu 2p and Se 3d, tabulated in **Table 7.**

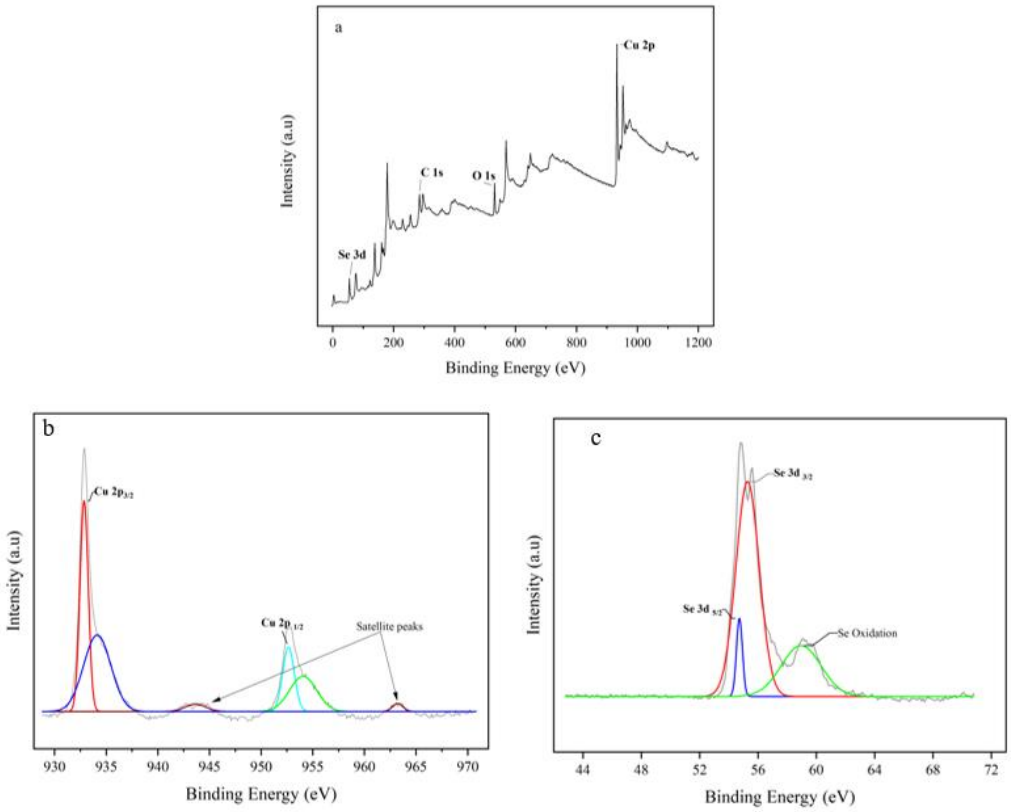

Figure 24: XPS (a) survey spectrum of pure CuSe and high-resolution spectra of the (b) Cu 2p and (c) Se 3d regions.

Table 7: Elemental composition of CuSe measured by XPS.

Composition (At. %)	
Cu	45.3
Se	23.9
O	30.8

Figure 25 shows the SEM images for CuSe. Hexagonally shaped nanostructures are visible in all images. No nanoparticle agglomeration was observed, although the edge length had a wide range of size distribution. The hexagonal plates showed a thickness varying from 34 nm to 40 nm, and the average edge length was 188 nm.

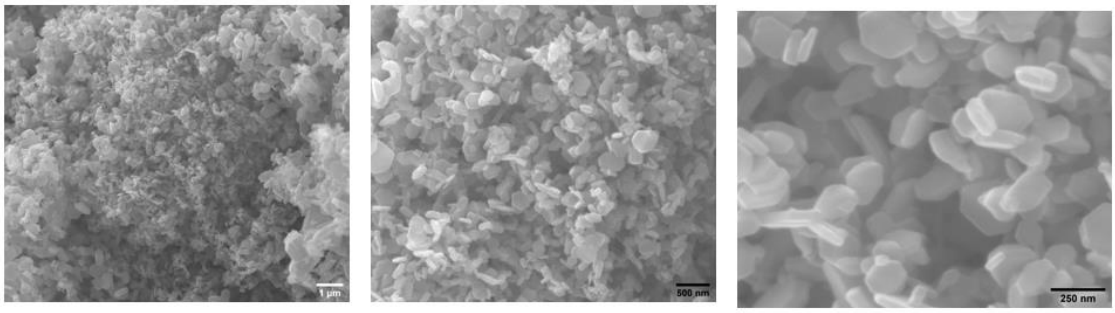

Figure 25: SEM images of CuSe nanostructures.

Table 8 represents the EDS analysis results of the CuSe sample. The results confirm the chemical composition with a 1:1 stoichiometry, indicating the material is CuSe, as per the 1:1 stoichiometry of Cu and Se atoms in the precursor. The atomic % of Cu and Se are 51 and 49, respectively. The elemental mapping of Cu and Se are shown in Figure 26.

Table 8:EDAX Quantification of as-synthesized CuSe

Composition (At. %)	
Cu	51
Se	49

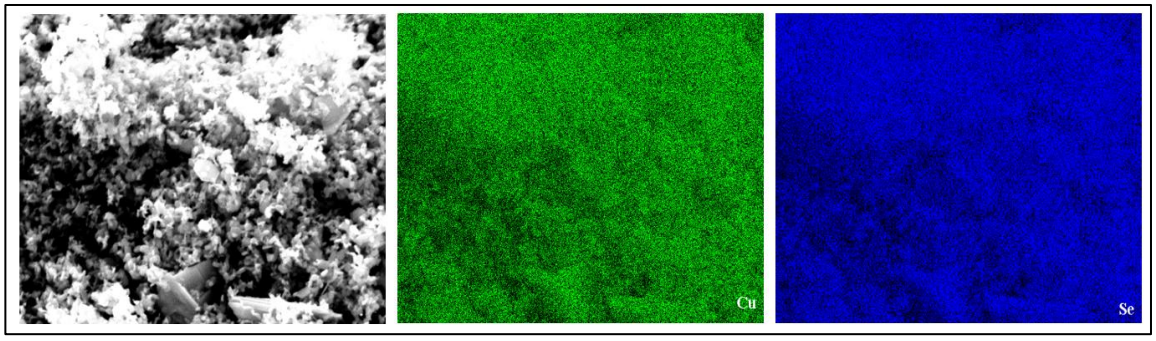

Figure 26: a) SEM and EDS mapping of b) Cu and c) Se of CuSe.

5.1.2. Thermal Properties

The thermal transitions of the CuSe nanomaterials were examined using DSC in the range of 25 to 400°°C. The melting point of the material is an essential criterion when the material is sintered for TE testing. Figure 27 shows the DSC and TGA of the CuSe sample. An endothermic peak is observed around 382 ℃, corresponding to the decomposition of CuSe to β-$Cu_{2-x}Se$ and Se [158].

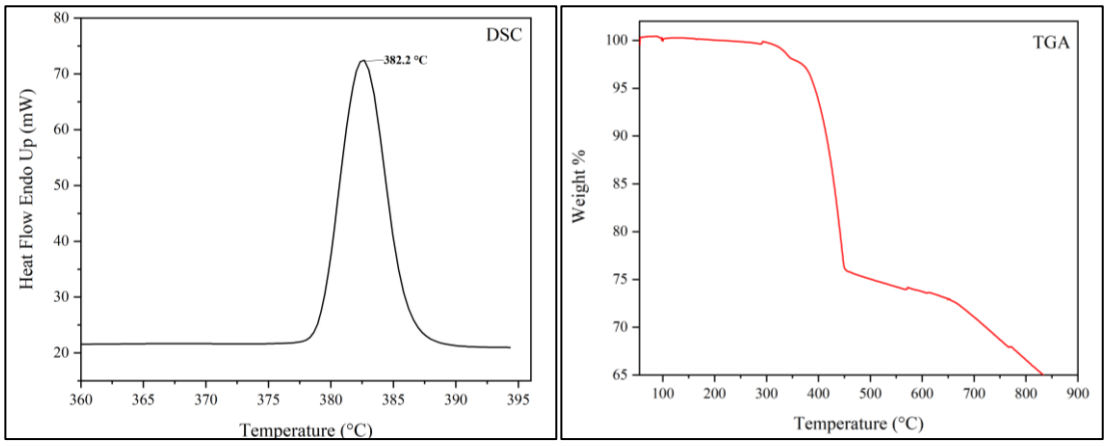

Figure 27: DSC and TGA curves of the CuSe nanocrystals.

The thermal stability of the materials was evaluated using TGA. The thermal stability of the TE material is essential as it dictates the temperature range of application. The 5% mass loss

temperature is at 423 ℃. The TGA thermogram in the region of room temperature to 900 ˚C is shown in Figure 26Figure 27. From the TGA thermogram, the decomposition of CuSe commences around 320 ˚C with a 37% weight loss of the sample, revealing the low thermal stability of the sample consistent with the literature [159, 160].

5.2. Copper (I) Selenide ($Cu_{2-x}Se$) and Copper Selenide- Graphene Nanocomposites

A 2/1 Cu/Se atomic ratio was used for the synthesis of Cu2Se and its GO nanocomposites. All the characterization tests performed for the CuSe were also carried out for the Cu2Se samples. The preparation method was identical to the CuSe sample synthesis except for the ratio of Cu/Se. The yield obtained was higher than 95% for all the materials.

5.2.1. Chemical and Structural Properties of $Cu_{2-x}Se$

Figure 28 shows the XRD pattern of the pure $Cu_{2-x}Se$ prepared using a 2/1 Cu/Se stoichiometric ratio. The XRD peaks match Berzelianite cubic $Cu_{1.8}Se$ (ICDD: 04-003-6777) belonging to the F-43m (216) space group. The lattice planes are identified as shown in Figure 28, with the peak of the (220) plane having the highest intensity. The interplanar spacing obtained for the pure copper selenide composites using Bragg's law for the (220) plane was 0.20 nm.

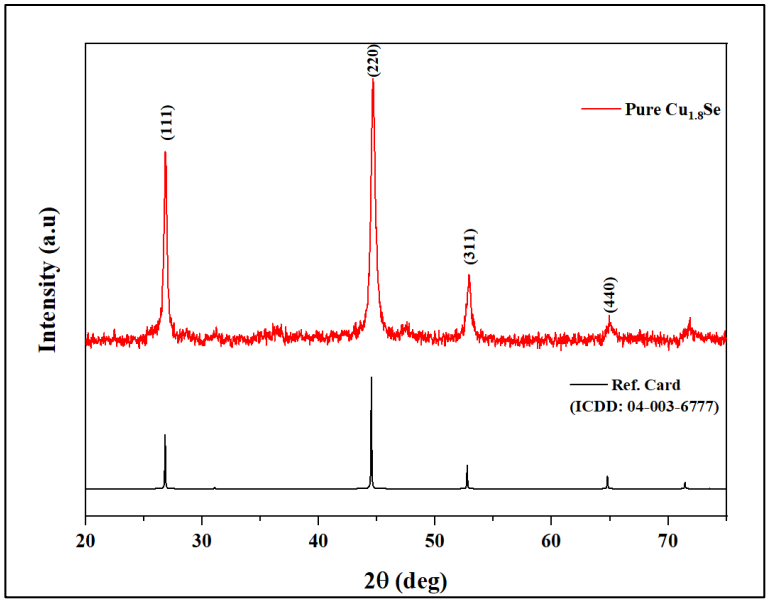

Figure 28: XRD plot of synthesized $Cu_{1.8}Se$ with standard PDF card (ICDD: 04-003-6777)

The grain size for the crystals was determined using Scherrer's, W-H, and W-A methods. The R^2 obtained from the Williamson-Hall method did not suggest a good fit. Hence, the WA method explained in Section 5.1.1 was followed. This method gave the best fit with an R^2 value of 0.96. The same trend was observed in all the composites, with WA having the best fit.

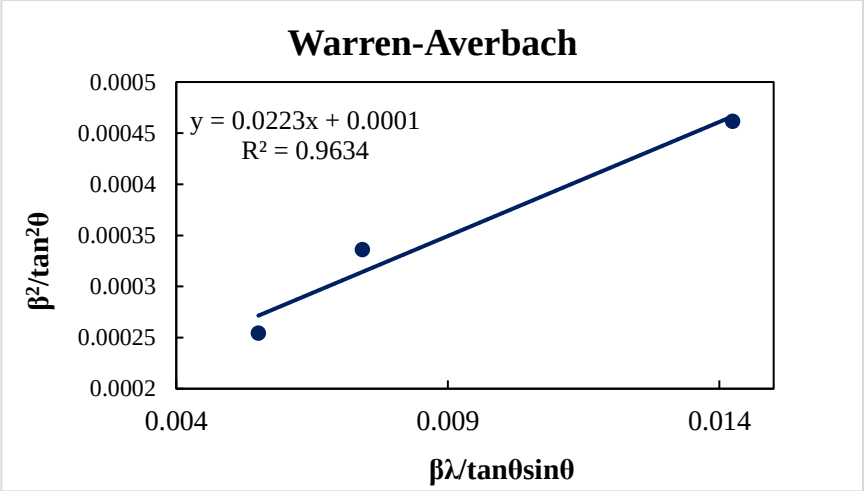

Figure 29: Warren-Averbach linear fit for pure $Cu_{1.8}Se$

Figure 29 shows a linear fit for $\frac{\beta^2}{\tan^2\theta}$ vs $\frac{\beta\lambda}{\tan\theta\sin\theta}$, the grain size and strain were obtained from the slope and the intercept, respectively. The grain size was 42 nm, and the strain was 0.2%. The cubic lattice parameter (a) for the pristine sample is 5.7427 Å.

In addition to XRD, XPS analysis was performed to detect the chemical state and composition of the synthesized $Cu_{1.8}Se$. XPS confirmed the synthesis of $Cu_{1.8}Se$ with both Cu and Se spectra showing peaks corresponding to $Cu_{1.8}Se$, as shown in Figure 30. Two peaks were observed for Cu 2p- at 933 eV and 953.1 eV, attributed to copper- Cu $2p_{3/2}$ and Cu $2p_{1/2}$. Selenium 3d scan shows two peaks at 54.5 eV, and 55.4 eV corresponds to the -2-oxidation state. Satellite peaks are marked in both the Cu and Se scans, indicating surface oxidation [161-163]. This does not affect the structure of the bulk phase, as the XRD analysis detected no oxide phases.

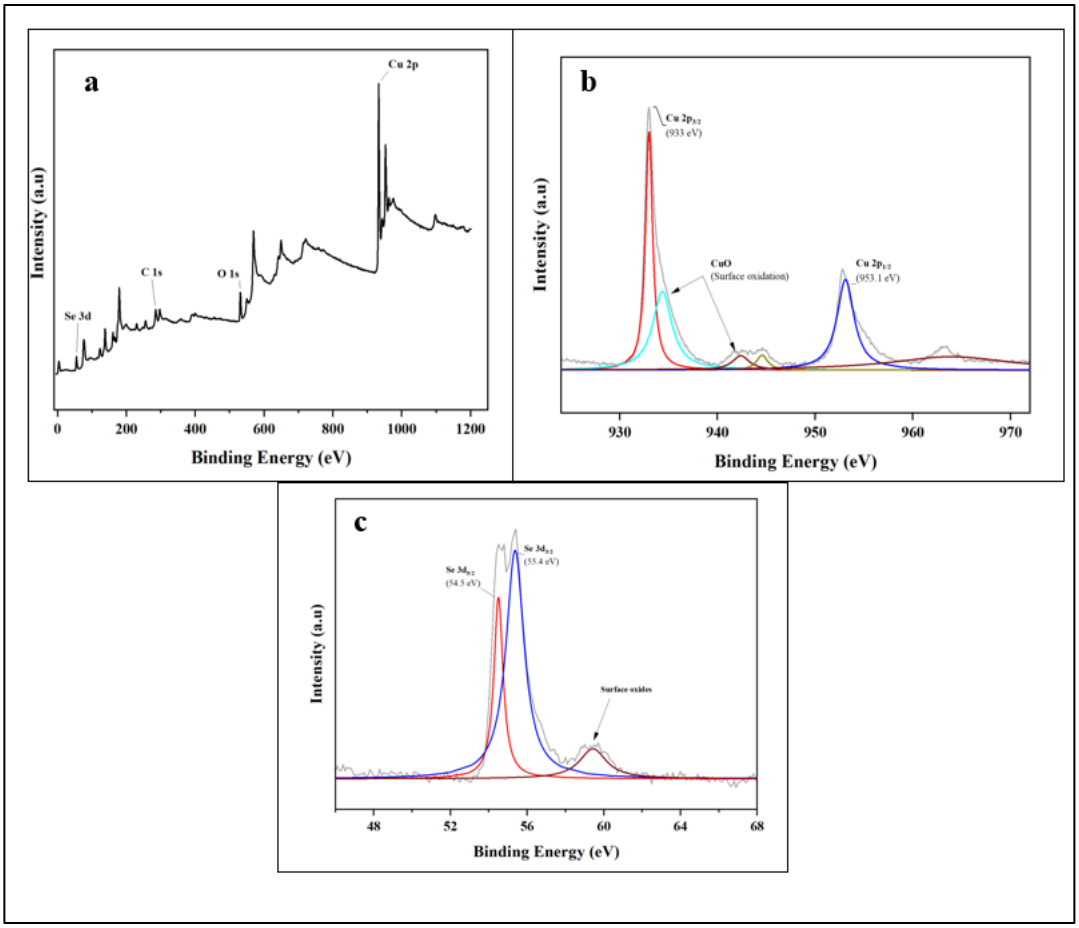

Figure 30: (a) Survey spectra obtained for pure $Cu_{1.8}Se$ (b) Copper – Cu 2p scan and (b) Selenium-Se 3d scan.

Figure 31 shows the SEM images for $Cu_{1.8}Se$. Spherical nanoparticles of various sizes are present in all images. They are irregular in shape, and their size ranges from 50-100 nm. There are also minor hexagonal-shaped nanoplates [93]. The optimum reaction time of 24 hours has helped in the crystallization.

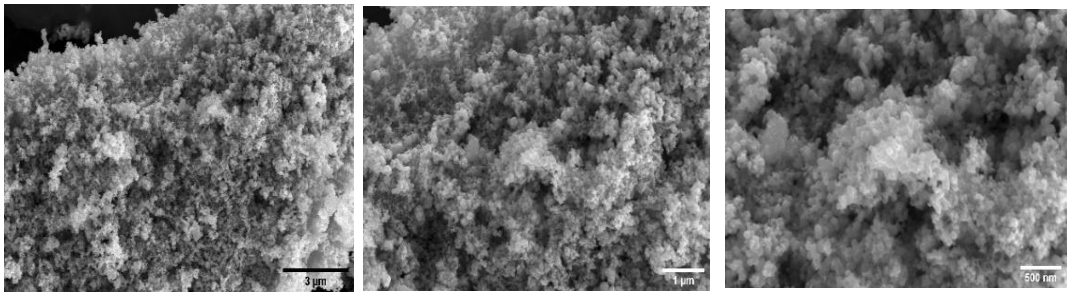

Figure 31: SEM images of the $Cu_{1.8}Se$ synthesized at 180 °C for 24 h.

5.2.2. Copper Selenide- Graphene Nanocomposites

The XRD patterns for the synthesized Tour's GO and Hummer's GO composites are represented in Figure 32. The peaks match with the cubic $Cu_{1.8}Se$ standard (ICDD PDF Card No: 04-003-6777). The same can be inferred from Hummer's GO composites, as shown**.** The synthesized nanopowders are present in the high-temperature β- phase, which is kinetically favored over the low-temperature α- phase [164]. This compound belongs to the class of non-stoichiometric $Cu_{2-x}Se$ with exceptional electrical properties due to high carrier concentration. The diffracted lattice planes are matched and identified in Figure 32**,** with (220) plane having the highest intensity. There are no peaks that show oxides in the sample or pure elements from the precursors. However, the 0.05% Hummer's GO composites show some low-intensity additional peaks due to multiple phases in the sample. Those peaks best match with the standard ICDD card of Cu_3Se_2/ CuSe.

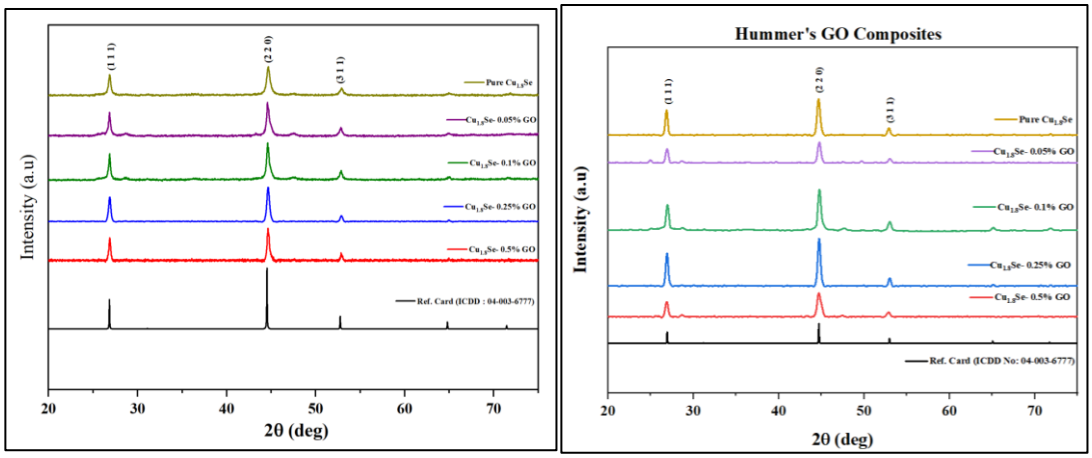

Figure 32: XRD plot of synthesized $Cu_{1.8}Se$- Tour's GO and Hummer's GO composites with standard PDF card (ICDD: 04-003-6777)

The same procedure used for the pure samples was followed to obtain the grain sizes of the graphene composites. Grain size calculated using the Warren Averbach method had the best fit, and the results are summarized in Table 9**.** The Hummer's GO composites showed a comparatively lesser grain size than the Tour's GO composites. The synthesis method for GO is different in the two cases. GO prepared via Hummer's method has a comparatively smaller sheet size than GO prepared by Tour [165]. The linear fits for the composites can be found in Appendix A.1

Table 9: Grain sizes for pure $Cu_{1.8}Se$ and $Cu_{1.8}Se$ Graphene composites obtained using Scherrer, Williamson-Hall, and Warren-Averbach methods

GO Concentration (%)	Grain Size (nm)		
	Scherrer's Method	Williamson-Hall	Warren-Averbach (Best Fit)
0 (Pure)	22	48	42
Tour's GO Composites			
0.05	25	56	48
0.1	28	58	51

0.25	35	43	47
0.5	37	43	48
Hummer's GO Composites			
0.05	26	28	32
0.1	28	23	29
0.25	31	26	32
0.5	23	29	32

XPS confirmed the synthesis of copper selenide-based composites with Cu and Se showing peaks corresponding to copper selenide. The deconvoluted XPS scan of the 0.1% GO composites is shown in Figure 33. As seen in the control sample, surface oxidation is present as indicated by the satellite peaks.

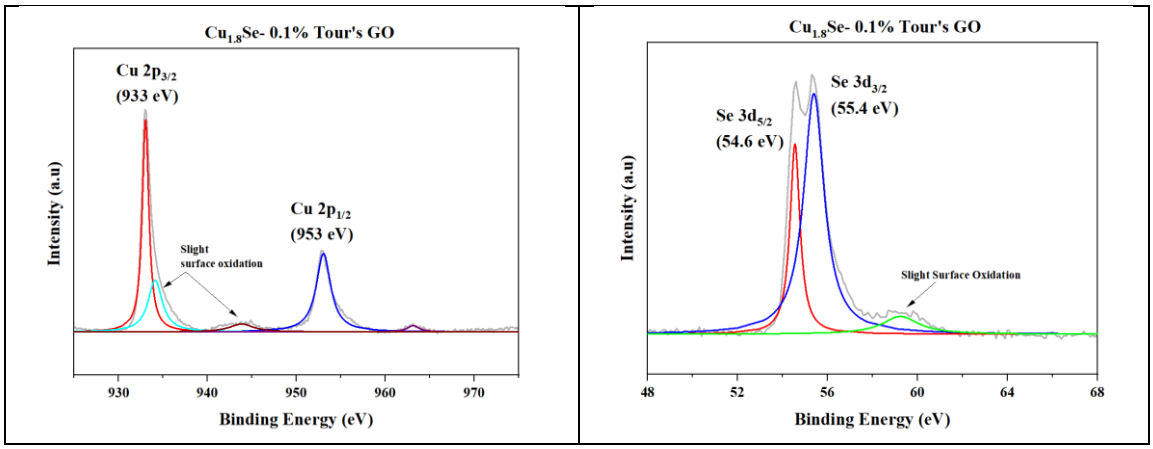

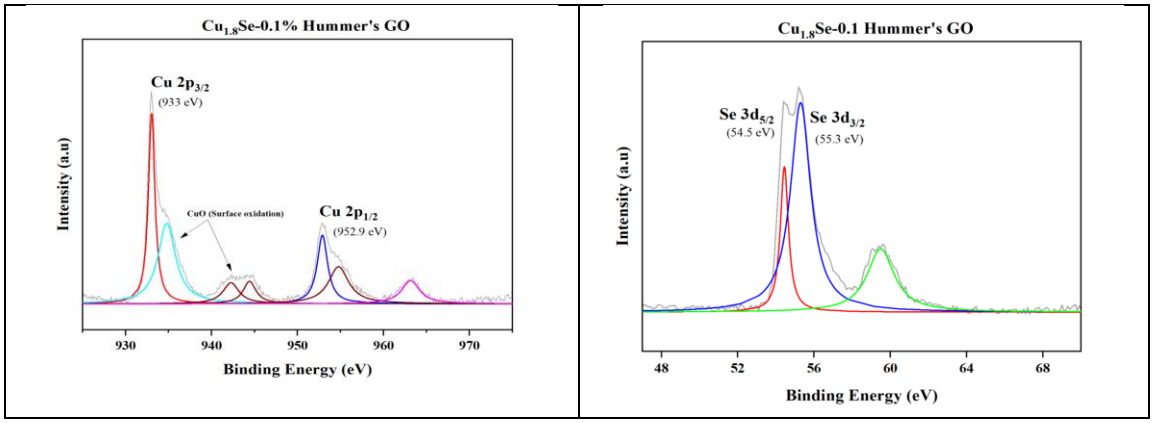

Figure 33: Deconvoluted XPS scans of the 0.1% Tour's and Hummer's GO composites

The Cu and Se content can be quantified from the peak areas of Cu 2p and Se 3d, tabulated in Table 10. In this sample's composition, Selenium has significantly decreased, although the EDS analysis gives a 2/1 Cu and Se atomic ratio. Since XPS is a surface characterization technique, the low Se content shows that the surface primarily consists of oxidized Cu.

Table 10:Quantification of pure $Cu_{1.8}Se$ and $Cu_{1.8}Se$ -Graphene composites from XPS

Graphene (wt%)	**Cu**	**Se**	**O**
0 (Pure)	59	11	30
Tour's GO Composites			
0.05	57	13	30
0.1	55	15	30
0.25	68	6	26
0.5	61	12	27
Hummer's GO Composites			
0.05	49	12	39
0.1	47	11	42
0.25	29	10	61
0.5	47	12	41

Figure 34 shows the SEM images of the 0.1% composites. The embedded carbon inclusions can be seen in the 0.1% Tour's GO composite that spans up to several micrometers. The presence of carbon inclusions strongly reduces the material's thermal conductivity by acting as barriers to phonon propagation at grain boundaries. There is also a high amount of agglomeration seen in the images. The remaining SEM images of the composites can be found in Appendix- A2.

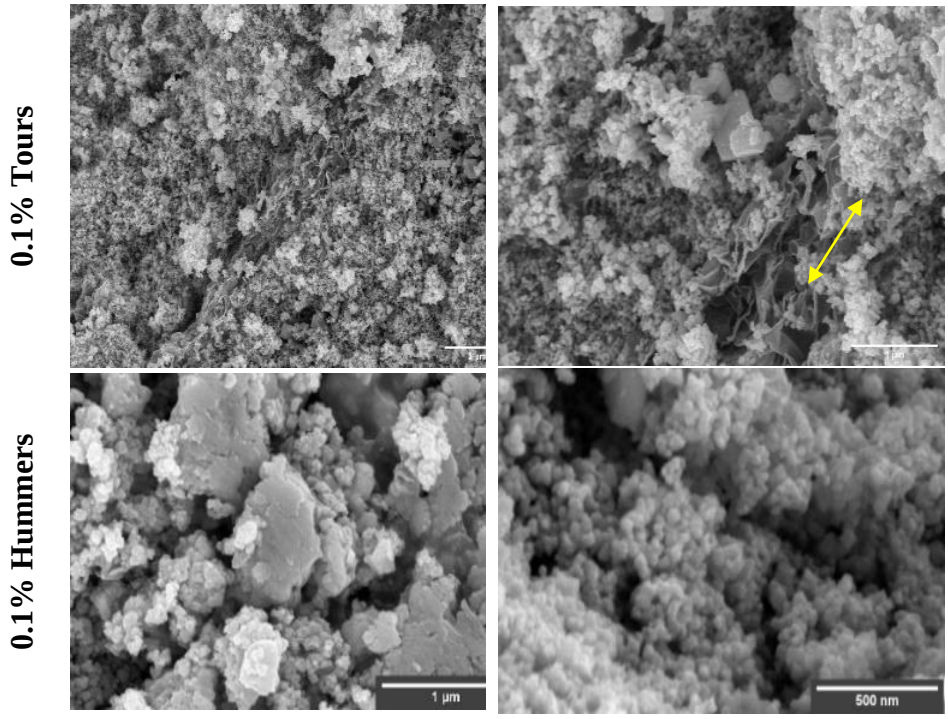

Figure 34: SEM Images of $Cu_{1.8}Se$ and $Cu_{1.8}Se$ – 0.1% GO nanocomposites

Table 11 summarizes the elemental composition results obtained from EDS analysis. A stoichiometric ratio of 2:1 (Cu: Se) with comparatively less oxygen atomic% in the Hummer's GO composites.

Table 11: Elemental composition from EDS analysis

Graphene (wt%)	Cu	Se	O
0 (Pure)	61	31	8
Tour's GO Composites			
0.05	54	25	21
0.1	53	25	22
0.25	64	28	8
0.5	55	28	17
Hummer's GO Composites			
0.05	60	29	11
0.1	48	29	23
0.25	62	27	11
0.5	57	28	15

5.2.3. Thermal Properties

Thermal properties of the as-synthesized nanopowders were analyzed using DSC and TGA using the technique and conditions outline in Section 4.3.2. The analysis was done from 50 °C to a temperature of 400˚C. From the DSC scans, it can be inferred that the sample is relatively stable without any peaks corresponding to melting for the pure, 0.05, and 0.1 composites. An endothermic peak was observed around 150 °C in the 0.25% and 0.5% Tour's GO composite, attributed to the sample's melting of remaining solvents/ salts. The endothermic peak corresponding to the melting point of Se (220 °C) is also absent in all samples. The synthesis's reaction temperature (180 °C) is higher than the phase transformation temperature (127 °C). Therefore, the obtained product is in the high-temperature β-phase, kinetically favored over the low-temperature α-phase. Hence, this phase transformation is absent in all the DSC scans [97]. The Hummer's GO composites also

showed the same trend for the 0.05% and 0.1% GO composites. The 0.25% GO composite has a peak at 100°C, which is due to removing residual moisture in the sample.

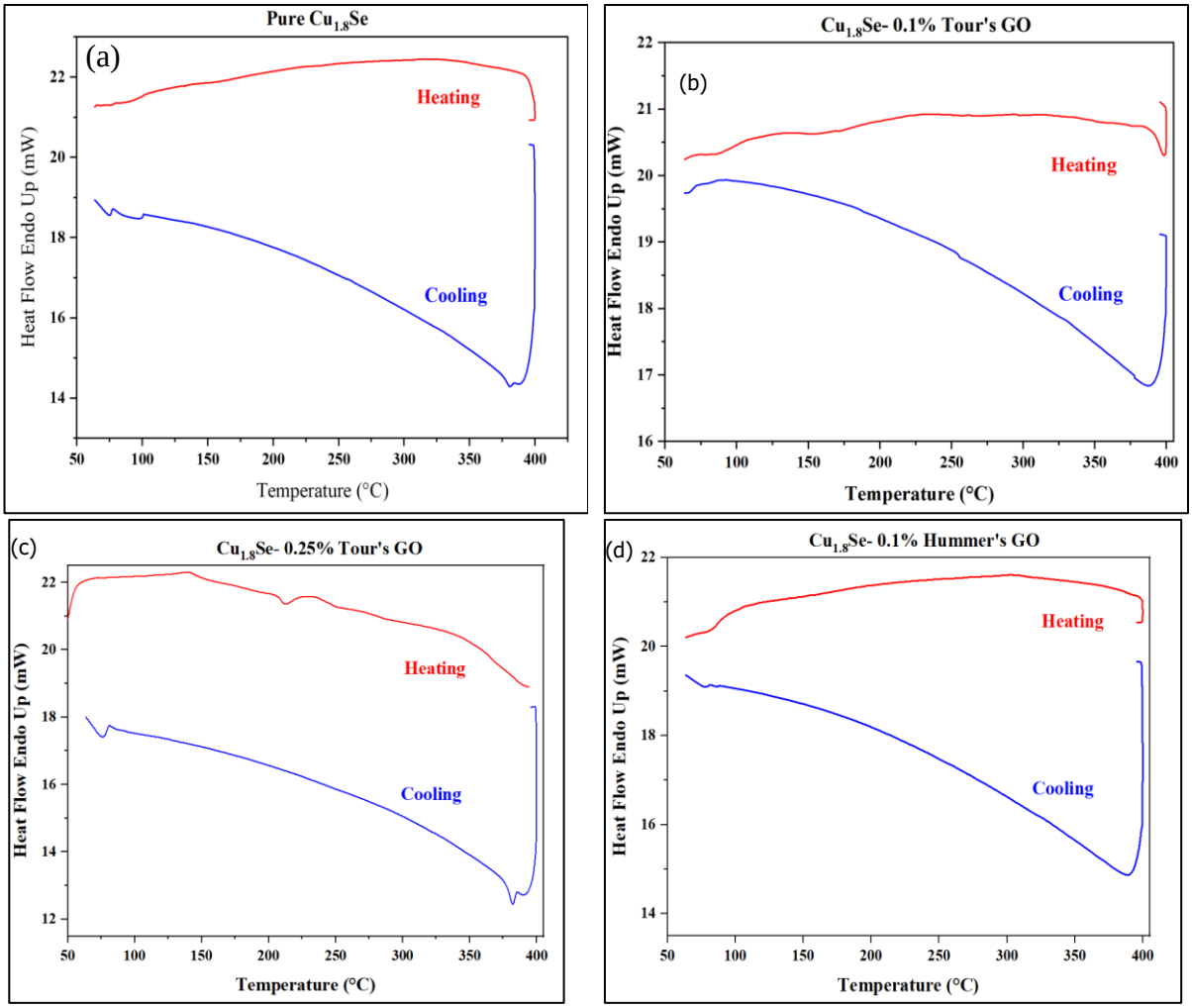

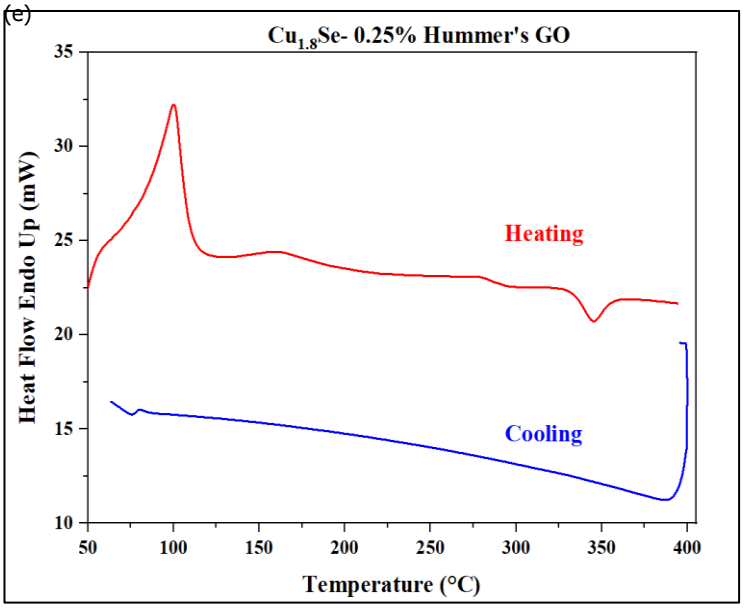

Figure 35: DSC thermograms of (a) Pure $Cu_{1.8}Se$, (b) $Cu_{1.8}Se$- 0.1% Tour's GO, (c) $Cu1_{.8}Se$- 0.25% Tour's GO (d) $Cu_{1.8}Se$- 0.1% Hummer's GO and (e) $Cu_{1.8}Se$- 0.25 % Hummer's GO performed from ambient to 400 ˚C under N_2 atmosphere.

The thermal stability of the pure and graphene nanocomposites was evaluated using TGA. The materials showed good stability up to 300 °C. A decrease in mass starts at 300 ˚C, but the simultaneous DSC signal does not show any thermal transformations at this temperature. The weight loss begins around 350 °C for all samples except 0.05% and 0.25% of Tour's GO composites depicted in Figure 36-a. They both show an abnormal weight gain which is not reflected in other samples. The pure sample had a weight loss of 10%, and no clear trend was observed for the graphene nanocomposites. The 0.1% Tour's GO composite had a lesser weight loss than the control sample.

For the Hummer's GO composites, 0.1% GO showed the best stability with only 7-8% weight loss. Again, the absence of a clear trend denies a conclusive statement on thermal stability.

The sublimation of Se and the electromigration of Cu at higher temperatures could be attributed to the weight loss[166]. Thus, the degradation must be rectified for the material to be helpful in practical applications.

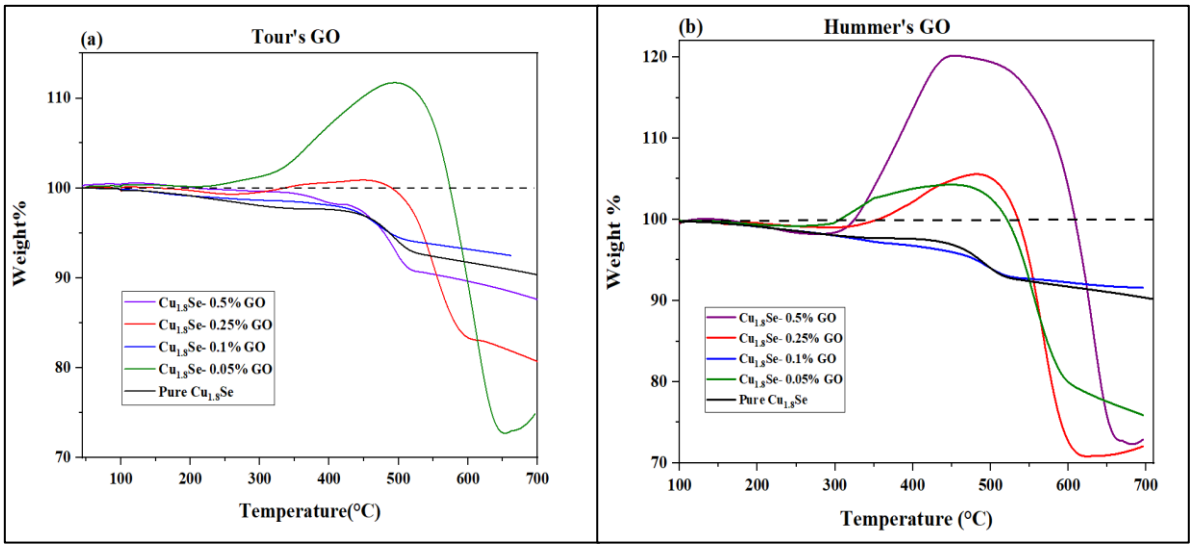

Figure 36:TGA for pure $Cu_{1.8}Se$ and GO composites heated at 20 ˚C/min under N_2 atmosphere, performed from ambient temperature to 700 ˚C

The thermal stability of the samples was improved by annealing the as-synthesized powders at 600 °C under inert conditions. The steps followed characterization, the results of the thermal properties are elaborated in Section 5.2.6.

5.2.4. Mechanical Properties

The hardness of pure copper selenide was measured and was found to be the lowest with a cross-plane hardness of 0.48 GPa, which is higher than the reported values [167, 168]. Figure 37 reveals that the hardness of the material increases with the addition of graphene. Although, the 0.05% GO loading shows better hardness than the 0.1% GO sample. There is an 83%

increase in hardness with the 0.05% Hummer's GO, revealing the excellent reinforcing effect of graphene and suggesting good dispersion in the $Cu_{1.8}Se$ matrix.

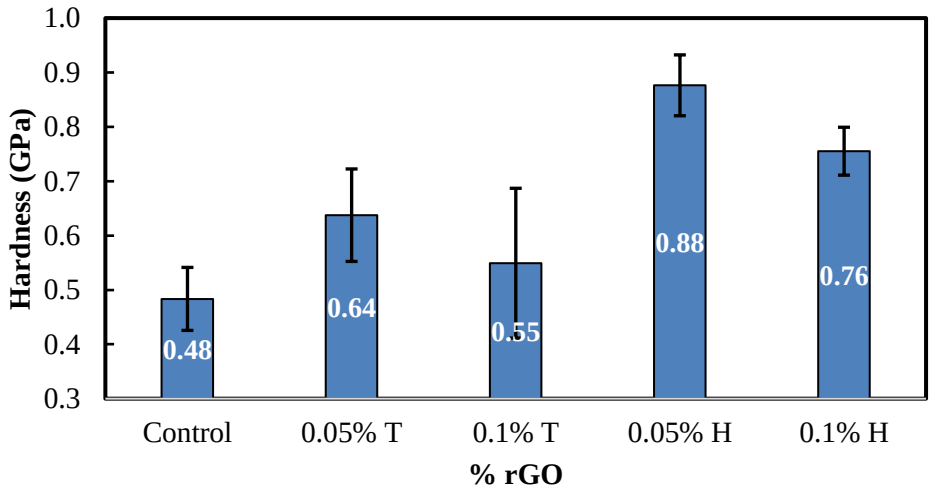

Figure 37: Effect of graphene loading on the hardness of $Cu_{1.8}Se$((H= Hummer's GO, T= Tour's GO)

5.2.5. Thermoelectric Properties

Electrical transport properties like the Seebeck coefficient (S) and electrical conductivity (σ) were measured for the pristine and graphene composites. The presence of a melting peak in the DSC scans of both the 0.25% and 0.5% Tours and Hummers GO composite prevented the hot-pressing and their corresponding testing. Melting of the sample might result in damage to the die/ sensors used in the respective equipment. Hence, only the new, 0.05%, and 0.1% composites were pressed and tested. Further heat treatment and analysis must be carried on the remaining composites to stabilize the material thermally.

Figure 38 shows the electrical conductivity (σ), Seebeck coefficient (S), and Power Factor trends for the pure and GO composites. The temperature-dependent electrical conductivity is shown in Fig. 34a. All the GO nanocomposites have higher electrical conductivity than the pristine sample. The nanocomposites show high electrical conductivity over the entire temperature range and drop as the temperature increases, typical of a semiconductor [169]. The electrical conductivity is comparable with state-of-the-art thermoelectric materials [57, 85, 170]. The non-stoichiometry of the compound due to copper deficiency leads to an increase in Cu vacancies. These vacancies generate more carrier concentration due to holes, thereby enhancing electrical conductivity [57]. At higher temperatures, the mobility of the charge carriers is significantly decreased, leading to a reduction in electrical conductivity. The increase in the conductivity over the temperature range for the GO composites seems to match the trend reported by Li et al. [141]. The presence of graphene inclusions generates more Cu vacancies, leading to increased electrical conductivity[141].

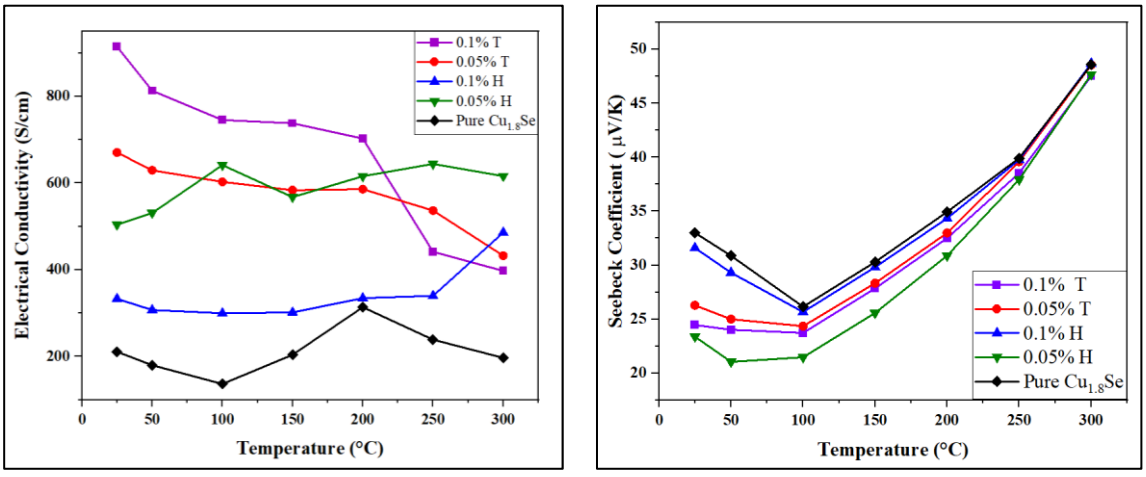

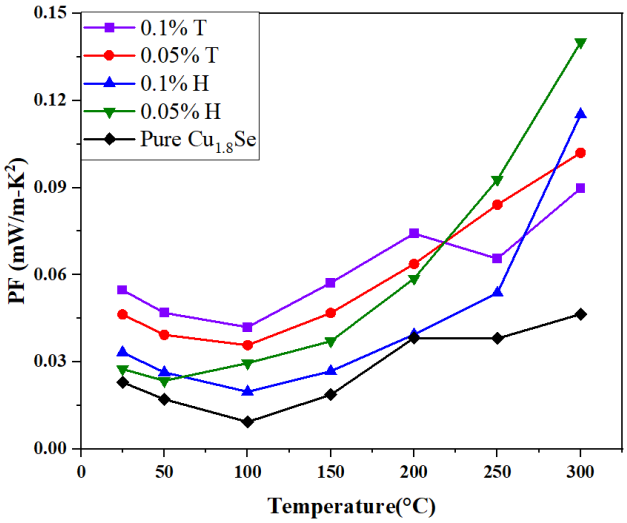

Figure 38: Temperature dependence of (a) Electrical conductivity, (b) Seebeck coefficient, and (c) Power factor for $Cu_{1.8}Se$ and its GO composites (H= Hummer's GO, T= Tour's GO)

Fig 34.b shows the Seebeck coefficient (S) temperature dependence, which is a crucial property in evaluating the TE performance of a material. All the samples show a positive Seebeck coefficient indicating holes are the primary carriers with p-type conduction [97]. All the samples (pure and composites) exhibit nearly the same trend where the Seebeck coefficient increases with increasing temperature. At 300 °C, all the samples exhibit the highest S of 49 µV/K, which is lower than the literature [140, 170]. As explained in Section 1.5.1, Seebeck coefficient (S) and carrier concentration are inversely related as per the relation [24]:

$$S = \frac{8\pi^2 k_B^2}{3eh^2} m^* T \left(\frac{\pi}{3n}\right)^{2/3} \quad (5.1)$$

where k_B is the Boltzmann's constant, h is the Planck constant, m^* the effective mass of the carrier, and e is the charge of an electron. Hence, the higher carrier concentration in the non-stoichiometric copper selenide could be the cause the low Seebeck coefficient.

The power factor ($PF=S^2\sigma$) for the pure and composites are shown in Fig. 34c. The control has the lowest PF over the entire temperature range. All the samples show an increasing trend with temperature. The Hummer's GO composite has a better PF than the Tour's GO composite with a maximum value of 0.14 mW/m-K^2 for the 0.05% Hummer's GO at 300 °C. That is a 200% increase over the control sample. The 0.05% GO concentration seems to have a higher PF than the 0.1% at 300 °C for both the composites. The 0.1% Tours GO composite has a higher PF over 0.05% GO from room temperature to 200 °C but drops suddenly to start increasing again. The presence of graphene inclusions could have reduced the thermal conductivity reported by others [141, 169]. Hence, graphene has dramatically increased the power factor by increasing both the Seebeck coefficient and electrical conductivity. Due to the thermal instability of the compound at higher temperatures, the measurements could not be run above 300 °C. Therefore, improvements in the synthesis method or treatment of the samples to produce a near stoichiometric compound with optimum carrier concentration should be carried out.

5.2.6. Thermal Treatment

As discussed in the previous sections, the superionic behavior of Cu ions at high temperatures leads to electromigration and thermal instability [104]. In Section 5.2.3, the poor thermal stability of some of the composites leads to the inability to press and test the sample for TE properties. Hence, the samples were selected for annealing to stabilize the material thermally. Annealing can modify the structure, composition, electrical and thermal properties. The

0.25% Hummer's GO was taken as the pilot sample to be annealed due to the melting peaks in the DSC scans. The annealing was carried out in a tubular furnace for 10 hours at 600 °C under high purity Argon.

Figure 39 shows the XRD patterns of the annealed 0.25% Hummer's GO composite. The well-defined peaks suggest that the annealed nanopowders are crystalline. The peaks match well with the standard PDF card (ICDD Card: 00-027-1131) of alpha-Cu_2Se. The peak at $2\theta=13°$ is a characteristic of the low-temperature α-phase. Hence, the previous $Cu_{2-x}Se$ loses Se and becomes stoichiometric Cu_2Se in the monoclinic phase belonging to space group P2/m(10).

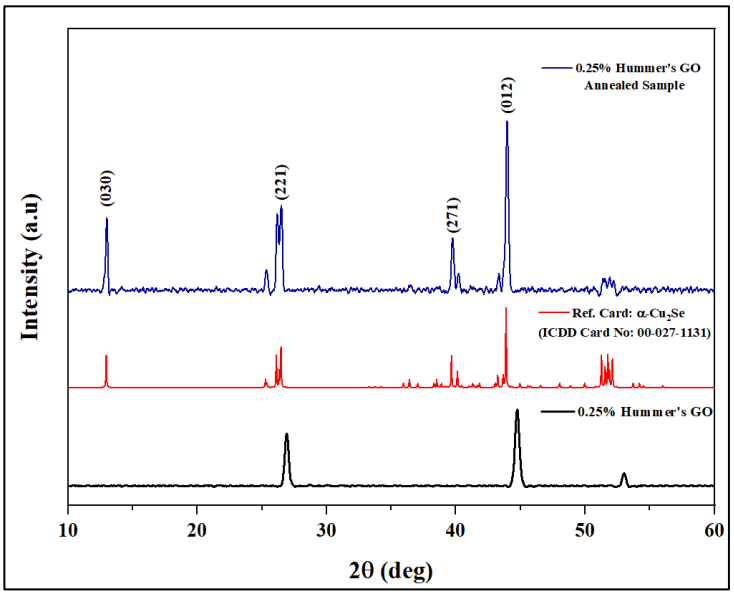

Figure 39: XRD plot of synthesized and annealed $Cu_{1.8}Se$- 0.25% Hummer's GO with standard PDF card (ICDD: 00-027-1131)

The interplanar distance of the (012) plane was 0.21 nm, obtained using Bragg's Law. The grain size was calculated using the Williamson-Hall method, and the same procedure as

detailed in Section 4.3.1 was followed. The average grain size for the crystals was 92 nm using Warren- Averbach method, which gave the best fit. The grain size has increased three times over the as-synthesized composite due to grain growth at high temperatures. The linear fits of the XRD data are provided in Figure 40. These fits yielded a strain of 11%.

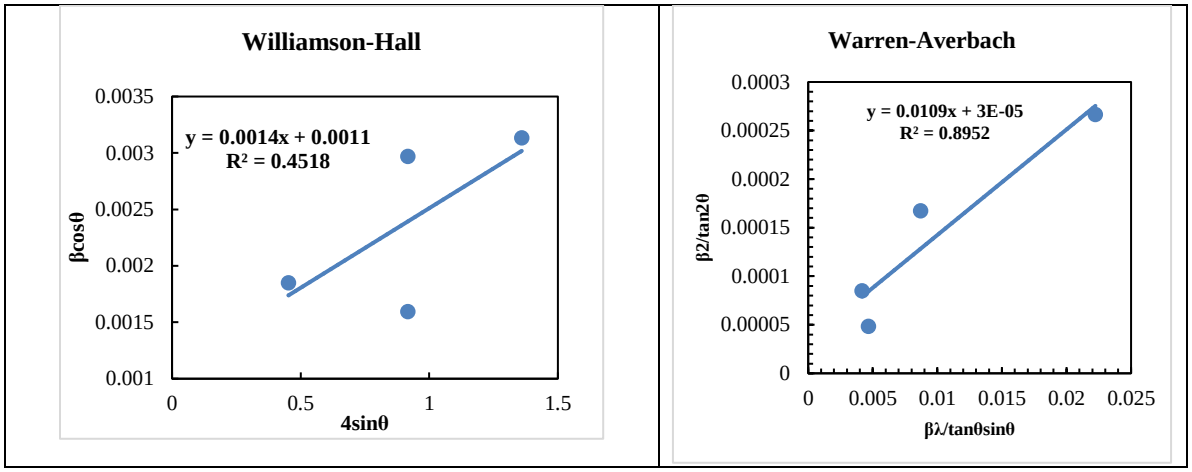

Figure 40: Williamson Hall and Warren-Averbach linear fit for the annealed 0.25% Hummer's GO composite

Hence, annealing has changed the non-stoichiometric phase to the stoichiometric phase, which would yield better TE properties.

The thermal stability of the compound was studied using TGA and DSC. The analysis was done from 50 °C to a temperature of 400˚C under nitrogen. Figure 41 shows the DSC and TGA scans of the annealed sample. As highlighted in the DSC scan, a reversible phase transition occurs at around 130-135 °C as reported in various literature [68, 171]. This confirms that the annealed sample is in the low-temperature α- phase and undergoes a reversible phase transition to high-temperature β-phase. Moreover, the TGA scan shows that the stability of the material has greatly improved with minimal weight loss,

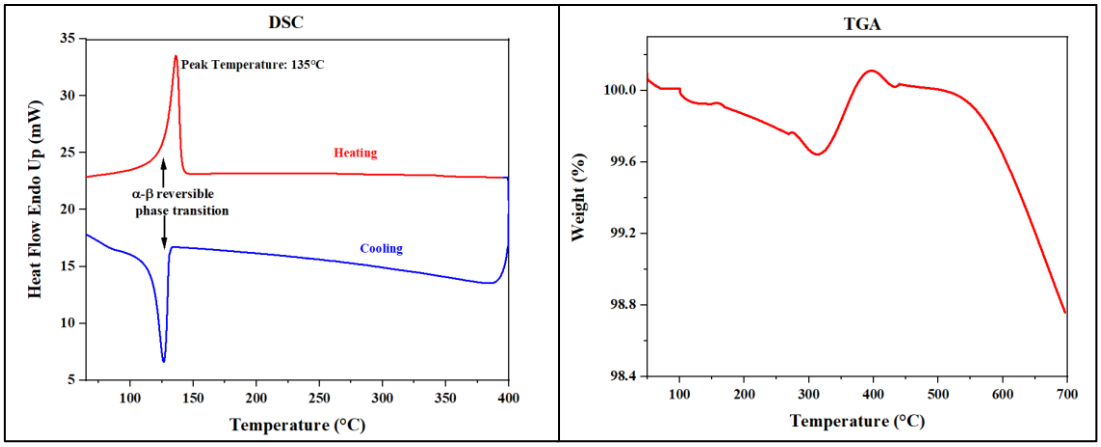

Figure 41: DSC and TGA scans of the annealed GO composite

The preliminary results confirmed the excellent thermal stability of the sample. Hence, the material was forwarded to hot pressing and subsequent TE property measurements. Figure 42 shows the electrical conductivity (σ), Seebeck coefficient (S), and Power Factor (PF) trend for the annealed sample. The sample shows high electrical conductivity that decreases with increasing temperature. The absence of Cu vacancies leads to minimal dislocations and point defects, thereby reducing the scattering factors responsible for low carrier mobility. The sudden increase in the electrical conductivity around 130-140 °C is due to the phase transition as discussed earlier. Fig. 38b shows the temperature dependence of the Seebeck coefficient. The Seebeck coefficient has substantially increased after annealing reaching 86 μV/K. The anomaly drop in the Seebeck coefficient at 140°C is due to the α-β transition.

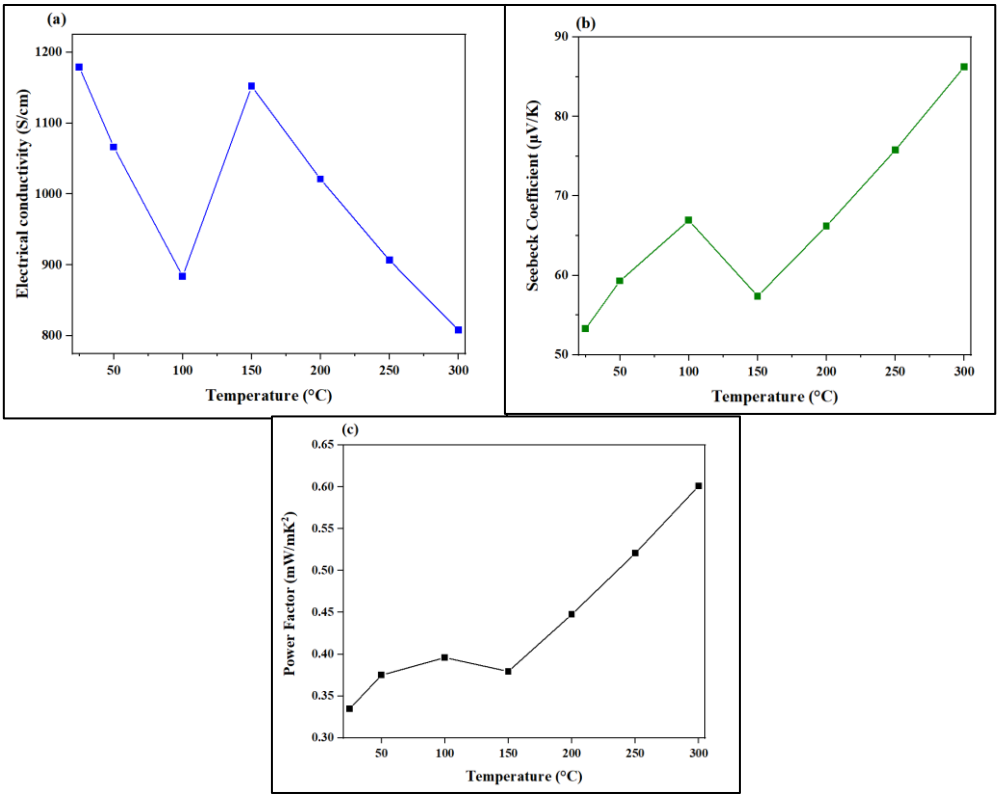

Figure 42: Temperature dependence of (a) Electrical conductivity, (b) Seebeck coefficient, and (c) Power factor for 0.25% Hummer's GO annealed sample.

Based on the electrical conductivity and Seebeck coefficient, the power factor is calculated. As shown in Fig 38.c, the power factor shows an increasing trend with temperature. A maximum value of 0.6 mW/mK^2 is achieved at 300 °C, four times higher than the power factor value obtained for the 0.05% Hummer's GO composite (PF= 0.14 mW/mK^2). Hence, annealing has improved the TE properties of the sample remarkedly, making it a potential method in the synthesis process.

The annealing process was then applied to the control sample using the same conditions to test the effect of pristine copper selenide. The removal of Cu vacancies has improved the Seebeck coefficient due to less carrier concentration. Figure 43 shows the electrical conductivity, Seebeck coefficient, and Power factor for the control and the annealed sample.

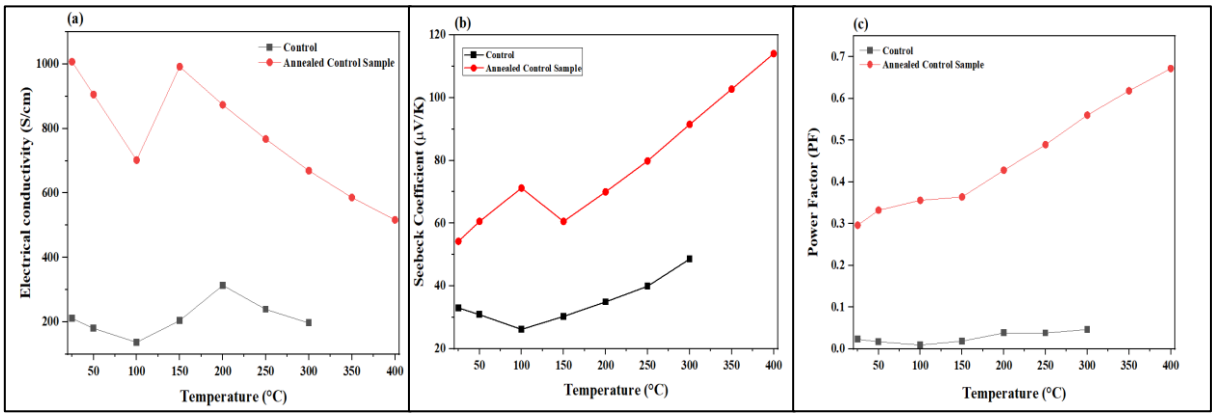

Figure 43: Temperature dependence of (a) Electrical conductivity, (b) Seebeck coefficient, and (c) Power factor for the control and annealed control sample.

The effect of annealing is evident on all the properties, with a significant increase in the Seebeck coefficient. Due to excellent thermal stability, the measurements were done up to 400 °C. The Seebeck coefficient of the non-annealed sample at 300 °C is 49 μV/K, while that of the annealed sample at the same temperature is 91 μV/K. Meanwhile, the power factor has increased from 0.04 mW/mK^2 to 0.56 mW/mK^2. The maximum power factor is 0.67 mW/mK^2 at 400 °C, comparable to those reported in the literature [83, 91].

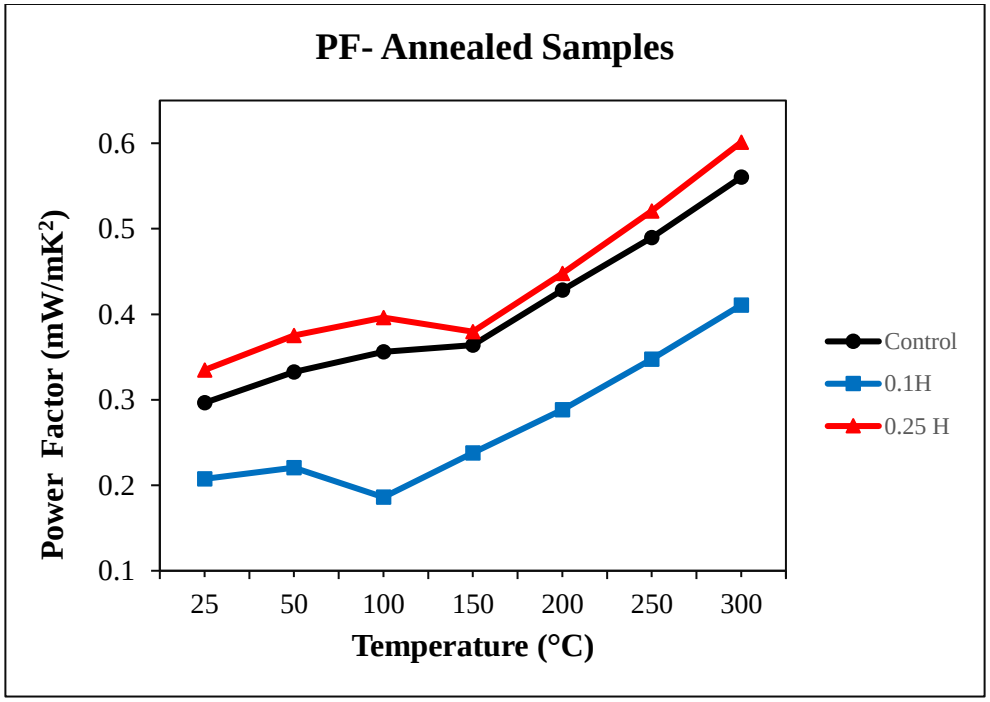

Figure 44: Comparision of annealed composites with the control

Figure 44 shows a comparision of annealing on the composites and the control sample. The annealing was carried out under the same conditions as before with no changes. As shown, the 0.25 Hummer's GO composite has the highest PF trend over the temperature measured. A maximum value of 0.60 mW/mK^2 is obtained at 300 °C higher than the control. Both the samples show a small drop due to phase transition around 130-140 °C. Hence, the addition of graphene has improved the TE properties of the material post annealing.. Unfortunately, the 0.1% Hummer's GO composite shows an anomaly trend with PF values lower than the control. However, the PF values increases with temperature and are higher than the same 0.1% Hummer's GO composite before annealing (0.11 mW/mK^2 at 300 °C). Larger grains

with fewer boundaries improved the carrier mobility of the electrons. Hence, the annealing should be carried out on all samples to enhance the TE properties.

6. CONCLUSION AND FUTURE WORK

In this research, pure copper selenide and their composites with GO (Tours and Hummers GO) were synthesized using a scalable hydrothermal method. Copper selenide was prepared from copper sulfate and selenium dioxide as precursors and hydrazine as the reducing agent. XRD and XPS analysis confirmed the synthesis of cubic copper selenide. The SEM analysis of the as-synthesized nanopowders shows spherical morphology with agglomeration and good dispersion of GO in the copper selenide matrix. The addition of GO did not have any effect on the structure and morphology of the sample. However, the Hummer's GO composites (~31 nm) had a comparatively lesser grain size than the Tour's GO composites (~49 nm). The TGA and DSC thermograms of the materials showed that their thermal stability requires improvement, as a high weight loss was observed, along with melting in the DSC analysis. The samples that did not show a melting peak were hot-pressed and analyzed for TE and mechanical properties. The hardness measurements carried out for control and composites gave results agreeable with the literature. Moreover, graphene has enhanced the mechanical properties, as demonstrated by an 83% increase in hardness to the control sample.

The TE properties were enhanced with GO, a 200% increase in the PF of 0.05% Hummer's GO over the control sample, with a maximum power factor of 0.14 mW/mK^2 . However, the material's poor thermal stability and non-stoichiometric nature yielded poor TE properties compared with the literature and restricted the hot-pressing and testing at higher temperatures. Hence, selected samples were chosen for thermal annealing treatment.

The thermal annealing of the 0.25% Hummer's GO at 600°C under inert conditions drastically improved the thermal stability. The XRD analysis confirmed low temperature α-phase monoclinic stoichiometric Cu_2Se with a large grain size of 92 nm. The TGA for the composite showed a slight mass loss (~1%). The DSC analysis confirmed the reversible α-β phase transition with no peaks corresponding to melting. The TE properties of the control sample have also been enhanced due to annealing. PF value of 0.6 mW/mK^2 is achieved at 300 °C, four times higher than the power factor value obtained for the 0.05% Hummer's GO composite at the same temperature (PF= 0.14 mW/mK^2). With satisfactory preliminary results, the annealing was carried on the control sample to have a clear understanding. As predicted, the thermal treatment has drastically improved the electrical conductivity, Seebeck coefficient, and power factor. The power factor has increased from 0.04 mW/mK^2 to 0.56 mW/mK^2 at 300 °C for the control, comparable with the literature. Thus, the effect of annealing has been studied on the structure and TE properties of the selected samples.

Regarding future work, the amount of the reducing agent used must be tuned to ensure the synthesis of stoichiometric Cu_2Se. The thermal treatment must be done on all the composites so that the TE performance testing can be performed, and the impact of adding graphene to the pure materials can be studied. The effect of different annealing temperatures, duration, and hot-pressing temperature must be examined to find the optimum condition for the best TE performance.

REFERENCES

[1] Z. Salameh, "Chapter 1 - Factors Promoting Renewable Energy Applications," in *Renewable Energy System Design*, Z. Salameh Ed. Boston: Academic Press, 2014, pp. 1-32.

[2] L. Wang *et al.*, "Exceptional thermoelectric properties of flexible organic–inorganic hybrids with monodispersed and periodic nanophase," *Nature Communications,* vol. 9, no. 1, p. 3817, 2018/09/19 2018, doi: 10.1038/s41467-018-06251-9.

[3] D. Beretta *et al.*, "Thermoelectrics: From history, a window to the future," *Materials Science and Engineering: R: Reports,* vol. 138, p. 100501, 2019/10/01/ 2019, doi: https://doi.org/10.1016/j.mser.2018.09.001.

[4] J.-F. Li, W.-S. Liu, L.-D. Zhao, and M. Zhou, "High-performance nanostructured thermoelectric materials," *NPG Asia Materials,* vol. 2, no. 4, pp. 152-158, 2010/10/01 2010, doi: 10.1038/asiamat.2010.138.

[5] L. E. Bell, "Cooling, Heating, Generating Power, and Recovering Waste Heat with Thermoelectric Systems," *Science*, vol. 321, no. 5895, p. 1457, 2008, doi: 10.1126/science.1158899.

[6] J.-c. Zheng, "Recent advances on thermoelectric materials," *Frontiers of Physics in China,* vol. 3, no. 3, pp. 269-279, 2008/09/01 2008, doi: 10.1007/s11467-008-0028-9.

[7] J. R. Szczech, J. M. Higgins, and S. Jin, "Enhancement of the thermoelectric properties in nanoscale and nanostructured materials," *Journal of Materials Chemistry,* 10.1039/C0JM02755C vol. 21, no. 12, pp. 4037-4055, 2011, doi: 10.1039/C0JM02755C.

[8] T. J. Seebeck, "Ueber die magnetische Polarisation der Metalle und Erze durch Temperaturdifferenz," *Annalen der Physik,* vol. 82, no. 3, pp. 253-286, 1826/01/01 1826, doi: 10.1002/andp.18260820302.

[9] J. C. A. Peltier, *Nouvelles expériences sur la caloricité des courans électriques*. 1834.

[10] L. Rayleigh, "XLIII. On the thermodynamic efficiency of the thermopile," *The London, Edinburgh, and Dublin Philosophical Magazine and Journal of Science,* vol. 20, no. 125, pp. 361-363, 1885/10/01 1885, doi: 10.1080/14786448508627771.

[11] A. F. Ioffe, L. Stil'Bans, E. Iordanishvili, T. Stavitskaya, A. Gelbtuch, and G. Vineyard, "Semiconductor thermoelements and thermoelectric cooling," *PhT,* vol. 12, no. 5, p. 42, 1959.

[12] L. D. Hicks and M. S. Dresselhaus, "Effect of quantum-well structures on the thermoelectric figure of merit," *Physical Review B,* vol. 47, no. 19, pp. 12727-12731, 05/15/ 1993, doi: 10.1103/PhysRevB.47.12727.

[13] L. D. Hicks and M. S. Dresselhaus, "Thermoelectric figure of merit of a one-dimensional conductor," *Physical Review B,* vol. 47, no. 24, pp. 16631-16634, 06/15/ 1993, doi: 10.1103/PhysRevB.47.16631.

[14] G. S. Nolas, J. Sharp, and J. Goldsmid, *Thermoelectrics: basic principles and new materials developments*. Springer Science & Business Media, 2013.

[15] Y. Lan, A. J. Minnich, G. Chen, and Z. Ren, "Enhancement of Thermoelectric Figure-of-Merit by a Bulk Nanostructuring Approach," *Advanced Functional Materials,* vol. 20, no. 3, pp. 357-376, 2010/02/08 2010, doi: 10.1002/adfm.200901512.

[16] X. Zhang and L.-D. Zhao, "Thermoelectric materials: Energy conversion between heat and electricity," *Journal of Materiomics,* vol. 1, no. 2, pp. 92-105, 2015/06/01/ 2015, doi: https://doi.org/10.1016/j.jmat.2015.01.001.

[17] D. M. Rowe, *Thermoelectrics handbook: macro to nano*. CRC press, 2018.

[18] M.-J. Huang, R.-H. Yen, and A.-B. Wang, "The influence of the Thomson effect on the performance of a thermoelectric cooler," *International Journal of Heat and Mass Transfer,* vol. 48, no. 2, pp. 413-418, 2005/01/01/ 2005, doi: https://doi.org/10.1016/j.ijheatmasstransfer.2004.05.040.

[19] A. Majumdar, "Thermoelectricity in Semiconductor Nanostructures," *Science*, vol. 303, no. 5659, pp. 777-778, 2004. [Online]. Available: www.jstor.org/stable/3836223 https://science.sciencemag.org/content/303/5659/777.long.

[20] J. He and T. M. Tritt, "Advances in thermoelectric materials research: Looking back and moving forward," *Science*, vol. 357, no. 6358, p. eaak9997, 2017, doi: 10.1126/science.aak9997.

[21] P. Brinks and M. Huijben, "14 - Thermoelectric oxides," in *Epitaxial Growth of Complex Metal Oxides*, G. Koster, M. Huijben, and G. Rijnders Eds.: Woodhead Publishing, 2015, pp. 397-441.

[22] M. Telkes, "The Efficiency of Thermoelectric Generators. I," *Journal of Applied Physics*, vol. 18, no. 12, pp. 1116-1127, 1947/12/01 1947, doi: 10.1063/1.1697593.

[23] M. V. Vedernikov and E. K. Iordanishvili, "A.F. Ioffe and origin of modern semiconductor thermoelectric energy conversion," in *Seventeenth International Conference on Thermoelectrics. Proceedings ICT98 (Cat. No.98TH8365)*, 28-28 May 1998 1998, pp. 37-42, doi: 10.1109/ICT.1998.740313.

[24] H. Alam and S. Ramakrishna, "A review on the enhancement of figure of merit from bulk to nano-thermoelectric materials," *Nano Energy*, vol. 2, no. 2, pp. 190-212, 2013/03/01/ 2013, doi: https://doi.org/10.1016/j.nanoen.2012.10.005.

[25] S. M. Pourkiaei *et al.*, "Thermoelectric cooler and thermoelectric generator devices: A review of present and potential applications, modeling and materials," *Energy*, vol. 186, p. 115849, 2019.

[26] X. Zhang and L. D. Zhao, "Thermoelectric materials: Energy conversion between heat and electricity," *Journal of Materiomics*, vol. 1, no. 2, pp. 92-105, 2015, doi: 10.1016/j.jmat.2015.01.001.

[27] J. He and T. M. Tritt, "Advances in thermoelectric materials research: Looking back and moving forward," *Science*, vol. 357, no. 6358, Sep 29 2017, doi: 10.1126/science.aak9997.

[28] C. Han, Z. Li, and S. Dou, "Recent progress in thermoelectric materials," *Chinese science bulletin*, vol. 59, no. 18, pp. 2073-2091, 2014.

[29] L. Yang, Z.-G. Chen, M. S. Dargusch, and J. Zou, "High Performance Thermoelectric Materials: Progress and Their Applications," *Advanced Energy Materials*, vol. 8, no. 6, p. 1701797, 2018/02/01 2018, doi: 10.1002/aenm.201701797.

[30] W. Liu, X. Yan, G. Chen, and Z. Ren, "Recent advances in thermoelectric nanocomposites," *Nano Energy*, vol. 1, no. 1, pp. 42-56, 2012/01/01/ 2012, doi: https://doi.org/10.1016/j.nanoen.2011.10.001.

[31] P. Vaqueiro and A. V. Powell, "Recent developments in nanostructured materials for high-performance thermoelectrics," *Journal of Materials Chemistry*,

10.1039/C0JM01193B vol. 20, no. 43, pp. 9577-9584, 2010, doi: 10.1039/C0JM01193B.

[32] G. J. Snyder and E. S. Toberer, "Complex thermoelectric materials," *Materials for sustainable energy: a collection of peer-reviewed research and review articles from Nature Publishing Group*, pp. 101-110, 2011.

[33] P. Pichanusakorn and P. Bandaru, "Nanostructured thermoelectrics," *Materials Science and Engineering: R: Reports*, vol. 67, no. 2, pp. 19-63, 2010/01/29/ 2010, doi: https://doi.org/10.1016/j.mser.2009.10.001.

[34] Z.-G. Chen, G. Han, L. Yang, L. Cheng, and J. Zou, "Nanostructured thermoelectric materials: Current research and future challenge," *Progress in Natural Science: Materials International*, vol. 22, no. 6, pp. 535-549, 2012/12/01/ 2012, doi: https://doi.org/10.1016/j.pnsc.2012.11.011.

[35] L. D. Hicks, T. C. Harman, X. Sun, and M. S. Dresselhaus, "Experimental study of the effect of quantum-well structures on the thermoelectric figure of merit," *Physical Review B*, vol. 53, no. 16, pp. R10493-R10496, 04/15/ 1996, doi: 10.1103/PhysRevB.53.R10493.

[36] V. Sandomirsky, A. V. Butenko, R. Levin, and Y. Schlesinger, "Electric-field-effect thermoelectrics," vol. 90, no. 5, p. 2370, 2001, doi: 10.1063/1.1389074.

[37] X. Zhou *et al.*, "Routes for high-performance thermoelectric materials," *Materials Today*, vol. 21, no. 9, pp. 974-988, 2018/11/01/ 2018, doi: https://doi.org/10.1016/j.mattod.2018.03.039.

[38] C. J. Vineis, A. Shakouri, A. Majumdar, and M. G. Kanatzidis, "Nanostructured Thermoelectrics: Big Efficiency Gains from Small Features," *Advanced Materials*, vol. 22, no. 36, pp. 3970-3980, 2010/09/22 2010, doi: 10.1002/adma.201000839.

[39] G. J. Snyder and E. S. Toberer, "Complex thermoelectric materials," *Nature Materials*, vol. 7, no. 2, pp. 105-114, 2008/02/01 2008, doi: 10.1038/nmat2090.

[40] E. Skrabek and D. Trimmer, "CRC handbook of thermoelectrics," *CRC, Boca Raton, FL*, p. 267, 1995.

[41] J. Tang *et al.*, "Maximization of transporting bands for high-performance SnTe alloy thermoelectrics," *Materials Today Physics*, vol. 9, p. 100091, 2019/06/01/ 2019, doi: https://doi.org/10.1016/j.mtphys.2019.03.005.

[42] L.-D. Zhao *et al.*, "Ultrahigh power factor and thermoelectric performance in hole-doped single-crystal SnSe," *Science*, vol. 351, no. 6269, p. 141, 2016, doi: 10.1126/science.aad3749.

[43] J. P. Heremans *et al.*, "Enhancement of Thermoelectric Efficiency in PbTe by Distortion of the Electronic Density of States," *Science*, vol. 321, no. 5888, p. 554, 2008, doi: 10.1126/science.1159725.

[44] M. S. Dresselhaus *et al.*, "New Directions for Low-Dimensional Thermoelectric Materials," *Advanced Materials,* vol. 19, no. 8, pp. 1043-1053, 2007/04/20 2007, doi: 10.1002/adma.200600527.

[45] Q. Li, Z. Lin, and J. Zhou, "Thermoelectric Materials with Potential High Power Factors for Electricity Generation," *Journal of Electronic Materials,* vol. 38, no. 7, pp. 1268-1272, 2009/07/01 2009, doi: 10.1007/s11664-008-0628-8.

[46] M.-S. Jeng, R. Yang, D. Song, and G. Chen, "Modeling the Thermal Conductivity and Phonon Transport in Nanoparticle Composites Using Monte Carlo Simulation," *Journal of Heat Transfer,* vol. 130, no. 4, 2008, doi: 10.1115/1.2818765.

[47] B. Poudel *et al.*, "High-Thermoelectric Performance of Nanostructured Bismuth Antimony Telluride Bulk Alloys," *Science,* vol. 320, no. 5876, p. 634, 2008, doi: 10.1126/science.1156446.

[48] H. L. Ni, X. B. Zhao, T. J. Zhu, X. H. Ji, and J. P. Tu, "Synthesis and thermoelectric properties of Bi2Te3 based nanocomposites," *Journal of Alloys and Compounds,* vol. 397, no. 1, pp. 317-321, 2005/07/19/ 2005, doi: https://doi.org/10.1016/j.jallcom.2005.01.046.

[49] X. W. Wang *et al.*, "Enhanced thermoelectric figure of merit in nanostructured n-type silicon germanium bulk alloy," *Applied Physics Letters,* vol. 93, no. 19, p. 193121, 2008, doi: 10.1063/1.3027060.

[50] A. J. Minnich, M. S. Dresselhaus, Z. F. Ren, and G. Chen, "Bulk nanostructured thermoelectric materials: current research and future prospects," *Energy & Environmental Science,* 10.1039/B822664B vol. 2, no. 5, pp. 466-479, 2009, doi: 10.1039/B822664B.

[51] M. G. Kanatzidis, "Nanostructured Thermoelectrics: The New Paradigm?," *Chemistry of Materials,* vol. 22, no. 3, pp. 648-659, 2010/02/09 2010, doi: 10.1021/cm902195j.

[52] P. Qiu, X. Shi, and L. Chen, "Cu-based thermoelectric materials," vol. 3, ed: Elsevier B.V., 2016, pp. 85-97.

[53] A. C. B. A. C. Phys and undefined, "Memoire Sur L'eIectro-chimie et L'emploi de L'electricite Pour Operer des Combinaisons."

[54] X. Y. Shi, F. Q. Huang, M. L. Liu, and L. D. Chen, "Thermoelectric properties of tetrahedrally bonded wide-gap stannite compounds Cu2ZnSn1−xInxSe4," *Applied Physics Letters,* vol. 94, no. 12, p. 122103, 2009/03/23 2009, doi: 10.1063/1.3103604.

[55] T. Plirdpring *et al.*, "Chalcopyrite CuGaTe2: A High-Efficiency Bulk Thermoelectric Material," *Advanced Materials,* vol. 24, no. 27, pp. 3622-3626, 2012.

[56] R. Liu, L. Xi, H. Liu, X. Shi, W. Zhang, and L. Chen, "Ternary compound CuInTe 2: a promising thermoelectric material with diamond-like structure," *Chemical Communications,* vol. 48, no. 32, pp. 3818-3820, 2012.

[57] H. Liu *et al.*, "Copper ion liquid-like thermoelectrics," *Nature Materials,* vol. 11, no. 5, pp. 422-425, 2012, doi: 10.1038/nmat3273.

[58] H. Liu *et al.*, "Ultrahigh Thermoelectric Performance by Electron and Phonon Critical Scattering in Cu2Se1-xIx," *Advanced Materials,* https://doi.org/10.1002/adma.201302660 vol. 25, no. 45, pp. 6607-6612, 2013/12/01 2013, doi: https://doi.org/10.1002/adma.201302660.

[59] R. P. Andres *et al.*, "Research opportunities on clusters and cluster-assembled materials —A Department of Energy, Council on Materials Science Panel Report," *Journal of Materials Research,* vol. 4, no. 3, pp. 704-736, 1989, doi: 10.1557/JMR.1989.0704.

[60] R. Amatya and R. J. Ram, "Trend for thermoelectric materials and their earth abundance," *Journal of Electronic Materials,* vol. 41, no. 6, pp. 1011-1019, 2012, doi: 10.1007/s11664-011-1839-y.

[61] Y. Gu *et al.*, "Hydrothermal synthesis of hexagonal CuSe nanoflakes with excellent sunlight-driven photocatalytic activity," *CrystEngComm,* vol. 16, no. 39, pp. 9185-9190, 2014, doi: 10.1039/c4ce01470g.

[62] W. S. Chen, J. M. Stewart, and R. A. Mickelsen, "Polycrystalline thin-film Cu2-xSe/CdS solar cell," *Applied Physics Letters,* vol. 46, no. 11, pp. 1095-1097, 1985, doi: 10.1063/1.95773.

[63] C. Naşcu, I. Pop, V. Popescu, E. Indrea, and I. Bratu, "Spray pyrolysis deposition of CuS thin films," *Materials Letters,* vol. 32, no. 2-3, pp. 73-77, 1997, doi: 10.1016/S0167-577X(97)00015-3.

[64] H. Okimura, T. Matsumae, and R. Makabe, "Electrical properties of Cu2−xSe thin films and their application for solar cells," *Thin Solid Films,* vol. 71, no. 1, pp. 53-59, 1980, doi: 10.1016/0040-6090(80)90183-2.

[65] M. A. Korzhuev, "Dufour effect in superionic copper selenide," *Physics of the Solid State,* vol. 40, no. 2, pp. 217-219, 1998, doi: 10.1134/1.1130276.

[66] T.-R. Wei *et al.*, "Copper chalcogenide thermoelectric materials," vol. 62, no. 1, pp. 8-24, 2019, doi: 10.1007/s40843-018-9314-5.

[67] A. L. N. Stevels and F. Jellinek, "Phase transitions in copper chalcogenides: I. The copper-selenium system," *Recueil des Travaux Chimiques des Pays-Bas,* vol. 90, no. 3, pp. 273-283, 1971, doi: 10.1002/recl.19710900307.

[68] V. Glazov, A. Pashinkin, and V. Fedorov, "Phase equilibria in the Cu-Se system," *Inorganic materials,* vol. 36, no. 7, pp. 641-652, 2000.

[69] L. Gulay, M. Daszkiewicz, O. Strok, and A. Pietraszko, "Crystal structure of Cu2Se," *Chemistry of metals and alloys,* no. 4,№ 3-4, pp. 200-205, 2011.

[70] H. Robert Donald and R. Maclaren Murray, "Canadian Journal Journal The crystal structures of Cu1Se, Cu,Se,, a- and yCuSe, CuSe,, and CuSe,II." [Online]. Available: www.nrcresearchpress.com

[71] V. M. Glazov, A. S. Pashinkin, and V. A. Fedorov, "Phase equilibria in the Cu-Se system," *Inorganic Materials*, vol. 36, no. 7, pp. 641-652, 2000, doi: 10.1007/bf02758413.

[72] G. P. Sorokin, Y. M. Papshev, P. T. O. S. P. S. State, u. Ussr, and undefined, "Photoconductivity of Cu2S Cu2Se and Cu2Te."

[73] A. M. Hermann and L. Fabick, "Research on polycrystalline thin-film photovoltaic devices," *Journal of Crystal Growth*, vol. 61, no. 3, pp. 658-664, 1983, doi: 10.1016/0022-0248(83)90195-1.

[74] K. C. Sharma, R. P. Sharma, and J. C. Garg, "Structural, electrical and optical properties of solution grown polycrystalline Cu1-xAgxSe thin films," *Journal of Physics D: Applied Physics*, vol. 25, no. 6, pp. 1019-1025, 1992/06/14 1992, doi: 10.1088/0022-3727/25/6/021.

[75] S. R. Gosavi, N. G. Deshpande, Y. G. Gudage, and R. Sharma, "Physical, optical and electrical properties of copper selenide (CuSe) thin films deposited by solution growth technique at room temperature," *Journal of Alloys and Compounds*, vol. 448, no. 1-2, pp. 344-348, 2008, doi: 10.1016/j.jallcom.2007.03.068.

[76] T. Ohtani, Y. Tachibana, J. Ogura, T. Miyake, Y. Okada, and Y. Yokota, "Physical properties and phase transitions of β Cu2-xSe (0.20≤x≤0.25)," *Journal of Alloys and Compounds*, vol. 279, no. 2, pp. 136-141, 1998, doi: 10.1016/S0925-8388(98)00674-4.

[77] W. Liu, X. Yan, G. Chen, and Z. Ren, "Recent advances in thermoelectric nanocomposites," vol. 1, ed: Elsevier, 2012, pp. 42-56.

[78] M. S. Dresselhaus *et al.*, "New directions for low-dimensional thermoelectric materials," *Advanced Materials*, vol. 19, no. 8, pp. 1043-1053, 2007, doi: 10.1002/adma.200600527.

[79] B. Yu *et al.*, "Thermoelectric properties of copper selenide with ordered selenium layer and disordered copper layer," *Nano Energy*, vol. 1, no. 3, pp. 472-478, 2012/05/01/ 2012, doi: https://doi.org/10.1016/j.nanoen.2012.02.010.

[80] L. P. Bulat *et al.*, "Experimental and theoretical study of the thermoelectric properties of copper selenide," *Semiconductors*, vol. 51, no. 7, pp. 854-857, 2017, doi: 10.1134/S1063782617070041.

[81] M. Yao *et al.*, "Low temperature thermoelectric properties of p-type copper selenide with Ni, Te and Zn dopants," *Journal of Alloys and Compounds*, vol. 699, pp. 718-721, 2017/03/30/ 2017, doi: https://doi.org/10.1016/j.jallcom.2016.12.400.

[82] M. Y. Tafti *et al.*, "Promising bulk nanostructured Cu2Se thermoelectrics via high throughput and rapid chemical synthesis," *RSC Advances*, 10.1039/C6RA23005A vol. 6, no. 112, pp. 111457-111464, 2016, doi: 10.1039/C6RA23005A.

[83] K. Tyagi *et al.*, "Enhanced thermoelectric performance of spark plasma sintered copper-deficient nanostructured copper selenide," *Journal of Physics and Chemistry of Solids*, vol. 81, pp. 100-105, 2015/06/01/ 2015, doi: https://doi.org/10.1016/j.jpcs.2015.01.018.

[84] S. Butt *et al.*, "One-step rapid synthesis of Cu2Se with enhanced thermoelectric properties," *Journal of Alloys and Compounds*, vol. 786, pp. 557-564, 2019/05/25/ 2019, doi: https://doi.org/10.1016/j.jallcom.2019.01.359.

[85] J. Chen *et al.*, "Nanostructured monoclinic Cu2Se as a near-room-temperature thermoelectric material," *Nanoscale*, 10.1039/D0NR05829G vol. 12, no. 39, pp. 20536-20542, 2020, doi: 10.1039/D0NR05829G.

[86] B. Gahtori *et al.*, "Giant enhancement in thermoelectric performance of copper selenide by incorporation of different nanoscale dimensional defect features," *Nano Energy*, vol. 13, pp. 36-46, 2015/04/01/ 2015, doi: https://doi.org/10.1016/j.nanoen.2015.02.008.

[87] K. Zhao *et al.*, "Extremely low thermal conductivity and high thermoelectric performance in liquid-like Cu2Se1−xSx polymorphic materials," *Journal of*

Materials Chemistry A, 10.1039/C7TA05788A vol. 5, no. 34, pp. 18148-18156, 2017, doi: 10.1039/C7TA05788A.

[88] T. W. Day *et al.*, "Influence of Compensating Defect Formation on the Doping Efficiency and Thermoelectric Properties of Cu2-ySe1–xBrx," *Chemistry of Materials*, vol. 27, no. 20, pp. 7018-7027, 2015/10/27 2015, doi: 10.1021/acs.chemmater.5b02405.

[89] K. Zhao *et al.*, "Enhanced Thermoelectric Performance through Tuning Bonding Energy in Cu2Se1–xSx Liquid-like Materials," *Chemistry of Materials*, vol. 29, no. 15, pp. 6367-6377, 2017/08/08 2017, doi: 10.1021/acs.chemmater.7b01687.

[90] K. Zhao *et al.*, "Thermoelectric properties of Cu2Se1−xTex solid solutions," *Journal of Materials Chemistry A*, 10.1039/C8TA01313F vol. 6, no. 16, pp. 6977-6986, 2018, doi: 10.1039/C8TA01313F.

[91] D. Li *et al.*, "Chemical synthesis of nanostructured Cu2Se with high thermoelectric performance," *RSC Advances*, 10.1039/C3RA47015F vol. 4, no. 17, pp. 8638-8644, 2014, doi: 10.1039/C3RA47015F.

[92] F. Rong, Y. Bai, T. Chen, and W. Zheng, "Chemical synthesis of Cu2Se nanoparticles at room temperature," *Materials Research Bulletin*, vol. 47, no. 1, pp. 92-95, 2012/01/01/ 2012, doi: https://doi.org/10.1016/j.materresbull.2011.09.026.

[93] P. Kumar, K. Singh, and O. N. Srivastava, "Template free-solvothermaly synthesized copper selenide (CuSe, Cu2−xSe, β-Cu2Se and Cu2Se) hexagonal nanoplates from different precursors at low temperature," *Journal of Crystal Growth*, vol. 312, no. 19, pp. 2804-2813, 2010/09/15/ 2010, doi: https://doi.org/10.1016/j.jcrysgro.2010.06.014.

[94] K. Liu, H. Liu, J. Wang, and L. Shi, "Synthesis and characterization of Cu2Se prepared by hydrothermal co-reduction," *Journal of Alloys and Compounds,* vol. 484, no. 1, pp. 674-676, 2009/09/18/ 2009, doi: https://doi.org/10.1016/j.jallcom.2009.05.014.

[95] X. Han, F. Liao, Y. Zhang, Z. Yuan, H. Chen, and C. Xu, "CTAB-assisted hydrothermal synthesis of Cu2Se films composed of nanowire networks," *Materials Letters*, vol. 210, pp. 62-65, 2018/01/01/ 2018, doi: https://doi.org/10.1016/j.matlet.2017.08.124.

[96] F. Gao, S. L. Leng, Z. Zhu, X. J. Li, X. Hu, and H. Z. Song, "Preparation and Thermoelectric Properties of Cu2Se Hot-Pressed from Hydrothermal Synthesis Nanopowders," *Journal of Electronic Materials,* vol. 47, no. 4, pp. 2454-2460, 2018/04/01 2018, doi: 10.1007/s11664-018-6082-3.

[97] L. Yang, Z.-G. Chen, G. Han, M. Hong, Y. Zou, and J. Zou, "High-performance thermoelectric Cu2Se nanoplates through nanostructure engineering," *Nano Energy,*

vol. 16, pp. 367-374, 2015/09/01/ 2015, doi: https://doi.org/10.1016/j.nanoen.2015.07.012.

[98] Y. Li *et al.*, "Mesoporous Cu2-xSe nanocrystals as an ultrahigh-rate and long-lifespan anode material for sodium-ion batteries," *Energy Storage Materials*, vol. 22, pp. 275-283, 2019/11/01/ 2019, doi: https://doi.org/10.1016/j.ensm.2019.02.009.

[99] R. Jin, X. Liu, L. Yang, G. Li, and S. Gao, "Sandwich-like Cu2-xSe@ C@ MoSe2 nanosheets as an improved-performance anode for lithium-ion battery," *Electrochimica Acta*, vol. 259, pp. 841-849, 2018.

[100] D. Chen *et al.*, "Nanosheets assembling hierarchical starfish-like Cu2−xSe as advanced cathode for rechargeable Mg batteries," *Chemical Engineering Journal*, vol. 384, p. 123235, 2020/03/15/ 2020, doi: https://doi.org/10.1016/j.cej.2019.123235.

[101] X. Li, Z. Zhang, C. Liu, and Z. Lin, "Capacity Increase Investigation of Cu2Se Electrode by Using Electrochemical Impedance Spectroscopy," (in English), *Frontiers in Chemistry*, Original Research vol. 6, no. 221, 2018-June-12 2018, doi: 10.3389/fchem.2018.00221.

[102] Y. Xiao *et al.*, "A Nanosheet Array of Cu2Se Intercalation Compound with Expanded Interlayer Space for Sodium Ion Storage," *Advanced Energy Materials*, https://doi.org/10.1002/aenm.202000666 vol. 10, no. 25, p. 2000666, 2020/07/01 2020, doi: https://doi.org/10.1002/aenm.202000666.

[103] J.-Y. Tak *et al.*, "Significantly enhanced chemical stability in interface-controlled Cu2+xSe-reduced graphene oxide composites and related thermoelectric performances," *J. Eur. Ceram. Soc.*, 10.1016/j.jeurceramsoc.2020.08.023 vol. 41, no. 1, pp. 459-465, // 2021, doi: 10.1016/j.jeurceramsoc.2020.08.023.

[104] S. D. Kang *et al.*, "Enhanced stability and thermoelectric figure-of-merit in copper selenide by lithium doping," *Materials Today Physics*, vol. 1, pp. 7-13, 2017/06/01/ 2017, doi: https://doi.org/10.1016/j.mtphys.2017.04.002.

[105] Q. Hu, Z. Zhu, Y. Zhang, X.-J. Li, H. Song, and Y. Zhang, "Remarkably high thermoelectric performance of Cu2−xLixSe bulks with nanopores," *Journal of Materials Chemistry A*, 10.1039/C8TA06912C vol. 6, no. 46, pp. 23417-23424, 2018, doi: 10.1039/C8TA06912C.

[106] P. Peng *et al.*, "Structure and thermoelectric performance of β-Cu2Se doped with Fe, Ni, Mn, In, Zn or Sm," *Intermetallics*, vol. 75, pp. 72-78, 2016/08/01/ 2016, doi: https://doi.org/10.1016/j.intermet.2016.05.012.

[107] T. W. Day *et al.*, "High-temperature thermoelectric properties of Cu1.97Ag0.03Se1+y," *Materials for Renewable and Sustainable Energy*, vol. 3, no. 2, p. 26, 2014/03/14 2014, doi: 10.1007/s40243-014-0026-5.

[108] L. Yang, Z.-G. Chen, G. Han, M. Hong, L. Huang, and J. Zou, "Te-Doped Cu2Se nanoplates with a high average thermoelectric figure of merit," *Journal of Materials*

Chemistry A, 10.1039/C6TA02998A vol. 4, no. 23, pp. 9213-9219, 2016, doi: 10.1039/C6TA02998A.

[109] Z. Zhu, Y. Zhang, H. Song, and X.-J. Li, "Enhancement of thermoelectric performance of Cu2Se by K doping," *Applied Physics A*, vol. 124, no. 12, p. 871, 2018/12/04 2018, doi: 10.1007/s00339-018-2299-5.

[110] Z. Zhu, Y. W. Zhang, H. Z. Song, and X. J. Li, "Enhancement of the Thermoelectric Properties of Cu1.98Se by Na Doping," *Journal of Electronic Materials*, vol. 47, no. 12, pp. 7514-7519, 2018/12/01 2018, doi: 10.1007/s11664-018-6694-7.

[111] K. S. Novoselov *et al.*, "Electric Field Effect in Atomically Thin Carbon Films," *Science*, vol. 306, no. 5696, pp. 666-669, 2004. [Online]. Available: www.jstor.org/stable/3839379

https://science.sciencemag.org/content/306/5696/666.long.

[112] H. Shen, L. Zhang, M. Liu, and Z. Zhang, "Biomedical applications of graphene," (in eng), *Theranostics*, vol. 2, no. 3, pp. 283-294, 2012, doi: 10.7150/thno.3642.

[113] P. Blake *et al.*, "Graphene-Based Liquid Crystal Device," *Nano Letters*, vol. 8, no. 6, pp. 1704-1708, 2008, doi: 10.1021/nl080649i.

[114] G. Jo, M. Choe, S. Lee, W. Park, Y. H. Kahng, and T. Lee, "The application of graphene as electrodes in electrical and optical devices," *Nanotechnology,* vol. 23, no. 11, p. 112001, 2012/02/28 2012, doi: 10.1088/0957-4484/23/11/112001.

[115] M. Liang, B. Luo, and L. Zhi, "Application of graphene and graphene-based materials in clean energy-related devices," *International Journal of Energy Research,* vol. 33, no. 13, pp. 1161-1170, 2009/10/25 2009, doi: 10.1002/er.1598.

[116] S. K. Tiwari, V. Kumar, A. Huczko, R. Oraon, A. D. Adhikari, and G. C. Nayak, "Magical Allotropes of Carbon: Prospects and Applications," *Critical Reviews in Solid State and Materials Sciences,* vol. 41, no. 4, pp. 257-317, 2016, doi: 10.1080/10408436.2015.1127206.

[117] G. Wang *et al.*, "Facile Synthesis and Characterization of Graphene Nanosheets," *The Journal of Physical Chemistry C,* vol. 112, no. 22, pp. 8192-8195, 2008/06/01 2008, doi: 10.1021/jp710931h.

[118] K. Kakaei, M. D. Esrafili, and A. Ehsani, "Graphene-Based Metal Particles," Elsevier, 2019, pp. 153-202.

[119] J. Zhou and R. Huang, "Internal lattice relaxation of single-layer graphene under in-plane deformation," *Journal of the Mechanics and Physics of Solids,* vol. 56, no. 4, pp. 1609-1623, 2008/04/01/ 2008, doi: https://doi.org/10.1016/j.jmps.2007.07.013.

[120] S. K. Tiwari, S. Sahoo, N. Wang, and A. Huczko, "Graphene research and their outputs: Status and prospect," *Journal of Science: Advanced Materials and Devices,* vol. 5, no. 1, pp. 10-29, 2020/03/01/ 2020, doi: https://doi.org/10.1016/j.jsamd.2020.01.006.

[121] P. Avouris and C. Dimitrakopoulos, "Graphene: synthesis and applications," *Materials Today,* vol. 15, no. 3, pp. 86-97, 2012/03/01/ 2012, doi: https://doi.org/10.1016/S1369-7021(12)70044-5.

[122] M. Bacon, S. J. Bradley, and T. Nann, "Graphene Quantum Dots," *Particle & Particle Systems Characterization,* vol. 31, no. 4, pp. 415-428, 2014/04/01 2014, doi: 10.1002/ppsc.201300252.

[123] S. K. Tiwari, V. Kumar, A. Huczko, R. Oraon, A. D. Adhikari, and G. C. Nayak, "Magical Allotropes of Carbon: Prospects and Applications," vol. 41, no. 4, pp. 257-317, 2016, doi: 10.1080/10408436.2015.1127206.

[124] H. Kim, A. A. Abdala, and C. W. Macosko, "Graphene/Polymer Nanocomposites," *Macromolecules,* vol. 43, no. 16, pp. 6515-6530, 2010/08/24 2010, doi: 10.1021/ma100572e.

[125] K. Kakaei, M. D. Esrafili, and A. Ehsani, "Chapter 5 - Graphene-Based Metal Particles," in *Interface Science and Technology*, vol. 27, K. Kakaei, M. D. Esrafili, and A. Ehsani Eds.: Elsevier, 2019, pp. 153-202.

[126] A. K. Geim and K. S. Novoselov, "The rise of graphene," *Nature Materials,* vol. 6, no. 3, pp. 183-191, 2007/03/01 2007, doi: 10.1038/nmat1849.

[127] A. A. Balandin, "Thermal properties of graphene and nanostructured carbon materials," *Nature Materials,* vol. 10, no. 8, pp. 569-581, 2011/08/01 2011, doi: 10.1038/nmat3064.

[128] A. A. Balandin *et al.*, "Superior Thermal Conductivity of Single-Layer Graphene," *Nano Letters,* vol. 8, no. 3, pp. 902-907, 2008/03/01 2008, doi: 10.1021/nl0731872.

[129] D. L. Nika and A. A. Balandin, "Phonons and thermal transport in graphene and graphene-based materials," *Reports on Progress in Physics,* vol. 80, no. 3, p. 036502, 2017/01/20 2017, doi: 10.1088/1361-6633/80/3/036502.

[130] Y. Anno, Y. Imakita, K. Takei, S. Akita, and T. Arie, "Enhancement of graphene thermoelectric performance through defect engineering," *2D Materials,* vol. 4, no. 2, p. 025019, 2017/02/02 2017, doi: 10.1088/2053-1583/aa57fc.

[131] J. Hu, S. Schiffli, A. Vallabhaneni, X. Ruan, and Y. P. Chen, "Tuning the thermal conductivity of graphene nanoribbons by edge passivation and isotope engineering: A molecular dynamics study," *Applied Physics Letters,* vol. 97, no. 13, p. 133107, 2010, doi: 10.1063/1.3491267.

[132] H.-S. Zhang, Z.-X. Guo, X.-G. Gong, and J.-X. Cao, "Thermal conductivity of sawtooth-like graphene nanoribbons: A molecular dynamics study," vol. 112, no. 12, p. 123508, 2012, doi: 10.1063/1.4768445.

[133] F. Mazzamuto *et al.*, "Enhanced thermoelectric properties in graphene nanoribbons by resonant tunneling of electrons," *Physical Review B*, vol. 83, no. 23, p. 235426, 06/29/ 2011, doi: 10.1103/PhysRevB.83.235426.

[134] H. Sevinçli, C. Sevik, T. Çağın, and G. Cuniberti, "A bottom-up route to enhance thermoelectric figures of merit in graphene nanoribbons," *Scientific Reports*, vol. 3, no. 1, p. 1228, 2013/02/06 2013, doi: 10.1038/srep01228.

[135] D. G. Papageorgiou, I. A. Kinloch, and R. J. Young, "Mechanical properties of graphene and graphene-based nanocomposites," *Progress in Materials Science*, vol. 90, pp. 75-127, 2017/10/01/ 2017, doi: https://doi.org/10.1016/j.pmatsci.2017.07.004.

[136] K. Ahmad, W. Pan, and H. Wu, "High performance alumina based graphene nanocomposites with novel electrical and dielectric properties," *RSC Advances*, 10.1039/C5RA01481F vol. 5, no. 42, pp. 33607-33614, 2015, doi: 10.1039/C5RA01481F.

[137] Y. Xie *et al.*, "Flexible thermoelectric nanogenerator based on the MoS2/graphene nanocomposite and its application for a self-powered temperature sensor,"

Semiconductor Science and Technology, vol. 32, no. 4, p. 044003, 2017/03/24 2017, doi: 10.1088/1361-6641/aa62f2.

[138] L. Wang, Q. Yao, H. Bi, F. Huang, Q. Wang, and L. Chen, "Large thermoelectric power factor in polyaniline/graphene nanocomposite films prepared by solution-assistant dispersing method," *Journal of Materials Chemistry A*, 10.1039/C4TA01541J vol. 2, no. 29, pp. 11107-11113, 2014, doi: 10.1039/C4TA01541J.

[139] K. Ahmad, C. Wan, M. A. Al-Eshaikh, and A. N. Kadachi, "Enhanced thermoelectric performance of Bi2Te3 based graphene nanocomposites," *Applied Surface Science*, vol. 474, pp. 2-8, 2019/04/30/ 2019, doi: https://doi.org/10.1016/j.apsusc.2018.10.163.

[140] M. Li *et al.*, "Ultra-high thermoelectric performance in graphene incorporated Cu2Se: Role of mismatching phonon modes," *Nano Energy*, vol. 53, pp. 993-1002, 2018/11/01/ 2018, doi: https://doi.org/10.1016/j.nanoen.2018.09.041.

[141] M. Li, S. M. Kazi Nazrul Islam, S. Dou, and X. Wang, "Significantly enhanced figure-of-merit in graphene nanoplate incorporated Cu2Se fabricated by spark plasma sintering," *Journal of Alloys and Compounds*, vol. 769, pp. 59-64, 2018/11/15/ 2018, doi: https://doi.org/10.1016/j.jallcom.2018.07.353.

[142] Q. Hu, Y. Zhang, Y. Zhang, X.-J. Li, and H. Song, "High thermoelectric performance in Cu2Se/CDs hybrid materials," *Journal of Alloys and Compounds*, vol. 813, p. 152204, 2020/01/15/ 2020, doi: https://doi.org/10.1016/j.jallcom.2019.152204.

[143] R. Nunna *et al.*, "Ultrahigh thermoelectric performance in Cu2Se-based hybrid materials with highly dispersed molecular CNTs," *Energy & Environmental Science*, 10.1039/C7EE01737E vol. 10, no. 9, pp. 1928-1935, 2017, doi: 10.1039/C7EE01737E.

[144] L. Zhao *et al.*, "Significant enhancement of figure-of-merit in carbon-reinforced Cu2Se nanocrystalline solids," *Nano Energy*, vol. 41, pp. 164-171, 2017/11/01/ 2017, doi: https://doi.org/10.1016/j.nanoen.2017.09.020.

[145] W. S. Hummers Jr and R. E. Offeman, "Preparation of graphitic oxide," *Journal of the american chemical society*, vol. 80, no. 6, pp. 1339-1339, 1958.

[146] D. C. Marcano *et al.*, "Improved Synthesis of Graphene Oxide," *ACS Nano*, vol. 4, no. 8, pp. 4806-4814, 2010/08/24 2010, doi: 10.1021/nn1006368.

[147] A. Chauhan and P. Chauhan, "Powder XRD technique and its applications in science and technology," *J Anal Bioanal Tech*, vol. 5, no. 5, pp. 1-5, 2014.

[148] R. Kohli, "Chapter 3 - Methods for Monitoring and Measuring Cleanliness of Surfaces," in *Developments in Surface Contamination and Cleaning*, R. Kohli and K. L. Mittal Eds. Oxford: William Andrew Publishing, 2012, pp. 107-178.

[149] Y. Shahmoradi and D. Souri, "Growth of silver nanoparticles within the tellurovanadate amorphous matrix: Optical band gap and band tailing properties, beside the Williamson-Hall estimation of crystallite size and lattice strain," *Ceramics International*, vol. 45, no. 6, pp. 7857-7864, 2019/04/15/ 2019, doi: https://doi.org/10.1016/j.ceramint.2019.01.094.

[150] A. W. Burton, K. Ong, T. Rea, and I. Y. Chan, "On the estimation of average crystallite size of zeolites from the Scherrer equation: A critical evaluation of its application to zeolites with one-dimensional pore systems," *Microporous and Mesoporous Materials*, vol. 117, no. 1, pp. 75-90, 2009/01/01/ 2009, doi: https://doi.org/10.1016/j.micromeso.2008.06.010.

[151] S. Mahadevan, S. P. Behera, G. Gnanaprakash, T. Jayakumar, J. Philip, and B. P. C. Rao, "Size distribution of magnetic iron oxide nanoparticles using Warren–Averbach XRD analysis," *Journal of Physics and Chemistry of Solids*, vol. 73, no. 7, pp. 867-872, 2012/07/01/ 2012, doi: https://doi.org/10.1016/j.jpcs.2012.02.017.

[152] D. Nath, F. Singh, and R. Das, "X-ray diffraction analysis by Williamson-Hall, Halder-Wagner and size-strain plot methods of CdSe nanoparticles- a comparative study," *Materials Chemistry and Physics*, vol. 239, p. 122021, 2020/01/01/ 2020, doi: https://doi.org/10.1016/j.matchemphys.2019.122021.

[153] D. R. Baer and S. Thevuthasan, "Chapter 16 - Characterization of Thin Films and Coatings," in *Handbook of Deposition Technologies for Films and Coatings (Third Edition)*, P. M. Martin Ed. Boston: William Andrew Publishing, 2010, pp. 749-864.

[154] S. Ebnesajjad, "4 - Surface and Material Characterization Techniques," in *Handbook of Adhesives and Surface Preparation*, S. Ebnesajjad Ed. Oxford: William Andrew Publishing, 2011, pp. 31-48.

[155] R. B. Prime, H. E. Bair, S. Vyazovkin, P. K. Gallagher, and A. Riga, "Thermogravimetric analysis (TGA)," *Thermal analysis of polymers: Fundamentals and applications*, pp. 241-317, 2009.

[156] V. Tebaldo and G. Gautier, "Influences of evaluation methods and testing load on microhardness and Young's modulus of ZTA and ATZ ceramics," *Ceramics International*, vol. 39, no. 3, pp. 2683-2693, 2013, doi: 10.1016/j.ceramint.2012.09.035.

[157] R. E. Smallman and A. H. W. Ngan, "Chapter 5 - Characterization and Analysis," in *Modern Physical Metallurgy (Eighth Edition)*, R. E. Smallman and A. H. W. Ngan Eds. Oxford: Butterworth-Heinemann, 2014, pp. 159-250.

[158] A. Gobeaut, L. Laffont, J. M. Tarascon, L. Parissi, and O. Kerrec, "Influence of secondary phases during annealing on re-crystallization of CuInSe2 electrodeposited

films," *Thin Solid Films,* vol. 517, no. 15, pp. 4436-4442, 2009/06/01/ 2009, doi: https://doi.org/10.1016/j.tsf.2009.01.043.

[159] T. Vinod, X. Jin, and J. Kim, "Hexagonal nanoplatelets of CuSe synthesized through facile solution phase reaction," *Materials Research Bulletin,* vol. 46, no. 3, pp. 340-344, 2011.

[160] J. Y. C. Liew, Z. A. Talib, Z. Zainal, M. A. Kamarudin, N. H. Osman, and H. K. Lee, "Structural and transport mechanism studies of copper selenide nanoparticles," *Semiconductor Science and Technology,* vol. 34, no. 12, p. 125017, 2019.

[161] Y. Liu, S. Shen, J. Zhang, W. Zhong, and X. Huang, "Cu2−xSe/CdS composite photocatalyst with enhanced visible light photocatalysis activity," *Applied Surface Science,* vol. 478, pp. 762-769, 2019/06/01/ 2019, doi: https://doi.org/10.1016/j.apsusc.2019.02.010.

[162] C. Han, Z. Li, W.-j. Li, S.-l. Chou, and S.-x. Dou, "Controlled synthesis of copper telluride nanostructures for long-cycling anodes in lithium ion batteries," *Journal of Materials Chemistry A,* vol. 2, no. 30, pp. 11683-11690, 2014.

[163] V. V. Singh and A. K. Singh, "Tetragonal Cu 2 Se nanoflakes: synthesis using selenated propylamine as Se source and activation of Suzuki and Sonogashira cross coupling reactions," *Dalton Transactions,* vol. 44, no. 2, pp. 725-732, 2015.

[164] F. Jia, S. Zhang, X. Zhang, X. Peng, H. Zhang, and Y. Xiang, "Sb-Triggered β-to-α Transition: Solvothermal Synthesis of Metastable α-Cu2Se," *Chemistry–A European Journal*, vol. 20, no. 48, pp. 15941-15946, 2014.

[165] S. Sali, H. R. Mackey, and A. A. Abdala, "Effect of Graphene Oxide Synthesis Method on Properties and Performance of Polysulfone-Graphene Oxide Mixed Matrix Membranes," *Nanomaterials*, vol. 9, no. 5, 2019, doi: 10.3390/nano9050769.

[166] D. R. Brown, T. Day, T. Caillat, and G. J. Snyder, "Chemical Stability of (Ag,Cu)2Se: a Historical Overview," *Journal of Electronic Materials*, vol. 42, no. 7, pp. 2014-2019, 2013/07/01 2013, doi: 10.1007/s11664-013-2506-2.

[167] L. Xue *et al.*, "Thermoelectric performance of Cu2Se bulk materials by high-temperature and high-pressure synthesis," *Journal of Materiomics*, vol. 5, no. 1, pp. 103-110, 2019/03/01/ 2019, doi: https://doi.org/10.1016/j.jmat.2018.12.002.

[168] K. Tyagi *et al.*, "Crystal structure and mechanical properties of spark plasma sintered Cu2Se: An efficient photovoltaic and thermoelectric material," *Solid State Communications*, vol. 207, pp. 21-25, 2015/04/01/ 2015, doi: https://doi.org/10.1016/j.ssc.2015.02.004.

[169] R. Nunna *et al.*, "Ultrahigh thermoelectric performance in Cu 2 Se-based hybrid materials with highly dispersed molecular CNTs," *Energy & Environmental Science*, vol. 10, no. 9, pp. 1928-1935, 2017.

[170] F. Gao, S. Leng, Z. Zhu, X. Li, X. Hu, and H. Song, "Preparation and thermoelectric properties of Cu 2 Se hot-pressed from hydrothermal synthesis nanopowders," *Journal of Electronic Materials*, vol. 47, no. 4, pp. 2454-2460, 2018.

[171] A. Stevels and F. Jellinek, "Phase transitions in copper chalcogenides: I. The copper-selenium system," *Recueil des Travaux Chimiques des Pays-Bas,* vol. 90, no. 3, pp. 273-283, 1971.

APPENDIX A

A.1. Linear fits of grain size calculations for the composites

Figure A.1 shows the Williamson Hall and Warren Averbach linear fits for Tour's GO composites

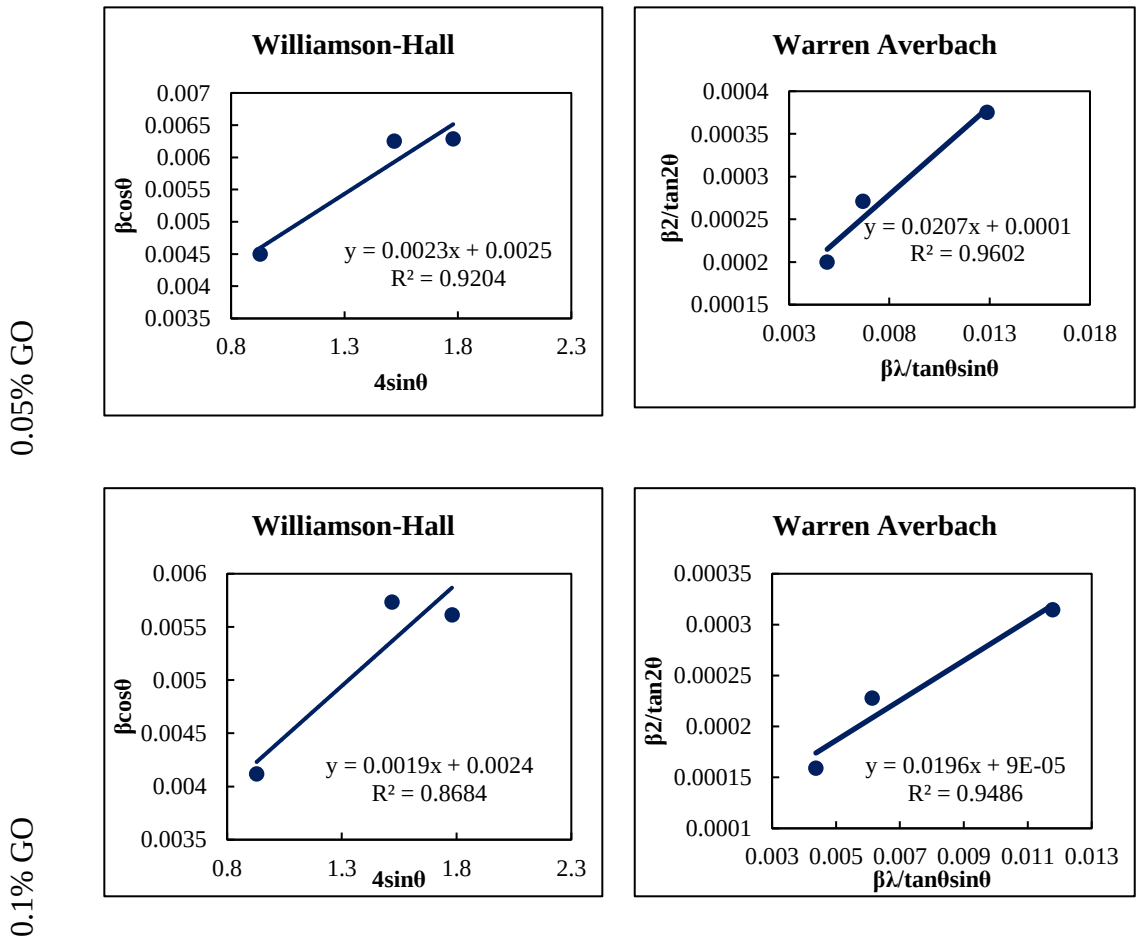

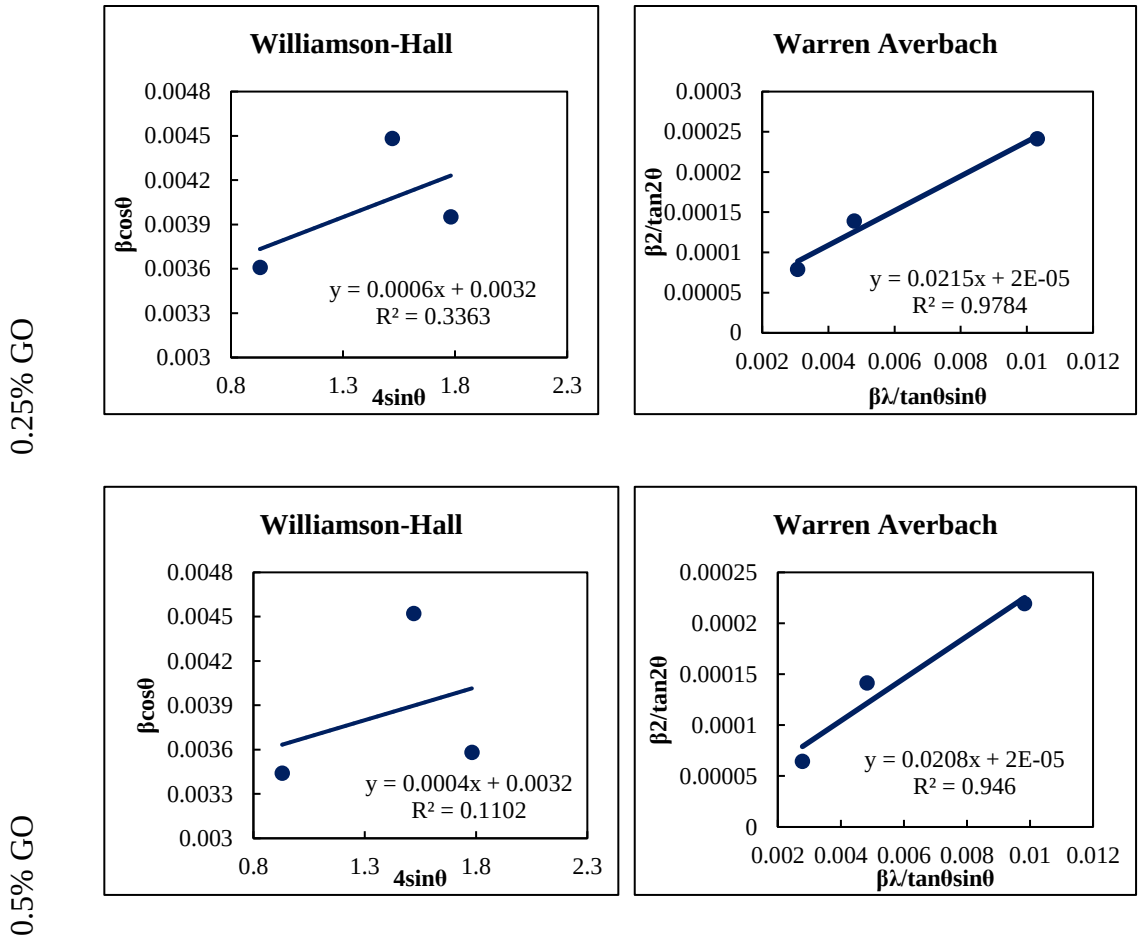

Figure A.2.: Linear fits of (a) Williamson-Hall and (b) Warren-Averbach models for $Cu_{1.8}Se$- Tour's GO composite. The R^2 value for Warren Averbach is higher, suggesting Warren-Averbach is a better fit.

Figure A.2 shows the Williamson Hall and Warren Averbach linear fits for Hummer's GO composites.

0.05% GO

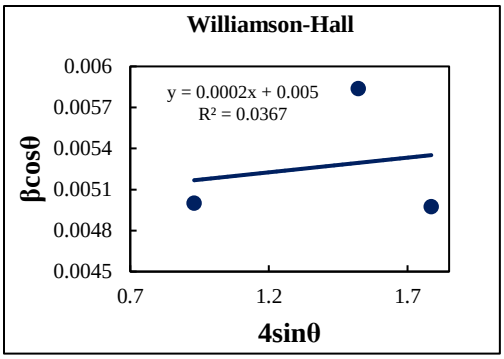

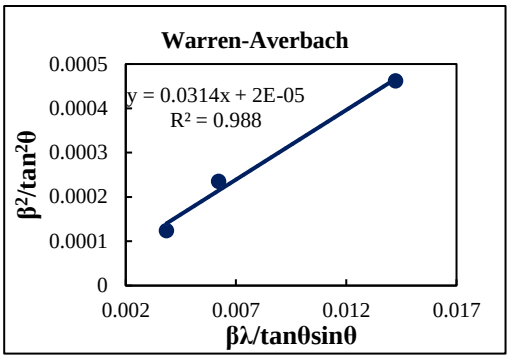

0.1% GO

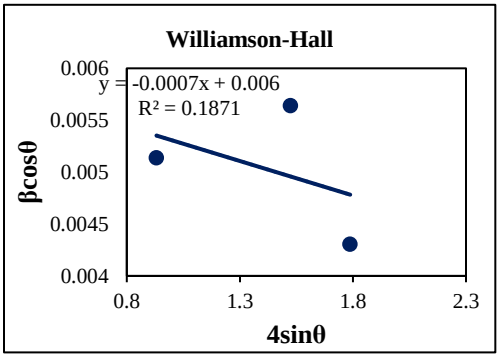

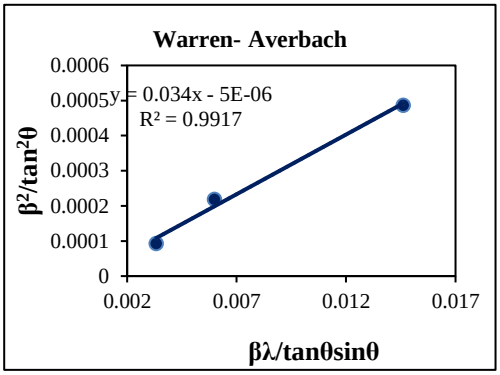

0.25% GO

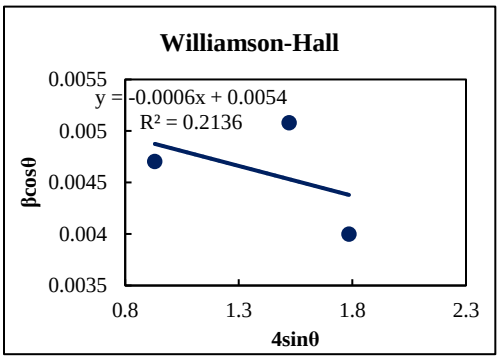

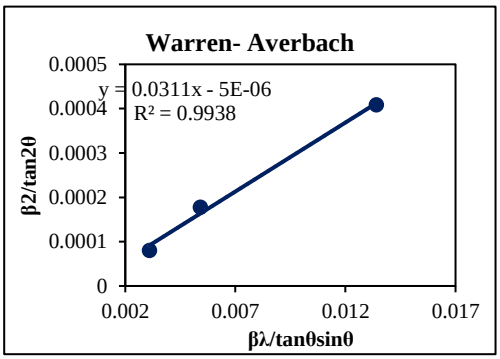

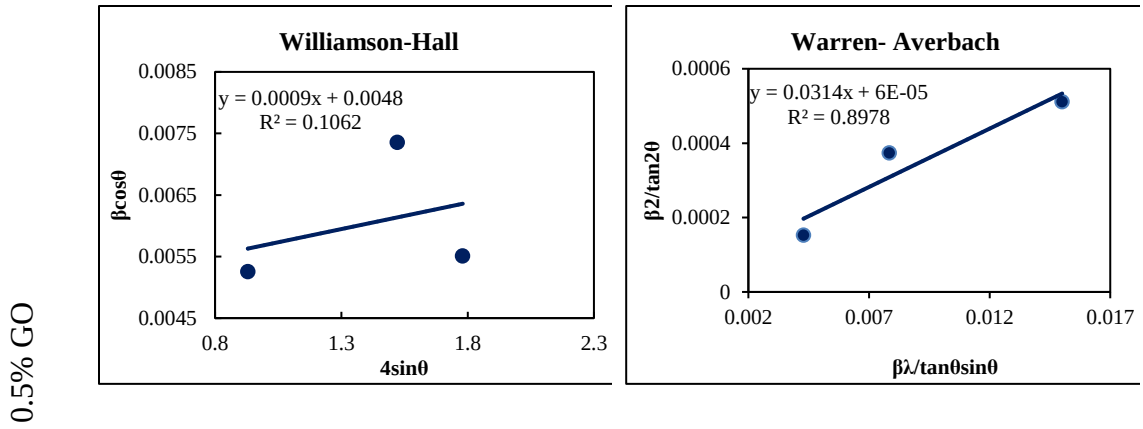

A.1 1: Linear fits of (a) Williamson-Hall and (b) Warren-Averbach models for $Cu_{1.8}Se$- Hummer's GO composite. The R^2 value for Warren Averbach is higher, suggesting Warren-Averbach is a better fit.

A.2. SEM images of the composites

The SEM images of the Tour's GO and Hummer's GO composties are shown below.

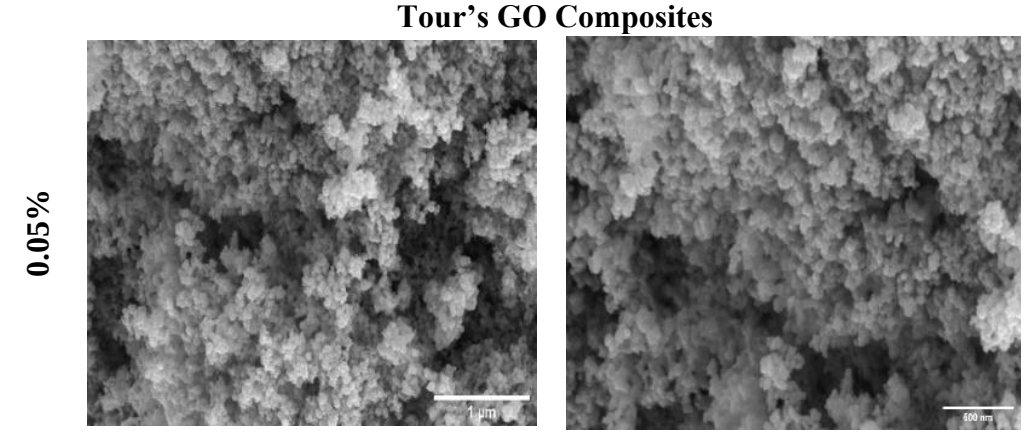

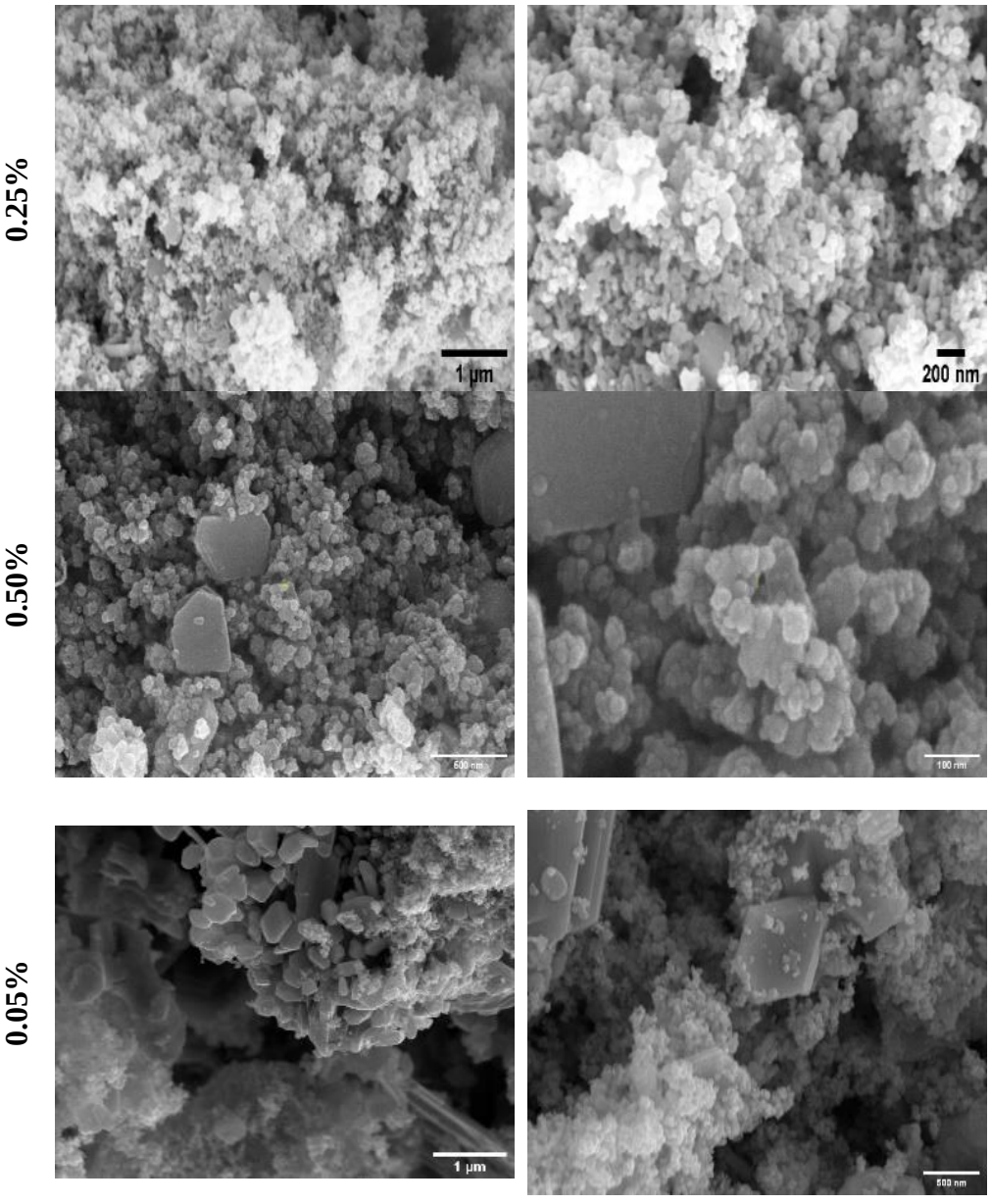
0.25%
0.50%
0.05%
1 µm
200 nm
1 µm

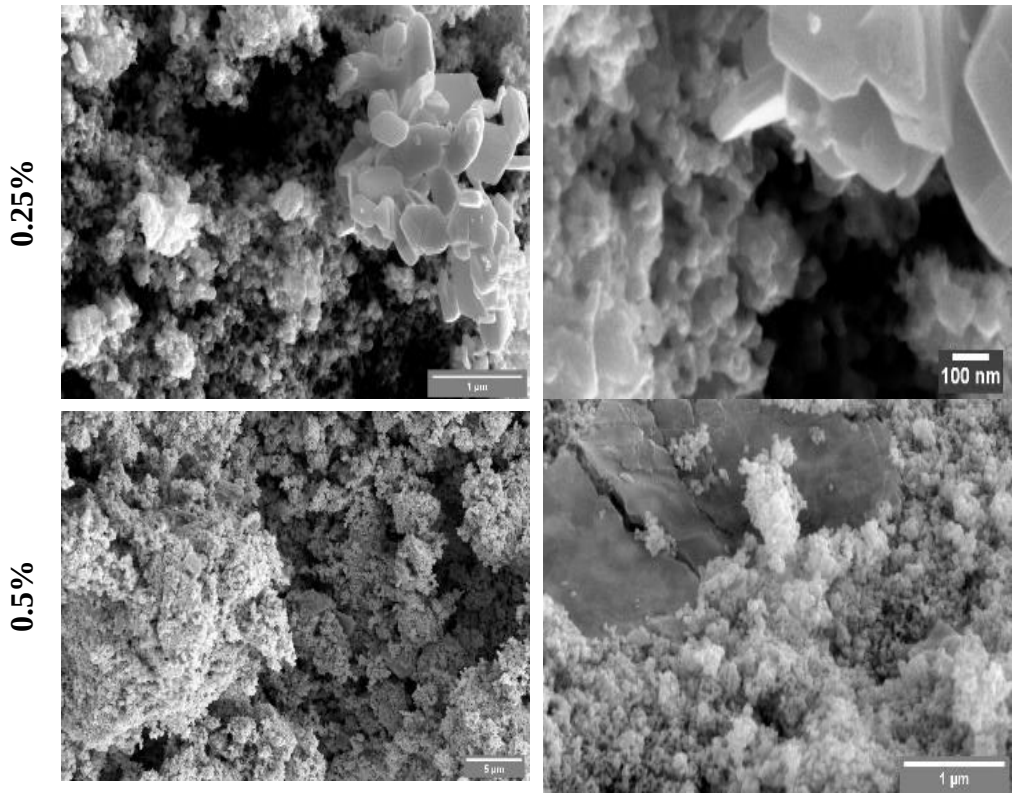

A.1 2: SEM Images of the composites

A.3. XPS Spectra of the composites.

The below images show the deconvoluted XPS scans of the Cu2p and Sed 3d spectra.

Tour's GO composites:

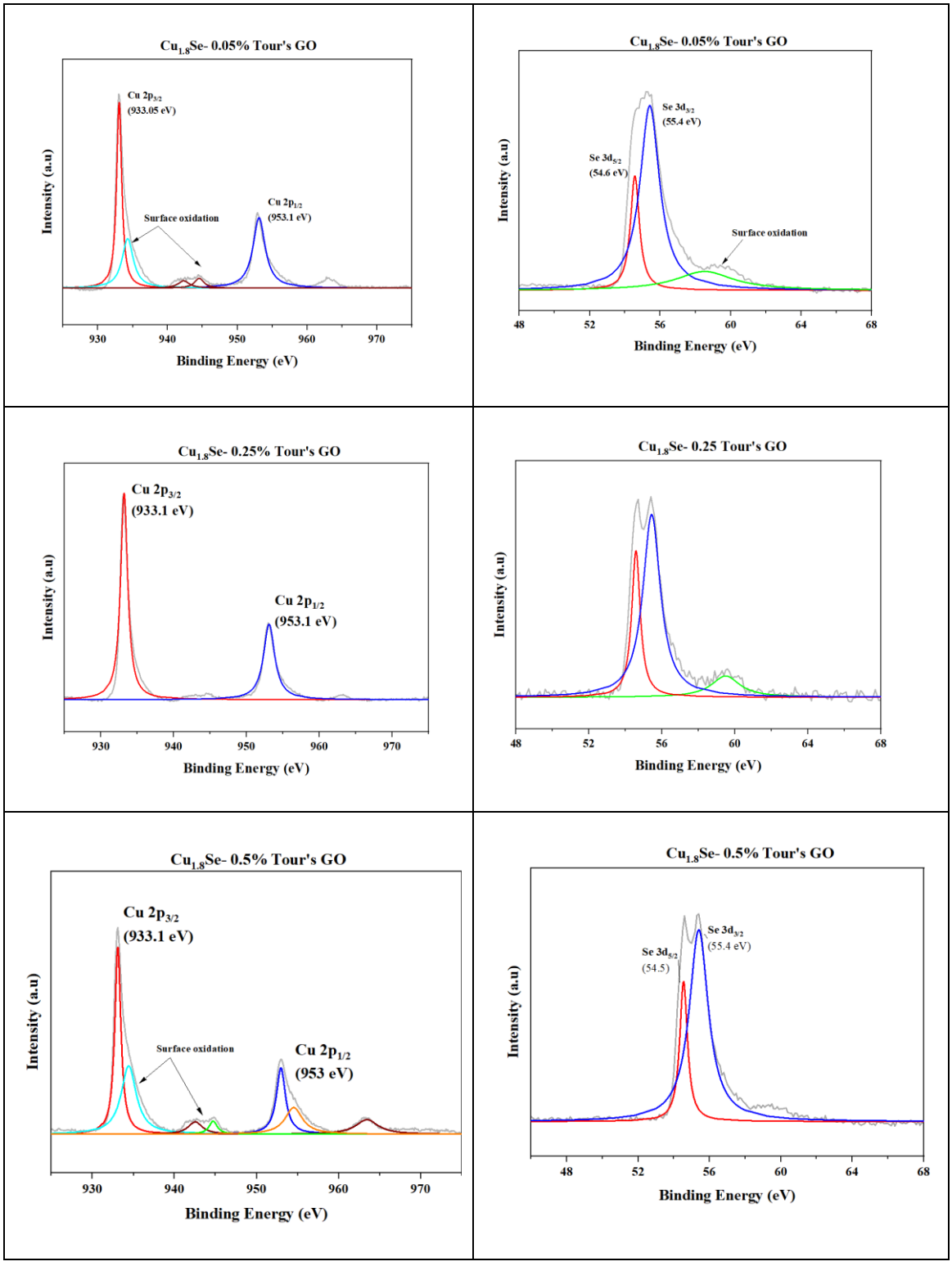
Cu1.8Se- 0.05% Tour's GO
Cu 2p3/2
(933.05 eV)
Surface oxidation
Cu 2p1/2
(953.1 eV)
Intensity (a.u)
Binding Energy (eV)
Cu1.8Se- 0.05% Tour's GO
Se 3d3/2
(55.4 eV)
Se 3d5/2
(54.6 eV)
Surface oxidation
Intensity (a.u)
Binding Energy (eV)
Cu1.8Se- 0.25% Tour's GO
Cu 2p3/2
(933.1 eV)
Cu 2p1/2
(953.1 eV)
Intensity (a.u)
Binding Energy (eV)
Cu1.8Se- 0.25 Tour's GO
Intensity (a.u)
Binding Energy (eV)
Cu1.8Se- 0.5% Tour's GO
Cu 2p3/2
(933.1 eV)
Surface oxidation
Cu 2p1/2
(953 eV)
Intensity (a.u)
Binding Energy (eV)
Cu1.8Se- 0.5% Tour's GO
Se 3d3/2
(55.4 eV)
Se 3d5/2
(54.5)
Intensity (a.u)
Binding Energy (eV)

A.1 3: $Cu_{1.8}Se$ – Tour's GO- XPS spectra of (a) Cu 2p (b) Se 3d

Hummer's GO composites:

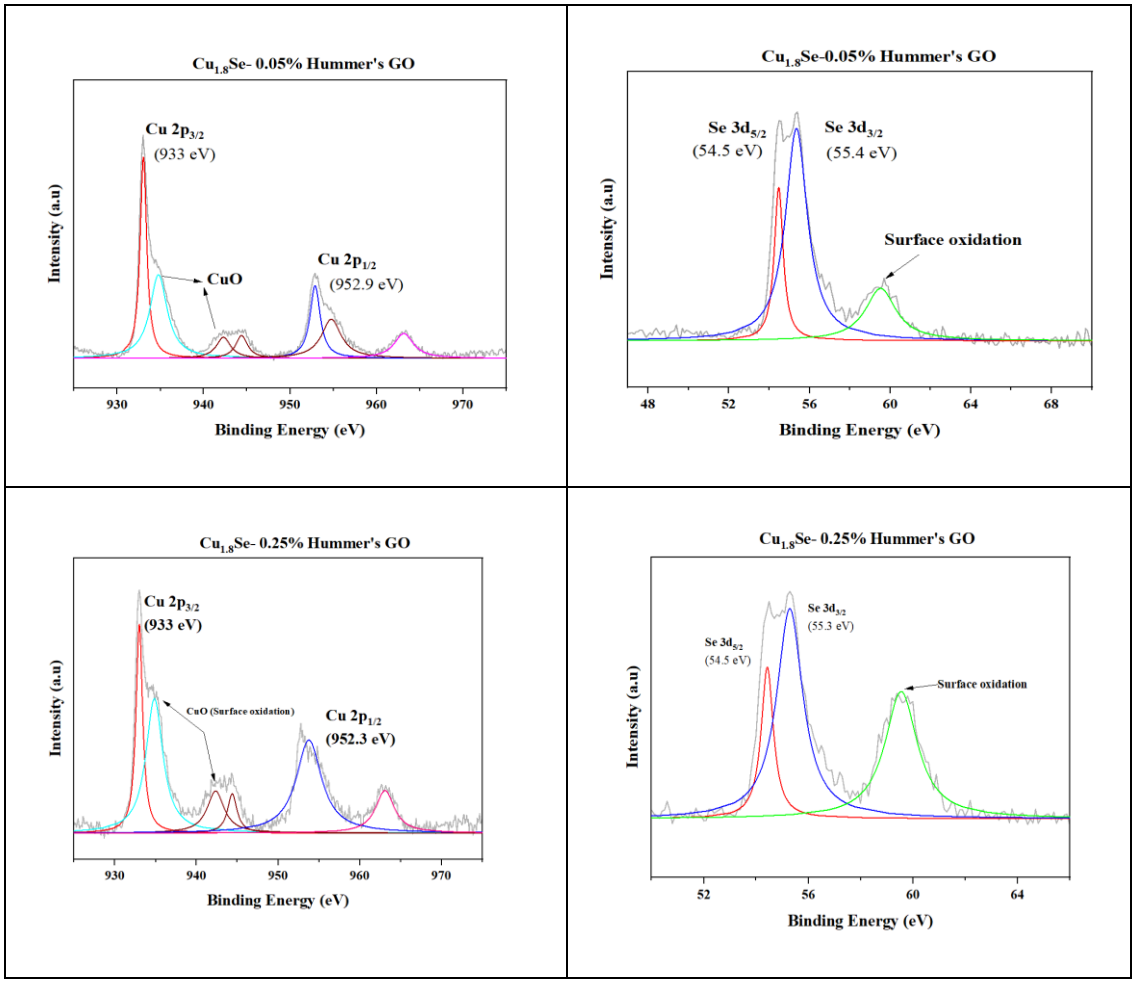

A.1 4: $Cu_{1.8}Se$ – Hummer's GO- XPS spectra of (a) Cu 2p (b) Se 3d

A.4.DSC Scans

Tours GO Composite:

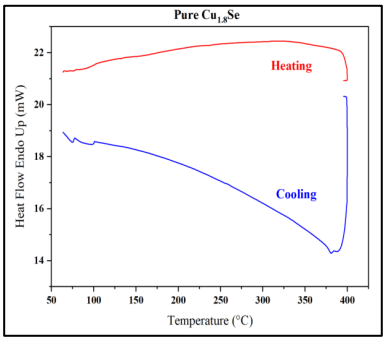

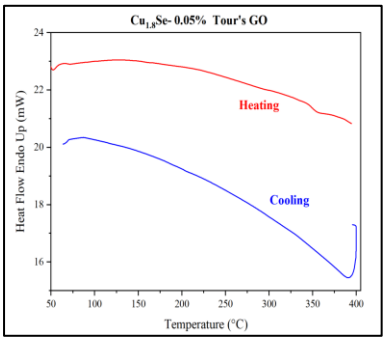

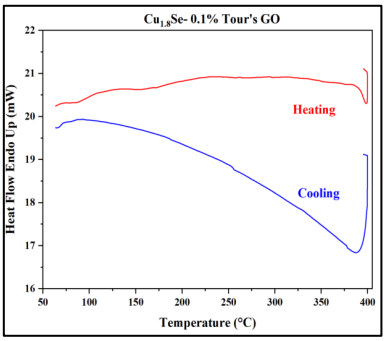

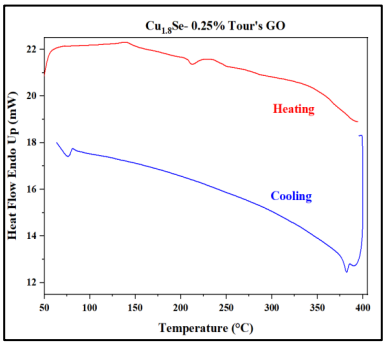

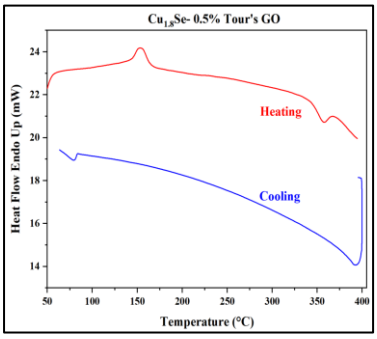

Hummer's GO composites

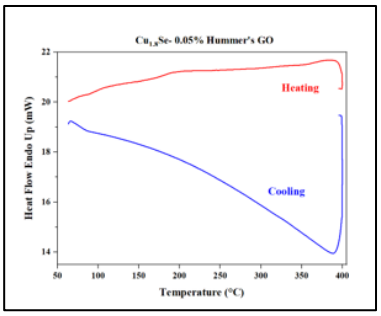

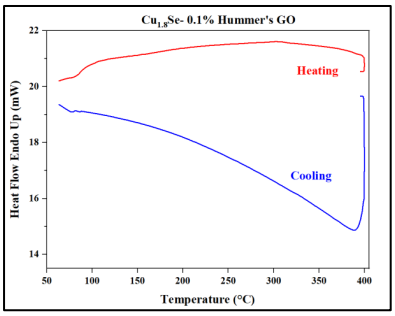

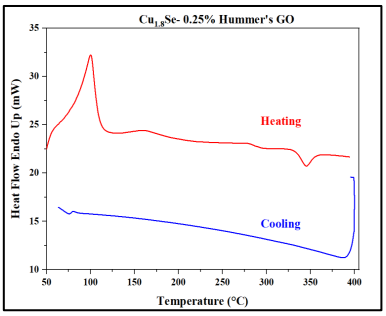

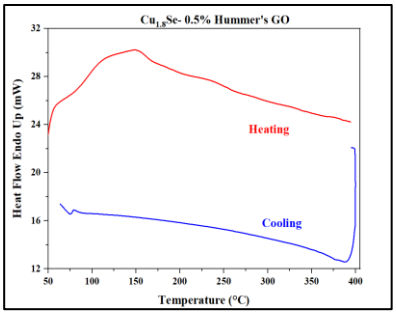
Cu1.8Se- 0.5% Hummer's GO
Heat Flow Endo Up (mW)
Temperature (°C)
Heating
Cooling
32
28
24
20
16
12
50
100
150
200
250
300
350
400